DEVELOPMENTS FOR THE TOF STRAW TRACKER

Dissertation
zur
Erlangung des Doktorgrades (Dr.rer.nat)
der
Mathematisch-Naturwissenschaftlichen Fakultät
der
Rheinischen Friedrich-Wilhelms-Universität Bonn

vorgelegt von
Aziz Ucar

Bonn 2006

Angefertigt mit Genehmigung der Mathematisch-Naturwissenschaftlichen Fakultät der Rheinischen Friedrich-Wilhelms-Universität Bonn

1. Referent: Prof. Dr. Kurt Kilian
2. Referent: Prof. Dr. Peter Herzog

Tag der Promotion: 17.11.2006

Erscheinungsjahr:2006

Abstract

COSY-TOF is a very large acceptance spectrometer for charged particles using precise information on track geometry and time of flight of reaction products. It is an external detector system at the Cooler Synchrotron and storage ring COSY in Jülich.

In order to improve the performance of the COSY-TOF, a new tracking detector *"Straw Tracker"* is being constructed which combines very low mass, operation in vacuum, very good resolution, high sampling density and very high acceptance. A comparison of $pp \rightarrow d\pi^+$ data and a simulation using the straw tracker with geometry alone indicates big improvements with the new tracker.

In order to investigate the straw tracker properties a small tracking hodoscope "*cosmic ray test facility*" was constructed in advance. It is made of two crossed hodoscopes consisting of 128 straw tubes arranged in 4 double planes.

For the first time Jülich straws have been used for 3 dimensional reconstruction of cosmic ray tracks. In this illuminating field the space dependent response of scintillators and a straw tube were studied.

Contents

List of Figures

List of Tables

Chapter 1

Introduction

1.1 Motivation

High energy physics deals basically with the study of the ultimate constituents of matter and nature of the interactions between them. Experimental research in this field of science is carried out with particle accelerators and their associated detection equipment. High energies are necessary for two reasons; first, in order to localize the investigations to very small scales of distance associated with the elementary constituents, secondly many of the fundamental constituents have large masses and require correspondingly high energies for creation and study.

Nearly seventy years ago, only a few elementary particles the proton, neutron, the electron and neutrino, together with the electromagnetic field quantum photon were known. The universe as we know it today appears indeed to be composed almost entirely of these particles. However, attempts to understand the details of the nuclear force between protons and neutrons, as well as to follow up the pioneering discoveries of new, unstable particles observed in the cosmic rays, led to the construction of ever larger accelerators and to the observation of many new particles. These so-called *"hadrons"* or strongly interacting particles are unstable under terrestrial conditions but are otherwise just as fundamental as the familiar proton and neutron [1]. Our present model of the constituents of matter is that they consist of fundamental point like spin 1/2 fermions the *quarks* [2], with fractional electric charges and the *leptons*, like the electron and neutrino, carrying integral charges.

The known quarks are listed in Table-1.1 ([3]). Quarks are always confined in compound

Quark	Electric charge (e)	Mass
u (Up)	2/3	2-8 MeV
d (Down)	-1/3	5-15 MeV
c (Charmed)	2/3	1-1.6 GeV
s (Strange)	-1/3	100-300 MeV
t (Top)	2/3	168-192 GeV
b (Bottom)	-1/3	4.1-4.5 GeV

Table 1.1: Quarks with their charges and masses.

systems which extend over distances of about $1fm$. The most elementary quark systems are *baryons* which have net quark number three, and mesons which have net quark number zero.

In Table-1.2 some baryons and mesons together with their quark contents, electric charges, masses, life times and decay modes are listed (the values are taken from [4]).

Particle	Quark content	Electric charge (e)	Mass (MeV)	$c\tau$	Decay Mode
p	uud	1	938.27		
n	ddu	0	939.56	$2.65 * 10^8 km$	$pe^-\bar{\nu}_e$
Σ^+	uus	1	1189.37	2.4 cm	$p\pi^0(51.6\%)$ $n\pi^+(48.3\%)$
Σ^0	uds	0	1192.64	$2.2 * 10^{-11}m$	$\Lambda\gamma$
Σ^-	dds	-1	1197.45	$4.4cm$	$n\pi^-(99.8\%)$
Λ	uds	0	1115.68	$7.89cm$	$p\pi^-(63.9\%)$ $n\pi^0(35.8\%)$
π^+	u$\bar{\text{d}}$	1	139.57	$7.80cm$	$\mu^+\nu_\mu(99.99\%)$
π^-	d$\bar{\text{u}}$	-1	139.57	$7.80cm$	$\mu^+\nu_\mu(99.99\%)$
π^0	(u$\bar{\text{u}}$+d$\bar{\text{d}}$)/$\sqrt{2}$	0	134.97	$25nm$	$2\gamma(98.8\%)$ $e^+e^-\gamma(1.2\%)$
K^+	u$\bar{\text{s}}$	1	493.68	$3.71m$	$\mu^+\nu_\mu(63.5\%)$ $\pi^+\pi^0(21.2\%)$
K^-	s$\bar{\text{u}}$	-1	493.68	$3.71m$	$\mu^+\nu_\mu(63.5\%)$ $\pi^+\pi^0(21.2\%)$

Table 1.2: Some baryons and mesons together with their quark contents, electric charges, masses, life times and decay modes.

Quantum Chromodynamics (QCD) is considered to be the underlying theory of the strong interaction, with quarks and gluons as fundamental degrees of freedom.

QCD is simple and well understood at short-distance scales, much shorter than the size of a nucleon ($< 10^{-15}$m) [5]. In this regime, the basic quark-gluon interaction is sufficiently weak. Here, perturbation theory can be applied, a calculation technique of high predictive power yielding accurate results when the coupling strength is small. In fact, many processes at high energies can quantitatively be described by perturbative QCD within this approximation.

The perturbative approach fails when the distance among quarks becomes comparable to the size of the nucleon, the characteristic dimension of our microscopic world. Under these conditions, the force among the quarks becomes so strong that they cannot be further separated. This unusual behavior is related to the self-interaction of gluons: gluons do not only interact with quarks but also with each other, leading to the formation of gluonic flux tubes connecting the quarks [6]. As a consequence, quarks have never been observed as free particles and are confined within hadrons, complex particles made of 3 quarks (baryons) or a quark-antiquark pair (mesons). Baryons and mesons are the relevant degrees of freedom in our environment.

In the domain of low energies and momentum transfers ($q^2 \sim 1-5GeV^2$, medium-energy physics) analytical QCD calculations are not reliable. In this domain, the useful methods are: the chiral effective theory, lattice calculations and meson exchange models [7]. In these theories, the properties of nuclei and nuclear reactions are described in terms of nucleons and mesons, interacting on a scale of 1 fm or larger. The nucleon-nucleon interaction at these distances is described by potentials derived from meson exchange models and adjusted to experimental data. The distance of interaction is governed by the mass of the meson. Light pions ($\pi^{0,+,-}$) mediate the long- and medium-distance interactions ($> 0.7fm$, *attractive*); heavy mesons (ω, ρ) are responsible for a strong short-range force (repulsive) [8].

The physics program at the medium energy hadron accelerators (TRIUMF, LAMPF, PSI, LEAR, SATURNE, IUCF, CELSIUS and COSY) was and is focusing on studies of the production and the decay of light mesons and baryon resonances and the conservation or violation of symmetries [9].

Investigations of the production of mesons and their interactions with nucleons are based on measurements determining the total and differential production cross sections and their dependence on the energy of the interacting nucleons. When one wants to study excited hadrons then the detector has to measure their stable decay products. This means that in the exit there are normally more than two outgoing particles. To establish a comprehensive description of the medium-energy physics, high quality measurements are needed, for which two very important requirements have to be fulfilled:

- a high acceptance detector system
- a beam of high quality and intensity

1.2 Scattering Experiments

Much of what we know about nuclei and elementary particles, the forces and interactions in atoms and nuclei has been learned from scattering experiments, in which atoms in a target bombarded with beams of particles [10]. The earliest were the alpha-particle scattering experiments of Ernest Rutherford. In 1906, to probe the structure of the atom, Rutherford observed the deflection of alpha particles as they pass through bulk matter (a thin sheet of gold foil). He observed that alpha particles from radioactive decays occasionally scatter at angles greater than 90^o, which is physically impossible unless they are scattering off something more massive than themselves. This led Rutherford to deduce that the positive charge in an atom is concentrated into a small compact nucleus [11]. Thus, nucleons scattered from atoms at various scattering angles reveal information about the nuclear forces as well as about the structure of nuclei.

The important observables to extract the physics from the scattering experiments are e.g. the energy dependent total cross section $\sigma(\epsilon)$ and the differential cross section $d\sigma/dcos(\theta)$ depending on the angular correlation between entrance and exit directions. Observables are always of the type: number of events per some phase space interval and per number of beam particles. The cross section shows resonance masses M_R and widths Γ_R. The angular distribution $d\sigma/dcos(\theta)$ depends on the square of the wave function and contains information on spin, parity and angular momentum content of the reaction. Excited hadrons appear as peaks in subsystem mass spectra.

In Fig.1.1 a typical scattering experiment illustrated. A stream of particles, all at the same direction and energy, moves through the target (very small spot) where some of the particles interact. The reaction particles are measured by a detector. The scatterer is represented by an area σ called *cross section*. It is the measure of the probability that a scattering can happen. The available beam intensity (n= number of particles per second) and the target thickness ($density \cdot length \cdot N_A\,(Avogadro\ number)$ = target particles per unit area) define the luminosity L ($reaction\, s^{-1}cm^2$) which is:

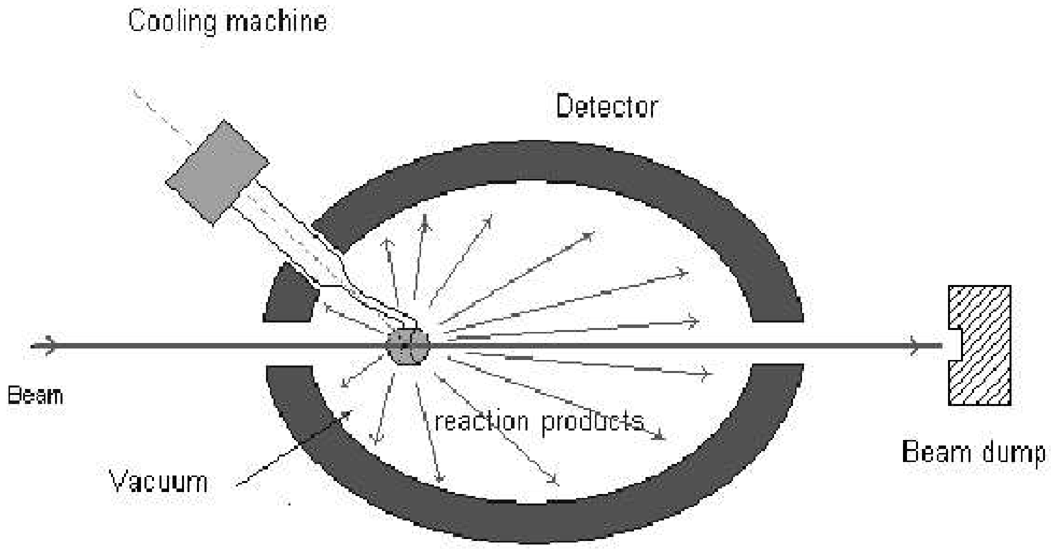

Figure 1.1: Principle of a scattering experiment on an external target. The beam passes through a cell with thin windows, which contains the target material. Reaction products are measured by surroundings detectors which cover the full solid angle in ideal case.

$$L = n \cdot \rho \cdot d \cdot N_A$$

The total reaction rate is given by:

$$Rate = L \cdot \sigma$$

where σ is the cross section of the reaction or interaction probability between particles of the beam and target. The unit of σ is barn ($1mb = 10^{-27}cm^2$). With a $4mm$ thick liquid hydrogen target having the thickness of $1.7 * 10^{22}\,protons/cm^2$ and a proton beam of $10^9\,s^{-1}$, the luminosity is:

$$L = 10^9\,s^{-1} \times 1.7 * 10^{22}\,cm^{-2} = 1.7 * 10^{31}\,cm^{-2}s^{-1}$$

With $\sigma_{pp} = 40mb = 4 * 10^{-26}cm^2$, the reaction rate in the target is $6.8 * 10^5 s^{-1}$. In order to measure the differential cross section, the following informations are needed [12]:

- intensity of the beam,
- total measurement time,
- solid angle coverage of the detector,
- scattering angle,
- number of particles scattered into this solid angle,
- thickness of the target,
- density of the target,
- atomic weight of the target material,
- Avagadro number ($N_A = 6.022 * 10^{23}$)

In general a detector covers only a certain part of the solid angle. One measures the differential cross section defined as:

$$\frac{d\sigma(\theta,\phi)}{d\Omega(\theta,\phi)} = \frac{number\ of\ particle\ scattered\ in\ to\ the\ d\Omega}{j\ (current\ density\ of\ the\ beam)}$$

and tries to extrapolate the full angular range.

If we consider the scattering of particles on a potential $V(r)$ which is only nonzero at $|r| < a$, the scattering process is described in the non-relativistic quantum mechanics by the sum of an incoming plane wave and an outgoing spherical wave [12]:

$$\Psi_T((\vec{r}) = A\left[e^{i\vec{k}\vec{r}} + f(\theta,\phi)\frac{e^{ikr}}{r}\right]$$

where $f(\theta,\phi)$ is the scattering amplitude. The density of the particles is given in quantum mechanics by $P = \Psi^*\Psi$. For incoming particles with the velocity of v_{in}, the current density is $j_{in} = v_{in}P = A^2 v_{in}$. Similarly for the outgoing particles the current density is $j_{out} = v_{out}|\Psi|^2 = v_{out}|f(\theta,\phi)|^2 A^2/r^2$. Using the current densities one can write the differential cross section in terms of scattering amplitude [12]:

$$\frac{d\sigma(\theta,\phi)}{d\Omega(\theta,\phi)} = |f(\theta,\phi)|^2$$

$f(\theta,\phi)$ is:

$$f(\theta,\phi) = \frac{-2\pi m}{h^2}\int e^{i\vec{k}\vec{r'}}V(r')\Psi_T(\vec{r'})d^3r' \tag{1.1}$$

1.3 Event Reconstruction and Feasibility of an Experiment

The detector volume is filled with devices which the particle traverse and in which they leave pieces of information by creating light flashes or movable electric charges (excitation and ionization). The event record of an experiment consists of signals from all particles of an interaction. After sorting out which informations are related to the same particle the kinematical properties of each particle have to be reconstructed to reveal the physical nature of the whole event [13].

In ideal case a detector must

- measure over the complete possible kinematical region for the desired reaction (100 % acceptance)
- make it possible to determine the four vectors $(E, \vec{p})$ of all reaction particles (kinematical completeness)

For kinematically complete events in which all four vectors are known (both in entrance and exit), all possible physical observables can be determined, but the precision which an experiment can reach is limited by

- precision in the kinematical coordinates (four vector components)
- statistical accuracy (number of events per interval)
- amount of background
- efficiency with which the detector and reconstruction procedure cover the phase space of the reaction

The precision in the determination of the four vector of a charged particle depends on the accuracies in the track direction, absolute momentum and identification of the particle mass. Except for the mass, these kinematical quantities can be measured by means of high granularity but approximately massless geometry detectors when particles are charged.

If the detector provides more information than necessary (over constraints) one can and should use the additional information to improve the precision in the event reconstruction by a fit procedure.

If we assume a reaction in which the beam and target particle go into several exit particles $1 + 2 + \cdots$, then we can write for that an equation for the four vectors P:

$$P_{beam} + P_{target} \quad = \quad P_1 + P_2 \cdots$$

In explicit four vector notation, this describes simply four equations for the simultaneous energy and momentum conservation and writes:

$$\begin{pmatrix} E \\ p_x \\ p_y \\ p_z \end{pmatrix}_{beam} + \begin{pmatrix} E \\ p_x \\ p_y \\ p_z \end{pmatrix}_{target} = \begin{pmatrix} E \\ p_x \\ p_y \\ p_z \end{pmatrix}_1 + \begin{pmatrix} E \\ p_x \\ p_y \\ p_z \end{pmatrix}_2 + \cdots \tag{1.2}$$

There holds the relativistic relation between energy and momentum $E_i^2 = m_i^2 + \vec{p_i}^2$ where $\vec{p} = (p_x, p_y, p_z) = |\vec{p}|(n_x, n_y, n_z)$ $\vec{n}$ is the unit vector of direction cosines ($|\vec{n}| = 1$ and $n_x^2 + n_y^2 + n_z^2 = 1$).

In Eq.1.3 an equivalent information to the four vectors (in Eq.1.2) is written.

$$\left|\begin{array}{c} m_b \\ n_{bx} \\ n_{by} \\ \pm|p_b| \end{array}\right| \oplus \left|\begin{array}{c} m_t \\ n_{tx} \\ n_{ty} \\ \pm|p_t| \end{array}\right| \rightarrow \left|\begin{array}{c} m_1 \\ n_{1x} \\ n_{1y} \\ \pm|p_1| \end{array}\right| \oplus \left|\begin{array}{c} m_2 \\ n_{2x} \\ n_{2y} \\ \pm|p_2| \end{array}\right| \tag{1.3}$$

The directional unit vectors $\vec{n}$ are worth only two variables, since $n_z^2 = 1 - n_x^2 + n_y^2$. The sign of n_z is kept in the momentum $\pm|p|$ and distinguishes forward or backward going tracks.

This table allows to count over constraints and thus judge if a given experimental setup provides enough information for a kinematically complete event construction [14].

For example, if we assume a pure geometry detector, for the reaction $pp \rightarrow d\pi^+$ (no velocity measurement for d and π^+), we have:

$$\begin{array}{r|c|c|c|c|c|c|c|l} & p & & p & & d & & \pi^+ & \\ & & & & & & & & \\ m \rightarrow & \surd & & \surd & & \surd & & \surd & \\ n_x \rightarrow & \surd & \oplus & \surd & \rightarrow & \surd & \oplus & \surd & \text{2 overconstraints} \\ n_y \rightarrow & \surd & & \surd & & \surd & & \surd & \\ |p| \rightarrow & \surd & & \surd & & 0 & & 0 & \end{array}$$

where $\surd$ means information produced by detector and 0 no information produced. We have two unknown momenta but four equations from the momentum conservation so we have already two over constraints.

With a time of flight information, giving $\vec{\beta}$ and in turn $\vec{p}$, (together with a mass assumption $\vec{p} = m \cdot \vec{\beta} \cdot \gamma$) we have except the masses no unmeasured information and four over constraints in this case.

$$\begin{array}{|c|c|c|c|c|c|c|l} p & & p & & d & & \pi^+ & \\ & & & & & & & \\ \surd & & \surd & & \surd & & \surd & \\ \surd & \oplus & \surd & \rightarrow & \surd & \oplus & \surd & \text{4 overconstraints} \\ \surd & & \surd & & \surd & & \surd & \\ \surd & & \surd & & \surd & & \surd & \end{array}$$

An example of three outgoing particles with a charged particle detector (like TOF) is

$$p_{beam} + p_{target} \rightarrow p + p + \pi^0 \ (or\ \gamma,\ or\ "nothing")$$

We have the following information about the reaction (from geometry and time of flight informations).

$$\left|\begin{array}{c} p \\ \\ \surd \\ \surd \\ \surd \\ \surd \end{array}\right| \oplus \left|\begin{array}{c} p \\ \\ \surd \\ \surd \\ \surd \\ \surd \end{array}\right| \rightarrow \left|\begin{array}{c} p \\ \\ \surd \\ \surd \\ \surd \\ \surd \end{array}\right| \oplus \left|\begin{array}{c} p \\ \\ \surd \\ \surd \\ \surd \\ \surd \end{array}\right| \oplus \left|\begin{array}{c} \pi^0\ (\gamma) \\ \\ \surd \\ 0 \\ 0 \\ 0 \end{array}\right| \quad \text{1 overconstraint}$$

In this case, we have three unknowns (momentum of the neutral particle) and 1 over constraint.

At low energy close to the π^0 threshold and with a time of flight information for the two protons three different hypothesis for the neutral particle are possible, pion, photon or nothing. This reaction $pp \rightarrow ppX^0$ was published by TOF [15]. A detector, having good enough resolution, allows to evaluate all three channels since the over constraint gives selectivity.

Chapter 2

Experimental System

2.1 COSY Accelerator

COSY is a cooler synchrotron and storage ring depicted in Fig.2.1. It delivers very high precision polarized and unpolarized beams of upto $\approx 2 * 10^{11}$ protons and deuterons per machine cycle in the momentum range from $300 MeV/c$ to $3600 MeV/c$ [16, 17]. This goal is accomplished by using an electron cooling system and a stochastic cooling system.

The electron cooler of COSY is designed for electron energies up to $100 keV$, thus to cool protons up to a momentum of $600 MeV/c$ [18, 19]. An electron beam guided in parallel to the protons (deuterons) reduces; the transversal and longitudinal momentum by friction and makes phase-space-dense ion beams before acceleration to a requested energy [20]. Electron cooling is used after stripping injection of H^- or D^- ions. With the stochastic cooling covering the range from $1.5 GeV/c$ up to maximum momentum, deviations from the beam are determined for sub samples of the beam and then in each turn a correction on the samples is applied. From turn to turn new samples are prepared by mixing [21, 22].

The beam preparation needs 2 to $12 sec$ (acceleration upto $2 sec$, electron cooling upto $10 sec$). The spill out time can be stretched from few seconds to minutes by stochastic extraction. On internal targets operation times can be upto hours for one cycle if stochastic cooling compensates the beam blow up by the target.

The COSY consists of two sources for unpolarized H^-/D^- - ions and one for polarized H^- -/ D^-- ions, the injector cyclotron JULIC that accelerates the H^- - ions up $300 MeV/c$ and D^- - ions up $600 MeV/c$, the cooler ring COSY with a circumference of 184 m delivering protons up desired momentum [16, 23]. Injection into COSY takes place via charge exchange of the H^-- or D^-- ions over $20 ms$ with a linearly decreasing closed orbit bump at the position of the stripper foil. The polarized source presently delivers $8.5 \mu A$ of polarized H^- - ions [23].

Four internal target areas (ANKE, COSY-11, COSY-13, EDDA) are available for experiments with a circulating beam. The beam can also be extracted via the stochastic extraction mechanism and is guided to three external experiment areas (magnetic spectrometer BIG KARL, Time Of Flight spectrometer TOF and JESSICA). The emittance of the extracted cooled beam is only $\epsilon = 0.4\pi \ mm \ mrad$ [24].

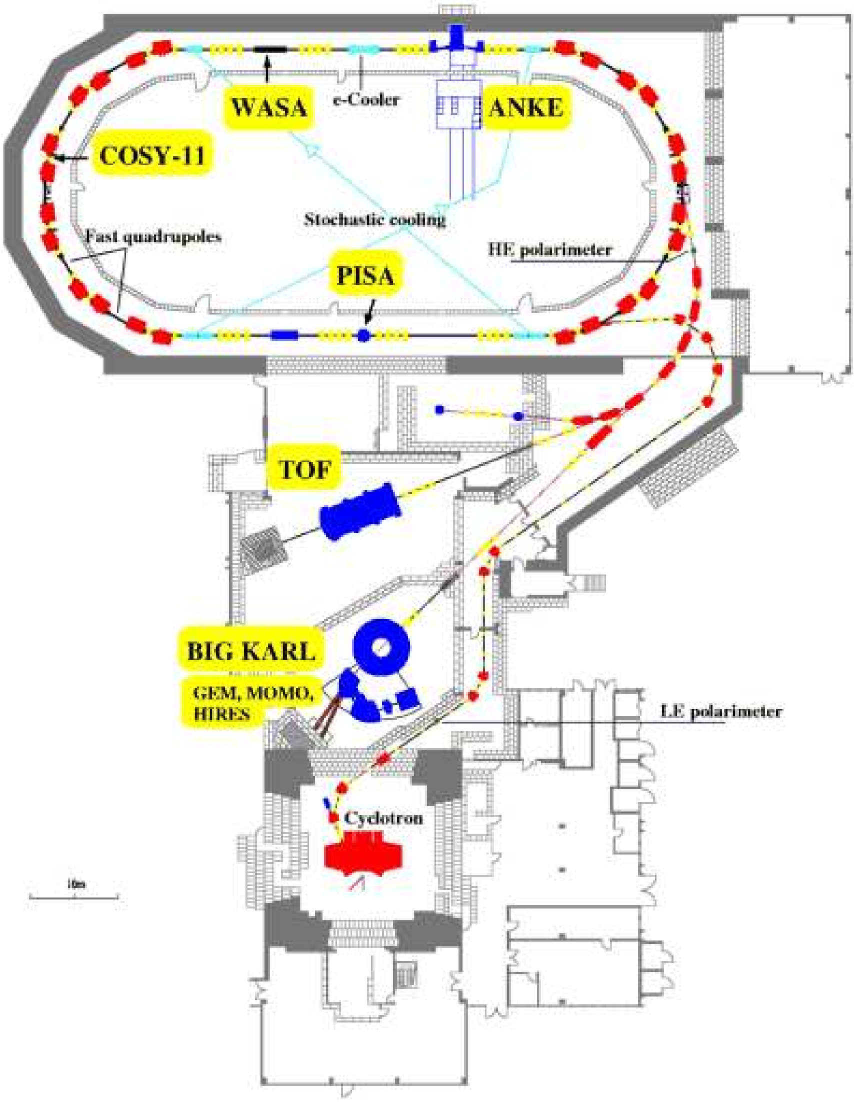

Figure 2.1: The COSY accelerator at the research center Jülich and the positions of experiments on internal and external targets.

2.1.1 Physics in COSY

The COSY accelerator with the energy range and beam quality that it provides, makes it possible to study the structure of mesons and baryons in the confinement regime of QCD. This field includes the analysis of decay properties of mesons and baryon excitations and interactions of meson meson, meson baryon and baryon baryon systems. The experimental studies are characterized by keywords like threshold measurements (it is possible due to the high quality of beam and target. Beam diameters at targets are available with divergencies below $1 mrad.$), strangeness production, final state interaction, medium modification and reaction mechanisms [25].

Threshold measurements are instructive for the interpretation of elementary interactions. The relative velocities of the ejectiles are low which favors s-waves and final state interactions. At threshold the momentum transfer is high since incoming particles have high and the outgoing particles have small center of mass momenta. The transfer is practically the center of mass momentum of the input channel. This large momentum transfer and s-wave dominance at threshold enhance heavy meson exchanges [26].

The strangeness production is an excellent tool to study hadron dynamics [27]. Due to the high selectivity for the detection of delayed decays of hyperons and K_s mesons it is experimentally particularly precise. Questions concerning the strangeness content of the nucleons and the reaction mechanisms for the dissociation can be addressed by such studies. For the $pp \rightarrow pK^+\Lambda$ [28] reaction it is comparatively easy and precise to measure the Λ polarization via the asymmetry of the parity violating weak decay $\Lambda \rightarrow p\pi^-$. In a simple quark model this is related to the s-quark polarization. With a polarized beam and polarized target a detailed analysis of the spin degrees of freedom can be done in Λ production reactions.

Modifications of the properties and interactions of hadrons within the nuclear medium are another interesting field. Questions here are for example the lifetime of hyper nuclei, specific reaction mechanisms and possible medium effects especially on K-mesons which may be isolated in *subthreshold* production experiments [29].

With COSY a wealth of experimental data has been accumulated during the last decade, which differ to previous measurements with respect to the quality and the amount of the data. Fig.2.2 gives an overview of the world data (including COSY) on total cross sections in pp interactions below $4 GeV/c$ beam momentum.

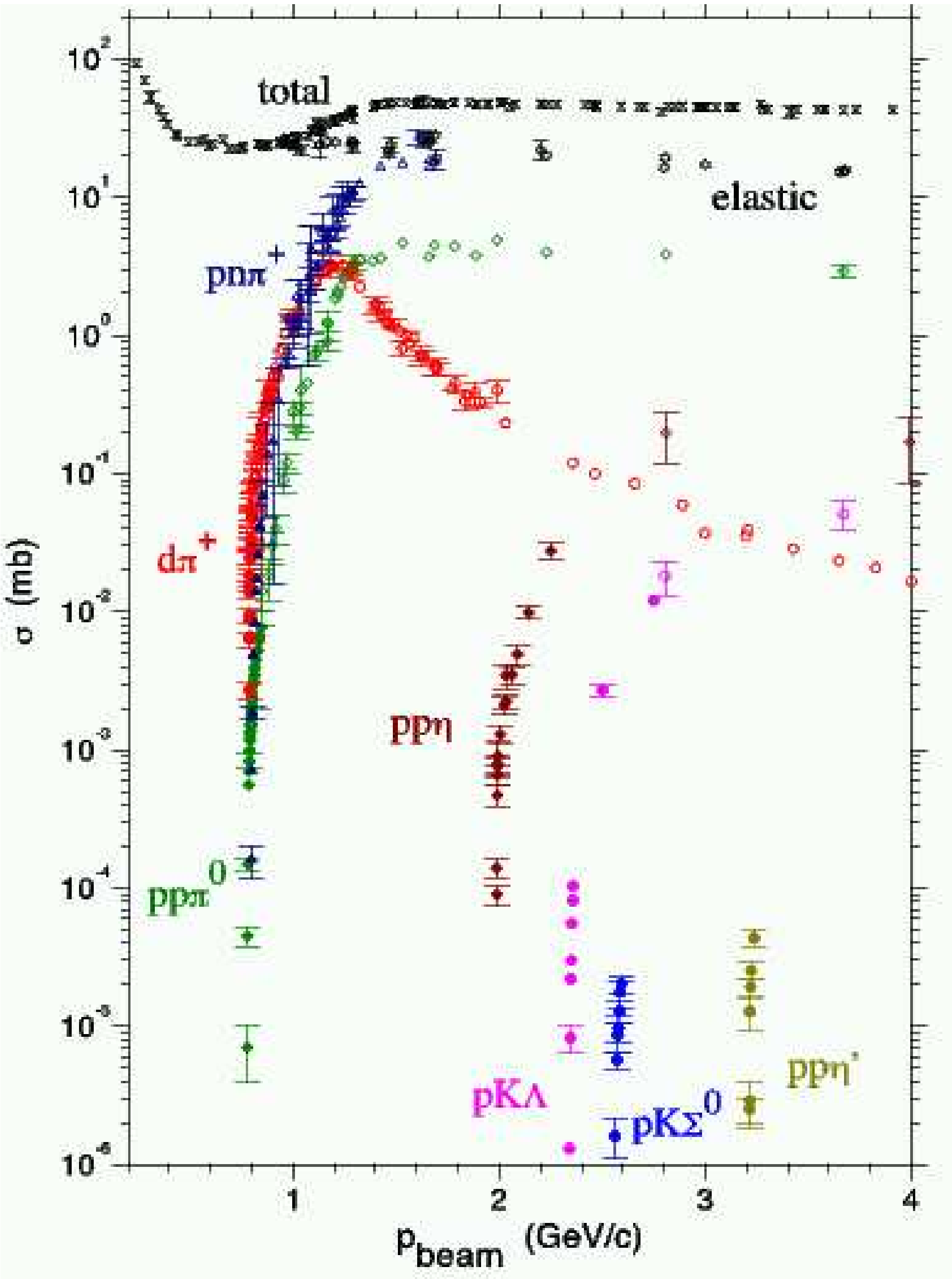

Figure 2.2: Cross sections for pp interactions as a function of the beam momentum (data from CELSIUS, COSY, IUCF, SATURNE). Figure is taken from [26]

2.2 COSY-TOF Detector System

Highly sophisticated detector systems are in operation either at the internal COSY beam or located at extracted beams in external areas. The time-of-flight spectrometer TOF is one of the main experimental facilities at the external beam lines of the COSY.

The investigations at COSY-TOF [30] concentrate mainly on the light and medium mass meson production, proton-proton bremsstrahlung and associated strangeness meson-baryon production by measuring following reactions

- $pp \rightarrow pK^+\Lambda$, $pK^+\Sigma^0$, $pK_s^0\Sigma^+$ [28, 31, 32, 33]
- $pp \rightarrow pp$, $pp\gamma$, $pp\pi^0$, $pp\eta$, $pp\eta'$ [15, 34, 35, 36, 37, 38]
- $pp \rightarrow pn\pi^+$, $d\pi^+$, $pp\pi^+\pi^-$, $pp\omega$ [39, 40]
- $pd \rightarrow^3 He\eta$, $^3He\eta'$, $^3He\omega$ [41]

The COSY-TOF spectrometer is designed as a scintillator hodoscope for stable charged particles covering about 2π solid angle in the laboratory system. The main components of the TOF spectrometer are a liquid hydrogen target, a start detector, tracker system and a system of three stop detector segments, forming a cylinder barrel with a circular endcap (Fig.2.3). The endcap consists of two concentric circular hodoscopes. Up to 3 barrel elements can be combined with the two planar front hodoscopes of 1.16 and 3 m outer diameter, providing very large solid angle coverage without holes. Fig.2.3 shows the TOF spectrometer in a 3 m long version. With two more existing barrel sections the maximal flight path in vacuum can be extended to more than $8m$. Since the typical velocities of the particles in the momentum range of COSY are between approximately 25% and 99% of the speed of light [42], the flight lengths must amount to some meters in order to be able to determine the velocity sufficiently well with the available time resolution of $2.5 * 10^{-10} sec$ (average over all detectors) [42].

The spectrometer components are housed in a big vacuum tank [43]. So it is guaranteed that beam particles and reaction products do not undergo reactions with air, which would lead to many non-target originated events and to straggling.

A very important advantage of TOF is the absence of a vacuum tube for the beam. Such a tube would occupy space for detectors at small angles and reaction particles would have to penetrate very thick layers of this tube if they are at small forward angles. TOF detectors can be (and they are) positioned millimeters away from the passing cooled primary beam. This is particularly advantageous if one is going to detect $\Lambda \rightarrow p\pi^+$ or $K_s \rightarrow \pi^-\pi^+$ decays which have decay vertices close to the beam in the few cm distance from the target. TOF is unbeatable best suited for reaction studies with Λ and K_s.

In order to calibrate the time measurement, the start and stop scintillators are connected to a nitrogen laser UV light calibration system by quartz light guides.

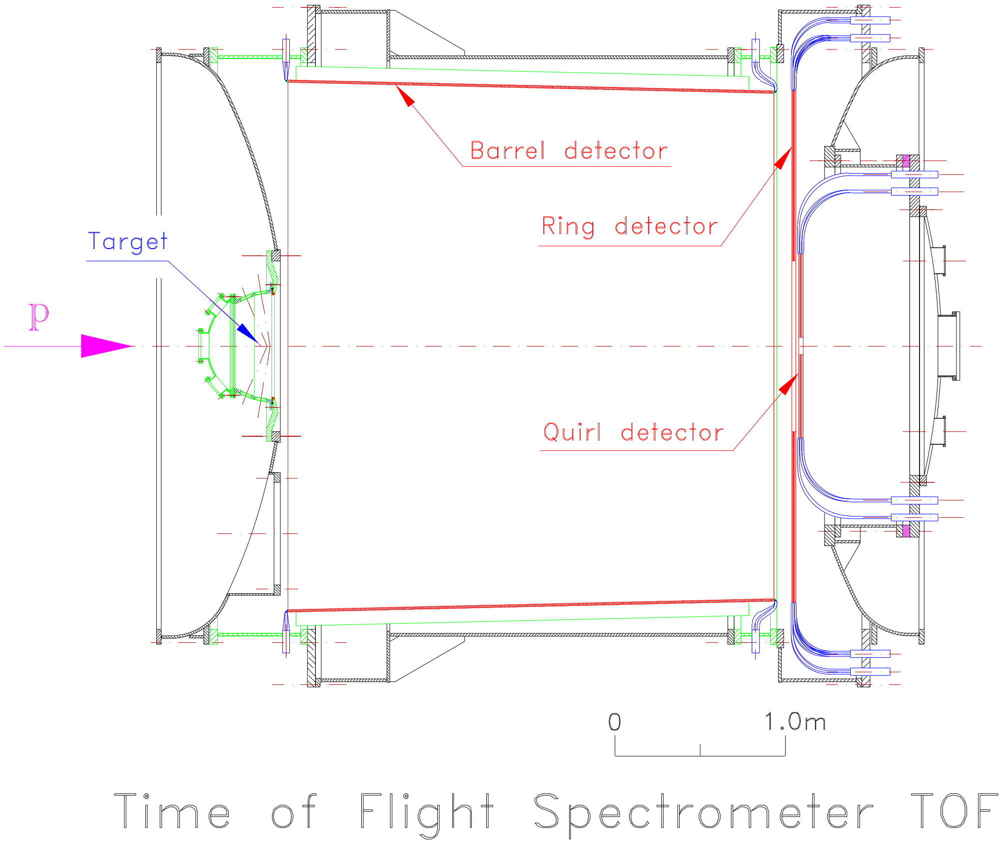

Figure 2.3: The COSY-TOF Detector. The beam enters from left, passes through the small cryotarget and the evacuated tank. Start detector and tracker are close to the target. The big stop detector hodoscopes cover the inner surface of the vacuum tank.

2.2.1 Target system

A very light liquid hydrogen (or deuterium) target (Fig.2.4), which is very small in order to take advantage of the excellent beam quality of COSY, has been developed and used for the external experiments at COSY [44]. Since hydrogen or deuterium are gases and have very low densities at room temperature and atmospheric pressure (0.08 g/l for H_2 and 0.166 g/l forD_2), leading to reduction of the reaction probability, they are liquefied. The liquid target with its very small amount of inactive material and thin beam windows is installed in the entrance of the TOF tank in a section with good vacuum of $10^{-6} - 10^{-7} mbar$. The target construction is affected by the following requirements [45]:

- It has to stabilize the target temperature within $\pm 0.05K$ in the range of liquid hydrogen/deuterium
- The windows for the beam inlet and exit through the target cell have to be very thin but nevertheless planar
- The target thickness has to be well defined. Therefore, the target liquid should have homogenous density without any bubbles
- The time needed for large temperature changes during cooling down to the working temperature or heating up to the room temperature has to be as short as possible
- The cooling system and the heat conductors have to occupy minimum space and minimum solid angle. There must be minimum mass in the target region in order to reduce background events and shadowing effects on reaction products before they can reach detectors
- the target should have axial symmetry

The target system used in the TOF experiments has a target cell with $6mm$ in diameter and normally $4mm$ in length. It has very thin windows of $0.9\mu m$ Mylar foil. This is achieved by a stabilized pressure difference over windows of $\leq 0.2mbar$ in all conditions [46, 47]. The small dimensions of the target minimize the background due to double scattering and enable measurements very close to threshold. If we consider the delayed decays of strange particles occurring a few centimeters after their production in the target, the target length therefore should be much smaller than the decay length of a few centimeters to get a well defined interaction vertex. This is important for high quality kinematical reconstruction and understanding of the reactions. The very thin window foils reduce the background events from reactions on heavier nuclei in the target window foils, the energy losses and straggling of the outgoing ejectiles. With the beam from COSY of $\approx 0.7mm\emptyset$ and $4mm\ lH_2$ thickness we obtain routinely a reaction vertex definition within $< 2mm^3$. This has big advantages for geometrical reconstruction and background identification.

In order to keep the target in optimum conditions (constant temperature and stable density), a heat pipe-target system is developed [48, 49]. It is a closed system, which has an evaporator and condenser section where the target material acts as a working fluid which evaporates and condenses. The condenser section and evaporator section (target cell) are connected by a transport (or adiabatic) section that bridges large distances. Heat applied to the evaporator section by an external source radiation vaporizes the working fluid. The resulting vapor pressure drives the vapor through the adiabatic section to the condenser, where the vapor condenses, releasing the latent heat of vaporization to the heat sink (cooling machine). The condensed liquid flows down to the evaporator section for re-evaporation. This gravity assisted circulation provides a stable dynamic equilibrium. The target material is liquefied by using a cooling machine. The cooling time of the system for H_2/D_2 from room temperature (300K) to 15/19K is 50/45 minutes respectively [46].

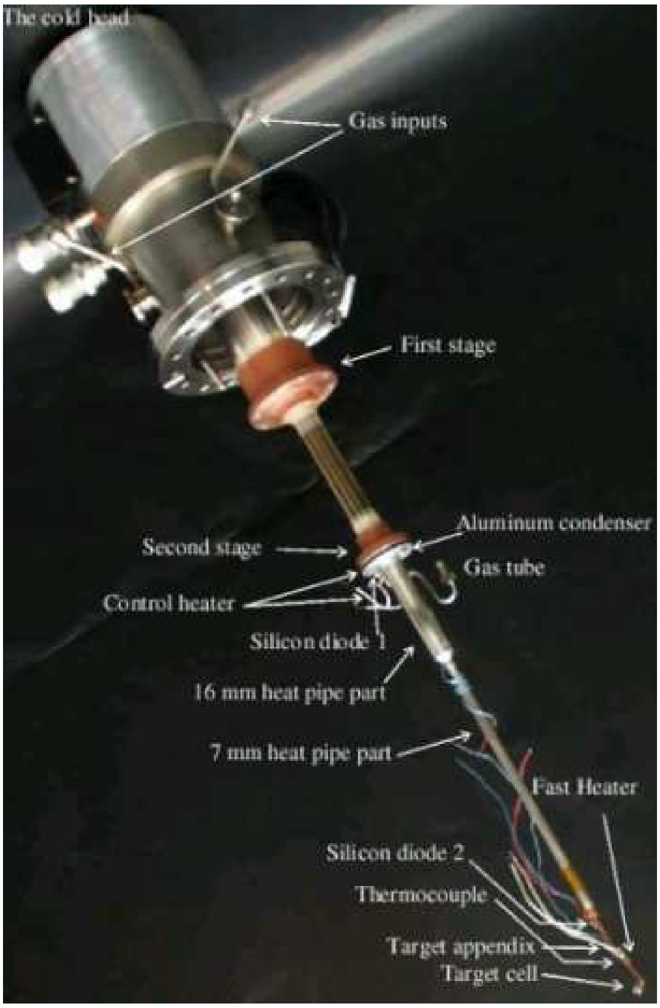

Figure 2.4: The target system. The cold parts below the flange are in vacuum. The necessary super isolation is removed in the picture.

2.2.2 Start Detector

The actual start detector consists of two circular layers of 12 wedge shaped plastic scintillator sectors ($\delta\phi = 30^o$) with $1mm$ thickness, placed in a distance of $23mm$ behind the target [50]. They deliver a reference signal for the time of flight measurement with the resolution of $\sigma = 170ps$. In order to cover the gaps between the wedges, the two layers are rotated to each other by 15^o leading to a ϕ information in steps of 15^o. Its outer radius is $76\,mm$. In the center there is a hole of $1.4\,mm$ radius for the beam.

2.2.3 Tracker

After the start detector, there is the *"Erlanger tracker"* detector (Fig.2.5), made especially to investigate the strangeness and hyperon-production [51]. Its goal is track and vertex reconstruction. It consists of a Si-μ Strip detector followed by two fiber hodoscopes providing geometry informations for the tracks of charged particles.

The Si-μ Strip detector with a thickness of $520\mu m$ is $30mm$ far from the target. It is made of 100 concentric rings ($\Delta r = 280\mu m$) on one side and 128 in ϕ segmented elements ($\Delta\phi = 2.81^o$) on the other side. The detector has an outer radius of $31mm$ and a beam hole with a radius of $3.1mm$. The 12800 pixels of the detector provide high resolution in determination of the track direction. The detector also provides energy loss information [52].

Two fiber hodoscopes complete the tracker detector system. They are made from $2 \times 2mm^2$ quadratic scintillating fibers, covered by cladding of about $0.1mm$ thickness. The first one placed $100mm$ downstream from the target, consists of two layers each of 96 scintillating fibers which are rotated 90^o relative to each other. In 2004 a new third plane is added to the existing system in order to increase the reconstruction efficiency. The second one is placed 200 mm far from the target and made of two times 192 fibers. It covers the active area of $1475cm^2$. Besides the energy loss of the particles, points for the primary and secondary tracks are provided by the fiber hodoscopes.

The straw tracker, having much higher resolution, much more depth and less mass, much larger surface will replace these fiber hodoscopes at the end of 2006. It will improve the overall performance of the experiments.

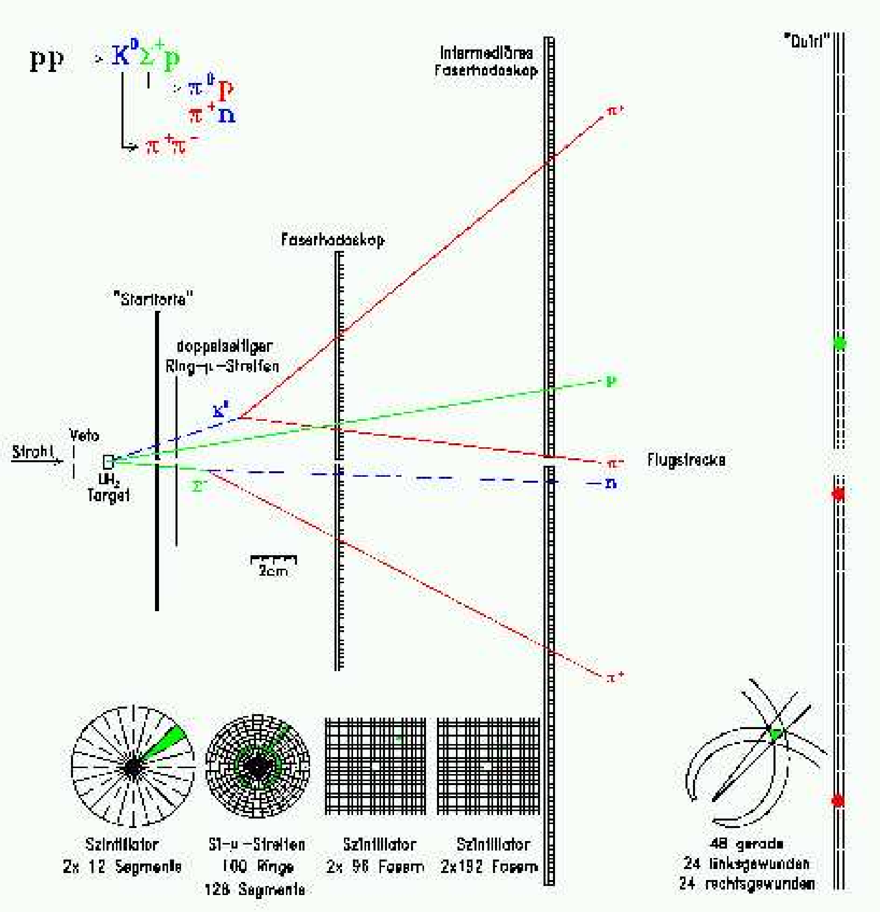

Figure 2.5: Schematic view of the actual start detector and tracking system (Erlanger start detector).

2.2.4 Stop Detector

The Quirl Ring and Barrel detectors constitute the stop detector Fig.2.6. There are no acceptance holes between these three components [53]. The barrel hodoscope consists of one layer of 96 straight scintillators which are read out from both sides [54]. It covers the large reaction angles and provides time and position information by averaging the response of the two photomultipliers at each end of the scintillator bars.

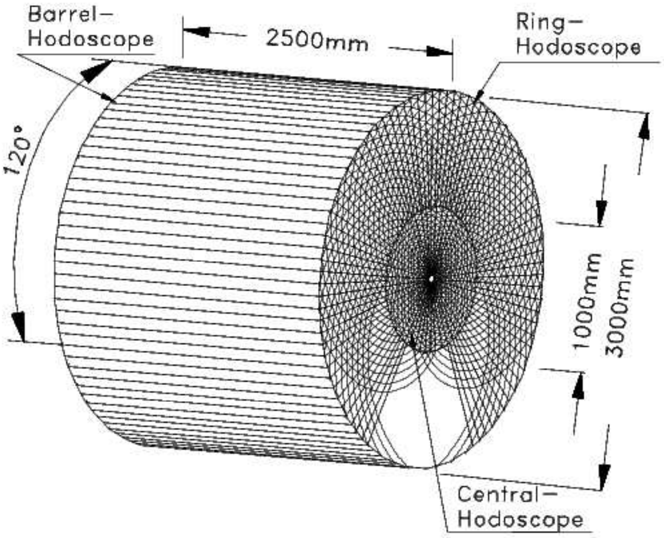

Figure 2.6: A sketch of the TOF spectrometer shows the Quirl, the Ring and one of the barrels

The central hodoscope ("quirl") is a 3-layer (each 0.5 cm thick) scintillation counter having the inner- and outer radius of $4.2cm$ and $58cm$. The first layer is divided into 48 wedge shaped sectors ($\Delta\phi = 7.5^o$). The second and third layers consist of 24 left- and 24 right wound (Archimedes) spirals. The relationship between ϕ and r is $r(\phi) = \frac{r_{max}}{\phi_{max}}\phi$ where $r_{max} = 58$ cm and $\phi_{max} = 180^o$ [52]. The overlapping area between three elements fired by a passing particle forms a triangular pixel giving the direction of the track (Fig.2.7). This type of hodoscope was originally invented and build for measurements at the LEAR/JETSET experiments and then for CELSIUS/WASA. The advantage of the three layer geometry is also that more than one passing particle tracks can be determined unambiguously. Since all scintillator elements are symmetric under rotations around the beam axis in steps of the azimuthal angular width of an element, the Quirl detector plane is divided into equal, radially symmetric areas. Therefore, all individual scintillators in a plane are exposed to the same integral counting rate as they cover identical parts of the phase space [55]. Furthermore the hodoscope gives a fast online multiplicity and timing trigger and allows for dE/dx measurements.

The ring detector consists also of three layers of $5mm$ thick scintillator material. It has an inner- and outer diameter of $1.136m$ and $3.08m$. The design is basically the same as that of the Quirl detector. The much larger surface of the ring detector is divided into 96 straight segments and 48 left- and right spirals with only 120^o winding angle for the bent scintillators [55].

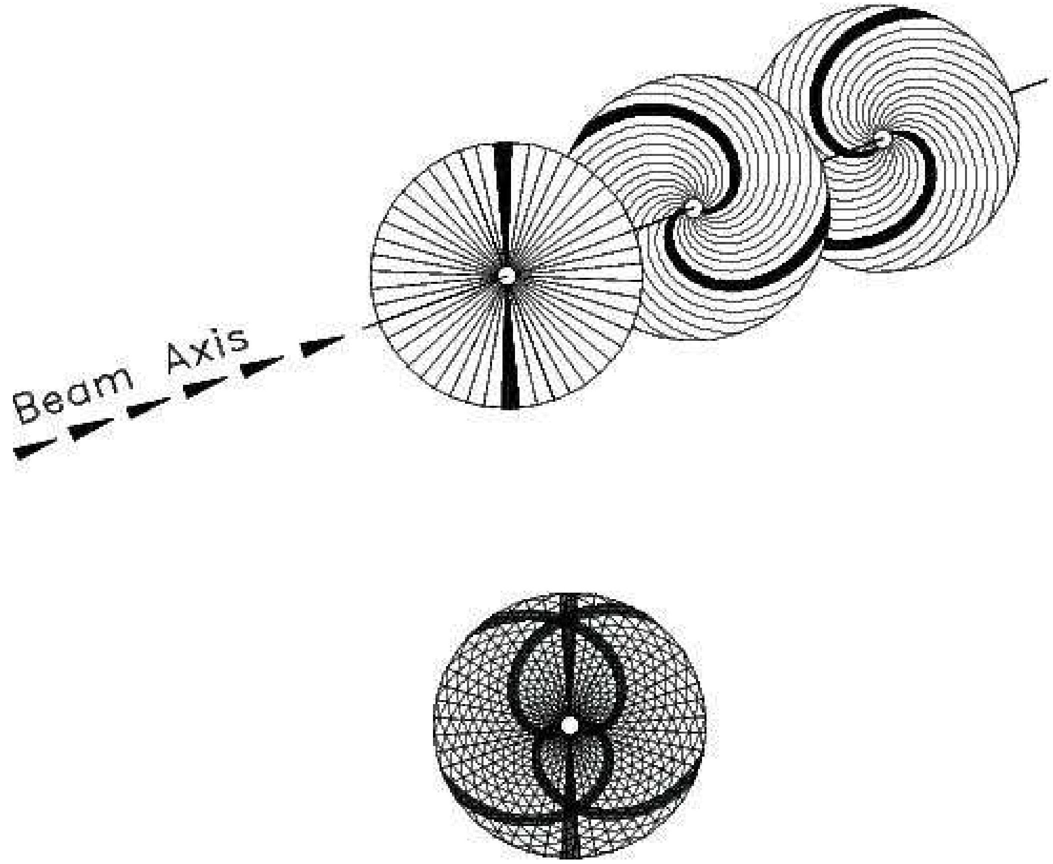

Figure 2.7: Schematic view of the Quirl detector showing the three layers. The elements which are hit by two particles are indicated in black

Chapter 3

New Geometry Spectrometer "Straw Tracker" for COSY-TOF

3.1 Requirements for the Straw Tracker

The time of flight spectrometer TOF will be extended by a much better tracking system with higher resolution, much higher sampling density, and lower mass [56, 57]. Three thousand *straw tubes* arranged in 15 double planes will replace the existing tracking detector (fiber hodoscopes) of COSY-TOF.

The straw tracker will be placed behind the μ-strip detector and ≈ 6 *cm* down stream from the target. It will improve

- track resolution
- efficiency of the event reconstruction
- acceptance
- transparency

in COSY-TOF experiments.

For reactions with two or three charged particles in the final state the particle momenta can be determined by measuring the direction vectors alone (see chapter 6). In this case better angular and position (track resolution) resolution directly improves the momentum resolution.

Examples of such reactions are $pp \rightarrow d\pi^+$, $pp \rightarrow pK^+\Lambda$ $(\Lambda \rightarrow p\pi^-)$. In the last reaction the direction of the neutral Λ hyperon can be determined by its production and decay vertex and decay plane. Both are given in first approximation by points of closest approach between the p and K tracks and the secondary p and π^- tracks, respectively. An intersection criterion on the simultaneous line fits must be imposed for the more precise final geometrical vertex determination. The momentum of a Λ can also be calculated from the decay angles of p and π^- with respect to the Λ track [58]. One main goal of the new track detector is to improve the decay vertex reconstruction, to determine all the geometrical information for $pK\Lambda$ much more precisely than now.

Due to its high resolution (better than $200\mu m$, see 5.8) and high sampling (30 planes = 30 coordinates per track), angular and position resolution will be increased significantly. This will improve the precision of all four vector components and exclude ambiguities.

If we compare θ resolution of the first fiber hodoscope with 2 mm thick fibers and placed $100mm$ away from the target, we find $\approx 20mrad$ $(arctan(2/100))$, for a single straw at the same distance from the target with the worst resolution of 0.2 mm, 10 times higher resolution of $\approx 2mrad$ is obtained. One should notice that with 30 track points the track resolution will be much better than 0.1 mm in position and $0.5mrad$ in direction.

One of the main topics studied in the COSY-TOF experiments is hyperon production. Since the hyperons decay typically in the first 80 mm and therefore in front of the fiber hodoscopes ($c\tau_{\Sigma^+} = 24\,mm$, $c\tau_{\Sigma^-} = 44\,mm$, $c\tau_{\Lambda} = 78.9\,mm$), the fibers are successful in reconstructing these decay patterns. But the weak points of these detectors is that due to the low sampling (only two space points per track) and limited resolution, there are rather frequently ambiguities from tracks crossing each other at the same detector elements which can not be solved (see Fig.3.1). The straw tracker with high sampling and much better resolution will solve such ambiguities very easily and in this way it will increase the efficiency of the event reconstruction.

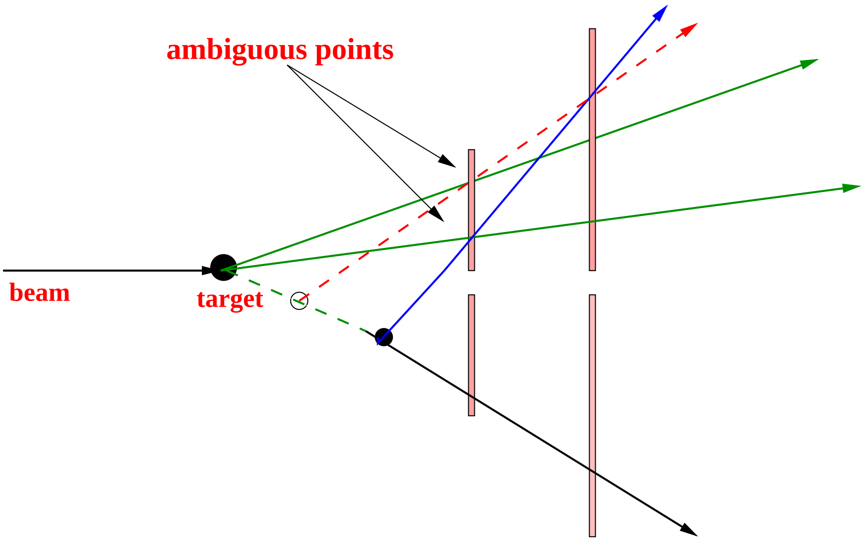

Figure 3.1: Two hodoscope planes can fake two possible Λ decay vertices due to insufficient information.

Moreover the straw detector will help to identify the tracks of charged π and K before they decay inside the TOF detector. The decay length L of a particle with mass m in the lab system is related to its intrinsic lifetime τ and its relativistic velocity β or to its mass and momentum p by:

$$L = c\tau\beta\gamma = c\tau p/m$$

For a charged π (K) meson with lifetime $\tau = 2.6 * 10^{-8}$ $(\tau = 1.24 * 10^{-8})$ we find $c\tau = 7.8m$ $(3.7m)$. With a momentum of say $p = 100MeV/c$ the decay length $L = 7.8/1.4 = 5.6m$

(0.74m). This means, that within $\approx 6cm$ flight pass 1% of the $\pi^{\pm}$ mesons (8% of the $K^{\pm}$ mesons) decay. If one finds such a meson track within the first 12 cm flight pass then one has a 98% (84%) chance to have the correct track direction [56]. It needs a very good tracker in order to avoid efficiency problems in reactions with several mesons.

Very important is the acceptance of a detector, its solid angle coverage. The solid angle Ω that an object covers at a point is defined as the surface area, S, of a projection of that object onto the sphere centered at that point, and can be written as $\Omega = S/R^2$ [59]. In Table-3.1 the acceptances of the first and second Fiber Hodoscopes and straw tracker at the same position are given. They are calculated from $\Delta\Omega = 2\pi(1 - cos\theta_{det})/2$ [14] by assuming circular detectors, instead of squares (taking into account that overlap areas of the detector planes in different orientation can be approximated to the circle) to make the calculation easier. Therefore $20 \times 20\ cm^2$ ($40 \times 40\ cm^2$) first fiber (second) hodoscope is replaced by circle of 20 cm (40 cm) diameter, crossing straw double planes ($100 \times 100\ cm^2$) by a circle of 100 cm diameter, at their position in the TOF and straw tracker. The increase in the acceptance due to the straw tracker is nearly 2.8 times at the first and 2.1 times at the second fiber hodoscope's position.

Detector/distance (from the target)	$\Delta\Omega$ of inscribed circles	percent of (4π)
first fiber hodo./20 cm	1.84	14.6%
straw tracker/20 cm	5.05	40.0%
second fiber hodo./40 cm	1.84	14.6%
straw tracker/40 cm	3.95	31.4%

Table 3.1: Circular acceptances of the first and second Fiber Hodoscopes (at their position in the TOF) and straw tracker planes at the same positions.

During the experiment all reaction products pass through the detectors and interact with the material of the detector by means of electromagnetic and strong interactions. This leads to straggling and secondary reactions. Massless construction (transparency) is a very important issue to avoid these unwanted effects.

The thickness of the two fiber hodoscopes is $4 \times 2 = 8mm$ scintillator. A particle traverses a thickness X in radiation length (X_0) of $X/X_0 \approx 0.019$ in the fiber hodoscopes. A particle through all 30 straw layers (the avarage Mylar thickness of 30 straw planes is $< 3mm$) on the other hand traverses only a thickness of $X/X_0 \approx 0.013$, dominated by the total Mylar film thickness and including gas (82/18% Ar/CO_2), anode wires, and aluminization of the Mylar film. The amount of matter for a track through the passive detector end part is $X/X_0 \approx 0.018$, including tube end plug, crimp pin, cathode belt and frame bar. Therefore, the whole straw tracker shows the same high transparency in all directions and minimum shadowing of the following detectors in the COSY-TOF barrel [60].

The straggling angle amounts to $\Theta_{strg} \cong \sqrt{\frac{X}{X_{rad}}}(20MeV/c)/(p\beta)$ [4], where $\frac{X}{X_{rad}}$ is the thickness of the scattering medium in radiation length. Angular imperfections project back into imperfections especially in vertex positions derived from track intersections. To reduce the effect of the straggling in the vertex reconstruction, the larger the straggling the shorter the distance must be over which a back projection is made. In other words, only reducing straggling as much as possible allows to stay with the sensitive tracker volume far enough from the target position where the track density may be easily too high.

A "massless" construction is also needed in order to avoid secondary hadronic reactions. They could spoil the track pattern or result in shadowing effects on subsequent detector components thus cutting into the acceptance. This is a demanding criterion not only for the sensitive parts but also for the mechanical structure material, like stretching frames or mounting and adjustment devices and electronic or gas supply components. The overpressure in the straw tubes is the trick which allows to avoid heavy frame construction in the TOF straw tracker.

3.2 The Jülich Straws

The straw tubes shown in Fig-3.2 consist of $1m$ long Mylar tubes with a diameter of $10mm$ aluminized on the inner surface. The wall thickness is $30\mu m$. Mylar is the preferred material because of its well suited mechanical properties like a high Young's modulus and tensile strength compared with Kapton [57]. Young's Modulus (also known as modulus of elasticity or tensile modulus) is a measure of the stiffness of a given material. Young's modulus (measured in pascals), Y, can be calculated by dividing the tensile stress by the tensile strain [61]:

$$Y \equiv \frac{tensile\ stress}{tensile\ strain} = \frac{F/A_0}{\Delta l/l_0} \tag{3.1}$$

where F is the force applied to the object; A_0 is the original cross-sectional area through which the force is applied; Δl is the amount by which the length of the object changes; and l_0 is the original length of the object.

The advantage of a higher Young's modulus is the possibility to avoid large changes of the tube length under pressure and therefore to hold the wire tension nearly constant over a larger pressure range.

Lightweight plastic end-caps glued into both ends of the Mylar tube provide gas tightness. The end-caps have a $3mm$ diameter and $5mm$ long cylindrical extension with a central hole for the crimp pins between which the counting tungsten wires with radius of 10μ are

Figure 3.2: Construction elements for a single straw tube: aluminized Mylar tube, 1 $cm\,\emptyset$ end caps with gas tubes, counting wire going through all elements and crimp pins which are finally glued into the 3 $mm\,\emptyset$ extensions which are used for transversal fixation.

stretched. These extensions are also used for a precise transversal fixation of all tubes on both ends in belts with precisely positioned holes. Gas flow is provided through thin plastic tubes which are glued into the end caps. Fig.3.3 shows the end structure of the straw tubes with crimp pins contacting the counting wires and springs providing cathode contacts between inner aluminum layer of the Mylar tubes and positioning belt. The weight of a single straw tube is $< 2.5g$ [56].

Figure 3.3: End structure of the straw double plane. The springs provide cathode contacting. The crimp pins make contact to the conducting wires. The straws are fixed transversally by positioning the $3mm\,\emptyset$ cylindrical extensions of the end-caps in corresponding holes in a $> 1m$ long belt. The conductive belt is removed.

Anode Wire	W97/Re3, Au-plated (4%)	$\rho = 19.3g/cm^3$, $\sigma = 6.3mg/L$ $R/L = 314\Omega/m$ (DC-resistance)
Cathode Tube	Mylar film, aluminized	$\rho = 1.4g/cm^3$ $R/L = 40\Omega/m$ $C/L \approx 9.8pF/m$

Table 3.2: Anode wire and Cathode tube properties

The simple but new idea of this detector development is to use the anyhow existing excess pressure inside the tubes in the TOF vacuum tank to create the necessary wire tension and mechanical stability. $1bar$ overpressure creates on the $1cm$ diameter end-caps an axial force ($7.85N$) which is enough to make the tubes self-supporting and supply the force ($0.4N$) to stretch the counting wire. This means, that massive frame constructions are not necessary [57]. As thickness defining element and in order to assure correct tube positions and rectangular shape, each plane has a window like frame made of Rohacell (plastic foam density $0.05g/cm^3$) reinforced by $0.3mm$ carbon fiber compound plates. Into this frame also the adjustment belts are integrated. They provide at the same time the cathode contacts to each tube via springs which connect the aluminization of the tubes with a copper layer on the belts (Fig.3.3)[56]. In order to prevent the bending of the straws due to the gravitation the tubes are glued to each other once with small drops of glue at about half length in the closely-packed double-layers [60].

Two planes (each has 104 straw tubes) in the double plane are arranged on top of each other by an half tube diameter offset to cover the low efficient regions near to the tube walls. 15 such double plane modules will be stacked on to each other and rotated by 120^o in order to allow for unambiguous multi track reconstruction. Frames and tubes of adjacent double planes lie flat on each other and stabilize each other in beam direction. A free passage of the primary beam through the double planes is provided by cutting out $1cm$ in the center from two central one meter straws in each plane. This gives an aperture of $\approx 1cm\,\emptyset$ throughout the full stack. Fig.3.4 shows the arrangement of three double planes constructed. The full set of straws plus preamplifiers will have a mass of about only $7.5kg$. With the reinforced Rohacell it was possible to construct a frame of about the same mass including the gas distributor and electronic contacts, so that the complete tracking detector has a total mass of about $15kg$ only. It is worth noting, that the ≈ 3000 signal cables of $5m$ length and $0.5mm$ diameter end up with a mass of $\approx 30kg$ comparable to the detector mass. One sees, that it makes sense to use very thin cables.

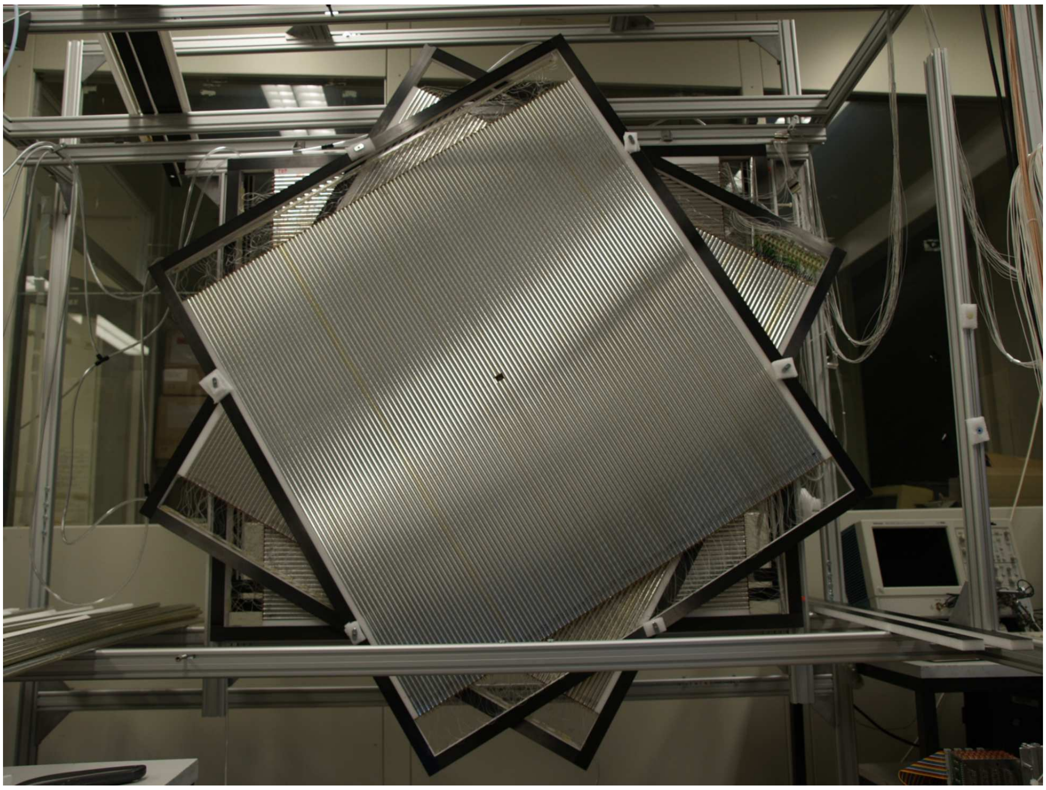

Figure 3.4: Three straw frames mounted in steps of 120^o around the beam direction. One also sees the central aperture for beam passage.

3.3 Basic Principles of the Straw Tube

Straw tubes are drift chambers (first operation drift chamber [62]) made of a gas filled conducting cylinder acting as cathode, and a sense wire stretched in the axis of the cylinder.

The electromagnetic interaction between the charged particles traversing the gas inside straw tube forms the basis of detection. Coulomb interactions between the incoming charged particles and bound electrons in the gaseous medium result in ionization. Due to the applied static electric field in the tube, electrons of primary ionization will drift to the positively charged anode wire and positive ions will move to the cathode. Since the electric field in the straw tube increases with r^{-1} towards the anode wire, in the vicinity of the thin wire (at $r_c = few\, wire\, radii$) the electric field gets strong enough so that electrons produced by the primary interaction can gain enough energy to produce an avalanche like secondary ionization process called gas amplification. In Fig.3.5 the gas amplification is depicted. A typical drop like ionization distribution close to the anode wire develops with all electrons in the front towards the wire surface and ions outside. Because of lateral diffusion and the small radius of the anode, the avalanche surrounds the wire; electrons are collected and positive ions start to drift towards the cathode. From the gas amplification or avalanche, signal amplification of $10^4 - 10^6$ is obtained [63]. This leads to a significant simplification of the measurement electronics. Signals produced by the collected charges are further amplified by exterior electronics and processed by a data acquisition system (DAQ). The track of a particle is mapped from the fired wires by registering the drift times of the electrons. Using these drift times, one can obtain the distance of closest approach of the track to the anode wire Fig.3.6. In a single straw the coordinate information is a *"cylinder of closest approach"*.

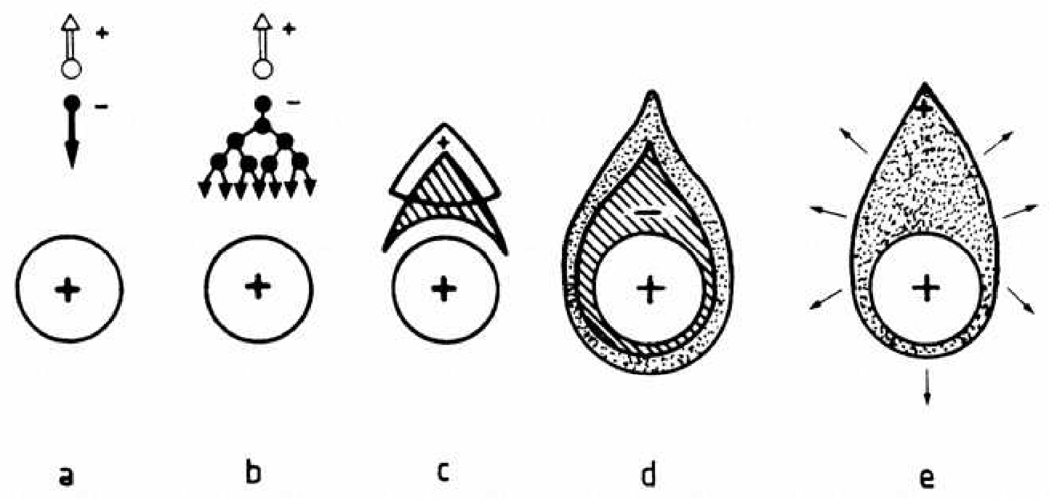

Figure 3.5: Time development of an avalanche in the Straw tube

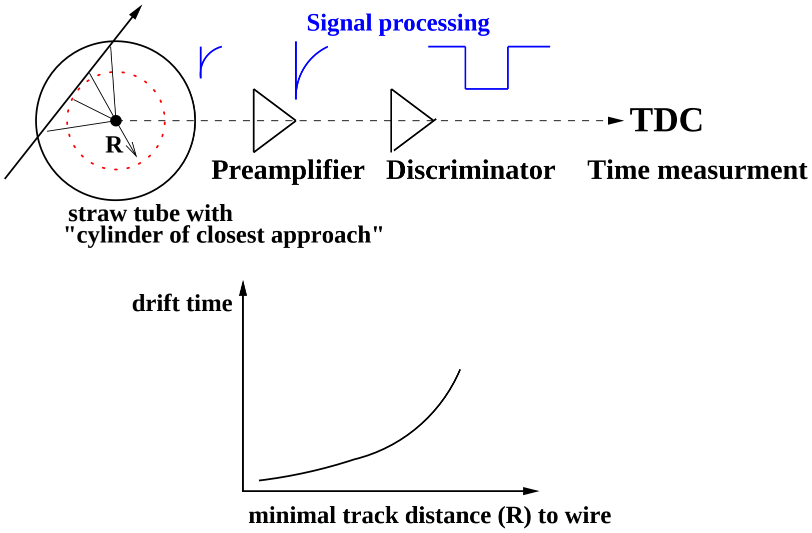

Figure 3.6: Time difference between creation of movable charges in the gas on the particle track and appearance of an avalanche signal on the counting wire. The coordinate information from a single straw is a ”cylinder of closest approach” [62].

3.4 Basic Physics of Particle Detection in a Straw Tube

3.4.1 Ionization Process

When a charged particle passes through a gas, it will lose a part of its kinetic energy in the medium by means of electromagnetic interaction. Energy transfer from the charged particle leads to ionization of the gas along the path of the traversing particle. An expression for the average differential energy loss due to ionization has been obtained by Bethe and Livingston in the framework of relativistic quantum mechanics [64]. The number of primary electron-ion pairs (N_p) depends on the atomic number, density and ionization potential of the gas, and on the energy and charge of the incident particle. The created primary electrons may have sufficient energy to ionize further and create secondary electron-ion pairs (clusters). The overall outcome of the two processes is called total ionization. The total number of electron-ion pairs per cm is denoted by N_t. These numbers have been measured and computed for a variety of gases [63, 65, 66, 67, 68, 69, 70]. Table 3.3 lists some values for N_p and N_t (taken from [71]), along with other general properties. All numbers are given for normal temperature and pressure.

Fig.3.7 shows the differential energy loses for various materials over a $\beta\gamma$ scale. dE/dx decreases fast due to β^{-2} dependence and reaches a minimum around $\beta\gamma = 3$ to 4 (minimum ionization) and then starts to increase logarithmically (relativistic rise) as $\beta \rightarrow 1$ [72]. The minimum ionization energy for most materials is equal to about 2 $MeVg^{-1}cm^2$ [63].

The ionization energy loss is statistically distributed around its mean value. The distribution, often referred to as energy straggling, is approximately Gaussian for thick absorbers, but develops asymmetry and a tail towards high energies for decreasing thickness. The high energy tail is related to the quasi free electron scattering in forward direction. It becomes a

Gas	Z	A	E_x (eV)	E_i (eV)	W_i eV	dE/dx (keV/cm)	N_p (cm^{-1})	N_t (cm^{-1})	X_0 (m)
He	2	4	19.8	24.5	41	0.32	4.2	8	745
CH_4	10	16	9.8	15.2	28	1.48	25	53	646
Ar	18	39.9	11.6	15.7	26	2.44	23	94	110
CO_2	22	44	5.2	13.7	33	3.01	35.5	91	183
C_2H_6	34	58	6.5	10.6	23	5.93	84	195	169
Xe	54	131.3	8.4	12.1	22	6.76	44	307	15

Table 3.3: Some properties of different gases. Z and A are charge and atomic weight. E_X, E_i excitation and ionization energy respectively, W_i is the average energy required to produce one electron-ion pair in the gas, dE/dx is the most probable energy loss by a minimum ionizing particle, X_0 is the radiation length.

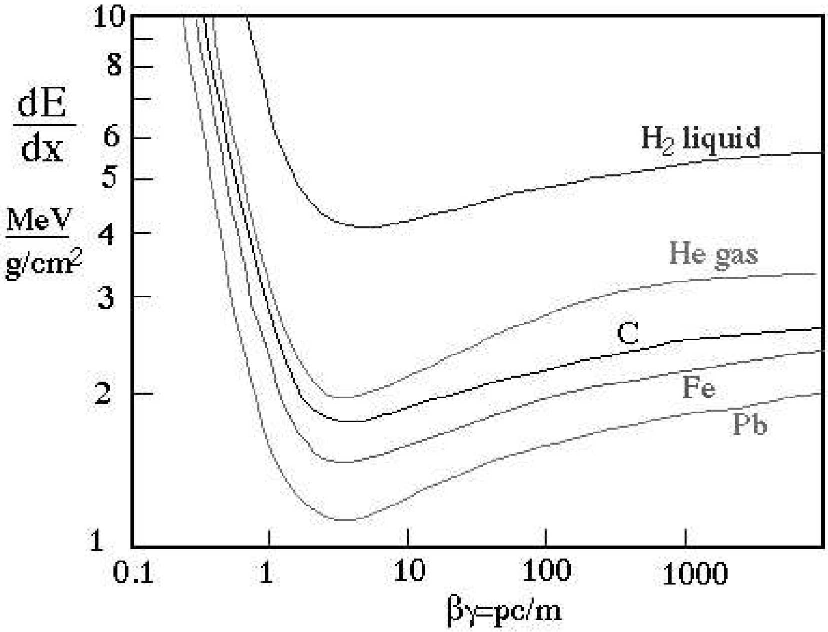

Figure 3.7: Ionization energy loss rate in various materials. The figure is taken from [73]

Landau distribution for very thin absorbers [74, 75].

An approximate expression for the probability of an electron emission with the energy E is given by [76]:

$$\begin{aligned} \frac{dP(E)}{dEdx} &= \frac{1}{E^2}\frac{2\pi N_A Z\rho e^4}{m_e c^2 A\beta^2} = \frac{W}{E^2} \\ W &= \frac{2\pi N_A Z\rho e^4}{m_e c^2 A\beta^2} \end{aligned} \tag{3.2}$$

where Z, A, ρ are the the atomic number, mass and the density of the medium, m_e, e mass and charge of the electron.

Due to the $1/E^2$ dependence of electron emission probability (Eq.3.2), electrons having low energy dominate in the ionization. Electrons ejected with an energy above a few keV up to a few hundred keV are called δ-rays. Their range can be approximated in g/cm^2 by [63]

$$R_p = 0.71 E^{1.72} \tag{3.3}$$

where E is the δ-electron energy in MeV.

Integrating the Eq.3.2, one can obtain an expression for the number of electrons $N(E \geq E_0)$ having an energy E_0 or larger as

$$N(E \geq E_0) = \int_{E_0}^{E_M} P(E)dE = W(\frac{1}{E_0} - \frac{1}{E_M}) \approx \frac{W}{E_0} \tag{3.4}$$

One can derive by combining Eq.3.3 and Eq.3.2, that in $1cm$ of argon, one out of five minimum ionizing particles eject a δ-electron with a range $10\mu m$ and only one out of twenty particles can produce a $3keV$ electron with a range more than $100\mu m$. Thus, the track of a projectile is determined precisely from the cluster positions.

3.4.2 Drift and Diffusion of Electrons in Gases

The motion of an electron in the gas is governed by two physical phenomena: drift and diffusion. In the absence of electric field the free electrons in a gas will move randomly with an agitation energy given by the Maxwell formula, $3/2\,kT$ (about 4.10^{-2} eV at 18 ^0C) and experience collisions with the gas molecules [71]. If an electric field is applied, then the original Maxwellian energy distribution becomes more complicated since the electrons start moving along the electric field. The free electrons will continue to have nondirectional velocity v (and energy ϵ) but they will exhibit drift along the field direction, with a mean drift velocity v_d. This drift velocity of electrons is determined by the cross sections and electric field. The average drift velocity, mean thermal velocity v, energy ϵ and the diffusion coefficient are given in terms of the mean fractional energy loss per collision by [77]:

$$v_d \approx [\frac{2}{3}(\frac{1}{3}\Lambda)^{1/2} eEl_e/m]^{1/2} \tag{3.5}$$

$$< \epsilon > \approx (3\Lambda)^{-1/2} eEl_e \tag{3.6}$$

$$v = [2(3\Lambda)^{-1/2} eEl_e/m]^{1/2} \tag{3.7}$$

$$D = [\frac{2}{9}(3\Lambda)^{-1/2} eEl_e/m]^{1/2} \tag{3.8}$$

where Λ is the mean fractional energy loss in a collision, l_e mean free path of the electrons (and inversely proportional to cross section), E electric field, and e, m charge and mass of the electron.

It is seen that the shorter the mean free path, the lower the drift velocity, the thermal velocity, and the diffusion coefficient. It is also seen from Eq.3.5, that with increasing mean fractional energy loss per collision, the drift velocity increases too.

One needs to know mean fractional energy loss per collision and mean free path or cross sections to get the drift velocity and diffusion coefficient. The Λ can be obtained from the Boltzmann transport equation "classical theory of electrons in gases". The solution of the equation is discussed in [78, 79]. The electron collisions cross sections for argon and carbon-dioxide are given in Fig.3.8 and Fig.3.9. As seen in in Fig.3.9, the behavior of electrons in molecular gases is much more complicated than pure gases due to the additional excitation modes (rotational and vibrational). The vibrational and rotational excitation cross sections dominating in the energy range $0.1 - 10\,eV$ result in the mean fractional energy loss being large and the mean electron thermal energy ϵ being low.

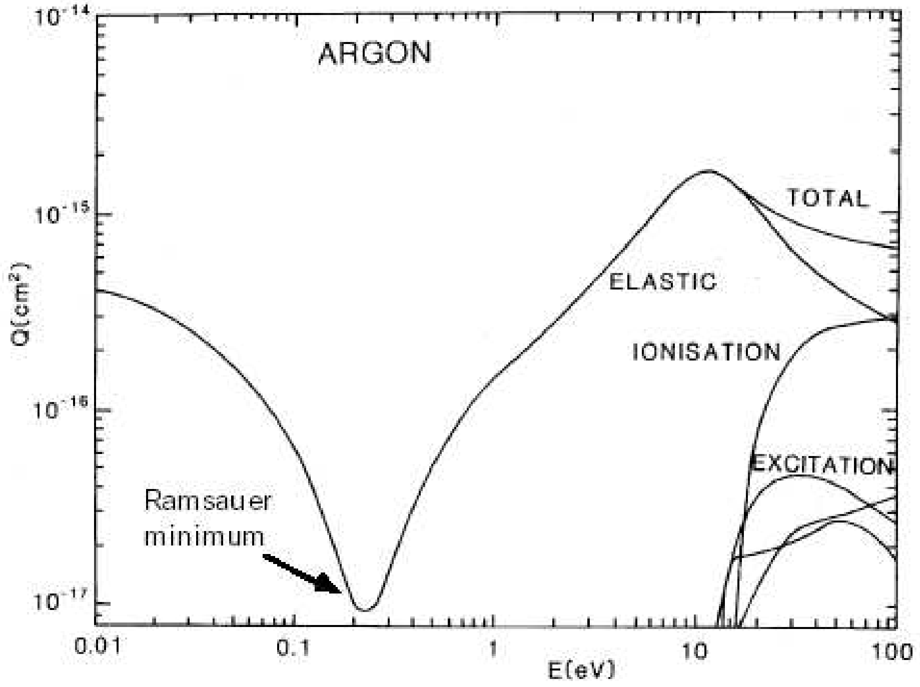

Figure 3.8: Cross sections for electron collisions in *Ar*. The figure is taken from [71]

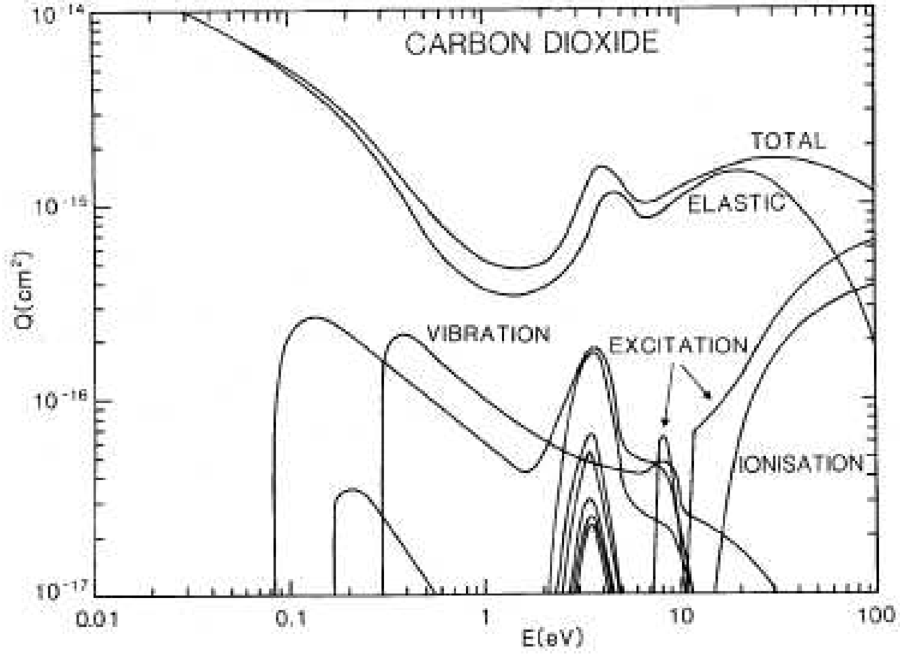

Figure 3.9: Cross sections for electron collisions in CO_2. The figure is taken from [71]

3.4.3 Gas Amplification

The electrons formed in the primary ionization process by the incident radiation move in the electric field inside the active counter volume towards the anode gaining energy from the field and colliding with the gas molecules. Each electron formed in an additional ionizing collision moves again toward the anode gaining energy eventually causing new ionizing collisions. In such a way an electron avalanche develops in the electric field, and the number of electrons reaching the anode is much higher than the number of electrons initially produced by the ionizing particle.This is called gas amplification.

The mean gas amplification factor M (gas gain) is defined as the number of avalanche electrons produced by each initial electron and by its successors as it travels towards the central wire:

$$M = \frac{N_e}{n} \tag{3.9}$$

where N_e is the total number of electrons collected at the anode and n is the number of initial electrons directly formed by ionization radiation.

The gas gain M is determined by the chamber geometry, the operating voltage, filling gas or gas mixture, and the gas pressure. Using the assumptions that the gas multiplication is only due to the accelerated electrons, photoelectric effects are negligible, no electron is lost in negative ion formation or recombination, then the mean gas amplification factor M is written as [80]:

$$ln\, M = \int_a^b \alpha(r)dr \tag{3.10}$$

where a and b are the anode and cathode positions, respectively, and $\alpha(r)$ is the first Townsend ionization coefficient defined as the mean number of electrons produced by a free electron per unit pathlength in an electric field. This parameter depends on the nature of the gas, its pressure P, and applied electric field strength E. In a cylindrical proportional counter with the anode of radius a, and cathode (cylinder) of radius b, the electric field strength $E(r)$ at the radius r produced by a potential difference V between the cathode and the anode is

$$E(r) = \frac{V}{rln(a/b)} \tag{3.11}$$

To exclude the pressure dependence of the ionization coefficient one usually defines the reduced ionization coefficient, α/P, and the reduced electric field strength $S = E/P$. Since the electric field in a cylindrical counter varies with the position (Eq.3.11), it is usually characterized by its reduced strength at the anode surface, S_a. The general expression for the gas amplification factor then becomes [80]:

$$ln\, M = K \int_{S_c}^{S_a} \alpha(r)dr \tag{3.12}$$

where $K = V/ln(b/a)$, the integration in Eq.3.12 is carried out over the counter radius, $a < r < b$, but it may be limited to the region where gas amplification is possible, i.e., from the anode radius a to the critical radius r_c beyond which the field is too low to support the gas amplification. S_c is the reduced electric field strengths at the critical radius r_c. In practice the evaluation of the integral fails because of the limited knowledge of α. It is difficult to find a single analytical function that describes all the regions of the α curve equally well. There were attempts to approximate some regions of the α/P by various analytical forms leading to various expressions for the gas amplification factor. A general formula for α/P derived from theoretical consideration of gas ionization by electrons in an electric field was proposed by Aoyama [81]. The applicability of the general approach for the large number of gases and gas mixtures used in proportional counters was verified. The reduced ionization coefficient thus obtained is

$$\frac{\alpha}{P} = AS^m exp(-BS^{m-1}) \tag{3.13}$$

where A, B and m ($0 < m < 1$) are coefficients which have to be determined experimentally. When α/P is substituted into Eq.3.12 and the integration carried out, the reduced gas gain becomes

$$ln\,\frac{M}{K} = \frac{A}{(1-m)B}[exp(-BS_a^{m-1}) - exp(-BS_c^{m-1})] \tag{3.14}$$

It was found that $m = 0.65$ describes well measurements with noble gas hydrocarbon mixtures and pure hydrocarbon. Table 3.4 gives the parameters used for several gases and mixtures [82].

Gas	$A(1/Torr\,mm)$	$B(kV/Torr\,mm)^m)$	m
Ar	1.40	0.018	1.0
CO_2	2.0	0.0466	1.0
$0.9\,Ar/0.1\,CH_4$	1.844	0.1044	0.65
Xe	2.60	0.035	1.0
N_2	1.2	0.0342	1.0

Table 3.4: Experimental parameters for different gases.

3.4.4 Gas Mixtures

The operating characteristics of a gaseous detector are highly dependent on the gas mix. One can select it for one or more of the following criteria:

- stability; low tendency to spurious discharges
- good detection efficiency; good amplification
- drift velocity; could be either slow (for good position measurement) or fast, for small dead time
- non-flammability; for safety
- low diffusion; for better time and space resolution
- minimum aging effects; for longer operational life of the detector

Chapter 4

Straw Electronics

4.1 Straw Signal

When a charged particle traverses a straw filled with $ArCO_2$ gas, it leaves an ionization trail of 50 to 60 clusters/cm (1-2 ion electron pair per cluster) inside the tube [63]. The time development of the avalanche and of the detected signal begin at a few wire radii, i.e. typically at less than $50\mu m$ from the anode surface. Taking a typical value of $5cm/\mu sec$ for the drift velocity of electrons in this region, it appears that, in less than $1nsec$ all electrons are collected on the anode wire. On the other hand, collection time of the ions is in the order of hundred microsecond very long compared to the electron collection time due to their heavy mass and decreasing velocity towards the cathode and the long distance from wire to cathode. Fig.4.1 shows time development of the straw signal together with signals obtained from several differentiation time constants. It is characterized by an initial burst of current (electron component), that comprises ≈ 1% of the total charge integrated over

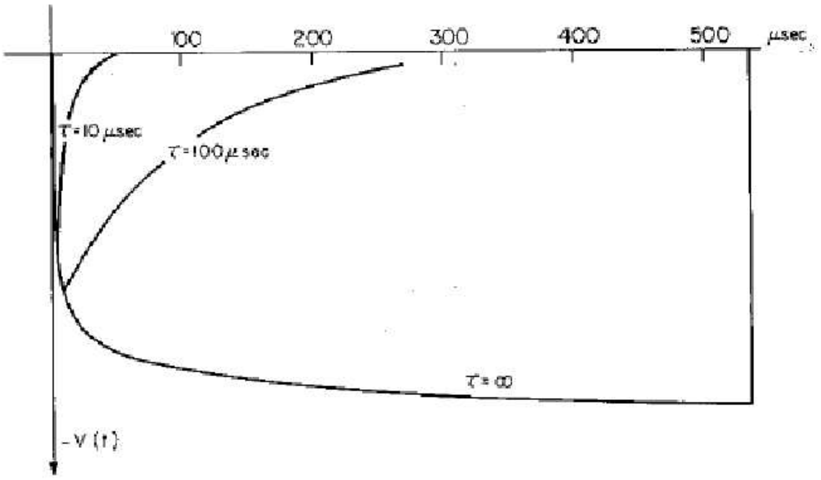

Figure 4.1: Time development of the pulse in the straw tube. The pulse shape obtained with several differentiation time constants is also shown. Figure is taken from [63]

the full ion drift time, and a remaining signal (ion tail) controlled by the motion of the ions. Ion movement in the high field close to the wire is still fast enough to contribute to a steep current signal which can be used for timing purposes.

Since the long ion tail would increase the dead time of the detector, elimination of the ion tail is one of the most crucial goals of the front-end electronics design. Only the first very fast response is used for the timing and the rest of the signal is canceled by employing a passive network that sharply differentiates the straw signal.

Main requirements for the electronics of the straw detector are:

- signal shaping corresponding to the detector properties
- low noise
- precise timing
- low per-channel cost
- low crosstalk

The straw tracker electronics consists of preamplifier, ASD-8 input board, ASD-8 chip containing amplifier and discriminator (analog to digital converter), and ECL converter (Fig.4.2).

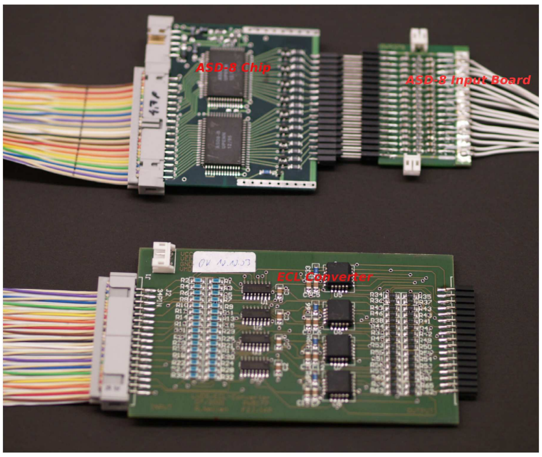

Figure 4.2: Picture of the ASD-8 chip (upper left), ASD-8 input board (upper right) and ECL converter (lower)

4.2 Preamplifier

The ASD-8 chips will be placed outside of the TOF tank in air for cooling reasons and in order to minimize the amount of material in the detection region. The analog signal from the straw tube will be transmitted to the ASD-8 chip via $5m$ long thin coax cables ($0,9mm$ diameter, 75Ω). In order to avoid noise problems due to the signal loss in the long cable between straw chamber and ASD-8 chip, the analog signal of some mV is amplified by means of a very small preamplifier developed in research center Jülich. The preamplifiers match to the 75Ω coax cables. They are directly connected to the straw tubes in vacuum. With $< 40mW$ power dissipation, the preamps have no cooling problem even in vacuum. Fig.4.3 shows the wiring diagram of the preamplifier. The capacitor C3 decouples the high voltage and is also responsible for the differentiation of the straw signal in order to cancel the ion tail. The resistors $R1$ and $R2$ define the amount of fed back and in turn the value of total amplification. The time constants of the preamplifier are $< 10nsec$ rise time and $\approx 150nsec$ decay time.

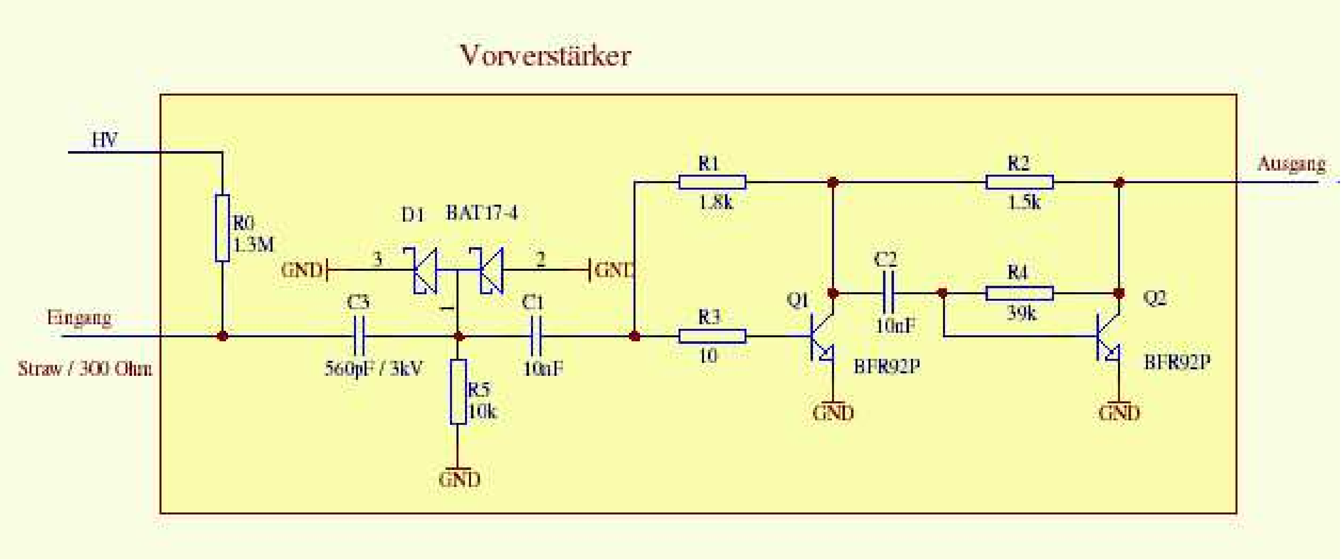

Figure 4.3: Wiring diagram of the preamplifier

Fig.4.4 shows the analog signal of a cosmic particle after the preamplifier. In the event shown two clusters of electrons are resolved in analog and digitization electronics.

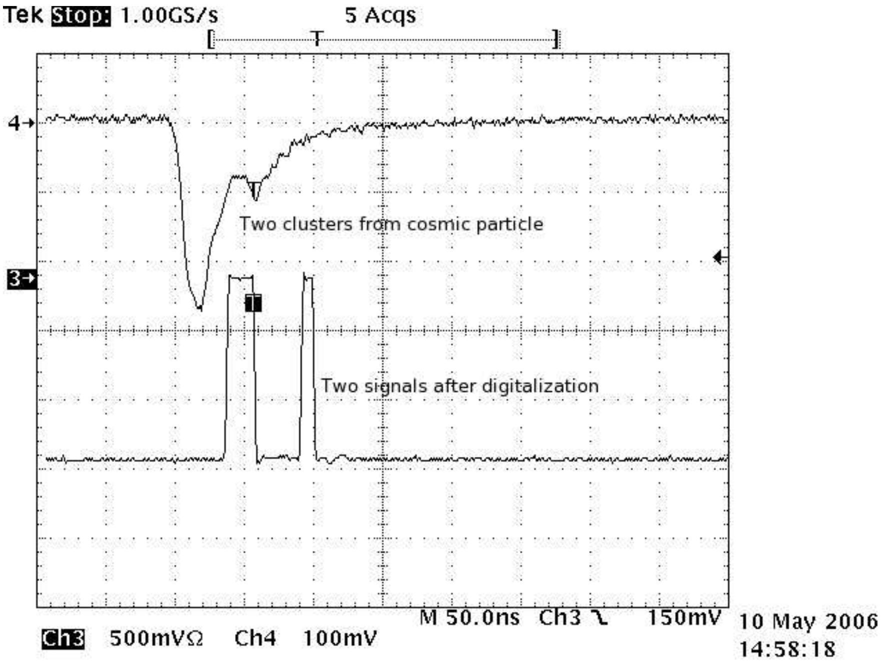

Figure 4.4: Analog signal (from the cosmic particle) after preamplifier and digitized form it behind the ECL converter. Two electron clusters appear in the event shown.

The most important properties of the preamplifier are:

- high band width ([83] Fig.4.5)
- low noise $< 10mV$ (Fig.4.4)
- low mass $\approx 0.37gr$
- adjustable amplification with dc supply

The preamplifier boards (width: $0.57cm$, height: $0.1cm$, length: $3.5cm$) are much smaller than the $1cm$ diameter straw tubes. They are mounted within the $1.98cm$ height of the double planes inside of the Rohacell frames which thus can be stapled.

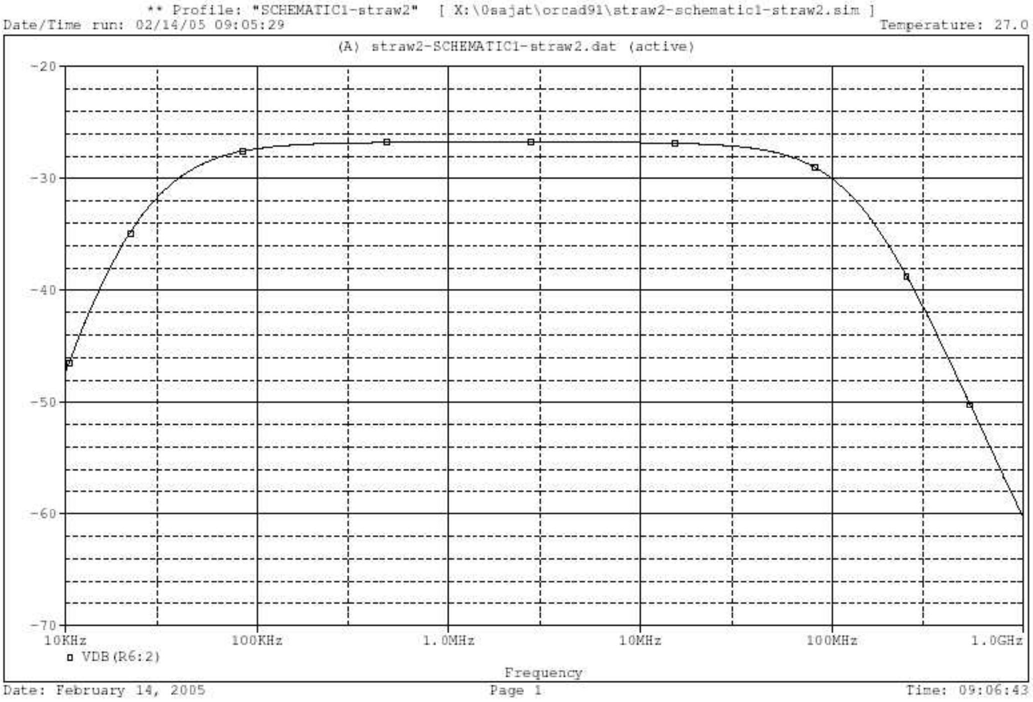

Figure 4.5: Simulated frequency response of the preamplifier [83]. Input signal -40 dB.

4.3 ASD-8 Input Board

Since the signal amplitude from the preamplifier at the end of the 5m cable is too big for the ASD-8 chip, it is reduced and shaped using an input board in front of the ASD-8. The wiring diagram is shown in Fig.4.6. Resistors R7 and R8 provide a reduction of the signal amplitude and impedance matching for the driving cable. C5 is used to set the signal level low enough in the ASD-8 and to block the direct current from the transmission line.

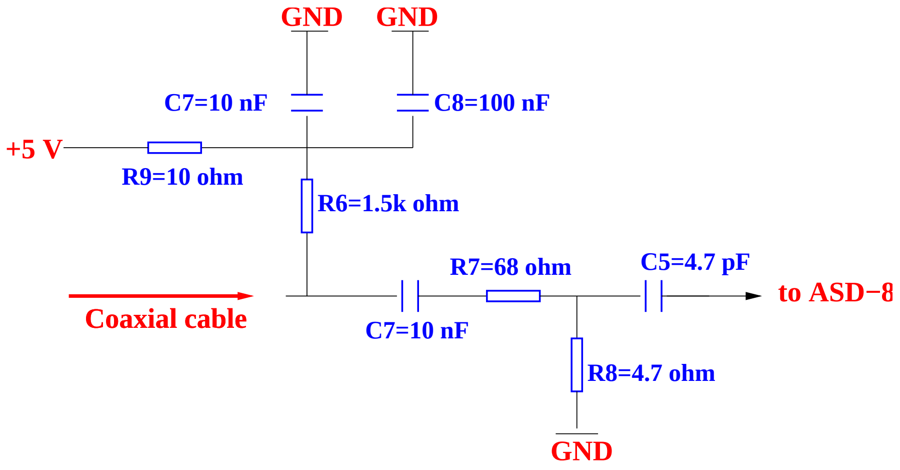

Figure 4.6: Schematic of the ASD-8 input board

The values of C5, R7 and R8 influence, besides the form of analog signal, efficiency of the detector, the internal stability and function of the ASD-8 chip (see section 4.6).

4.4 ASD-8 Chip

The amplifier-shaper-discriminator chip ASD-8 has been developed by the University of Pennsylvania for drift chamber applications. Requirements which ASD-8 chip satisfies are short measurement time ($\approx 10nsec$), good double pulse resolution ($\approx 25nsec$), low power consumption ($\approx 0.3W/chip$) and low operational threshold ($\approx 2fC$) [84]. The ASD-8 input is a preamplifier with a sensitivity of $2,5mV/fC$, a bandwidth of $100MHz$ and input impedance of 115Ω. The input is differential and symmetric for positive and negative pulses. The two-stage shaper eliminates the preamplifier tail utilizing pole zero cancellation technique. The shaped signal is then coupled into a two stage timing discriminator. The ASD-8 threshold is voltage programmable [85].

4.5 ECL Converter

Since the existing data acquisition system operates with the ECL norm signal (width of $10-20ns$ and amplitude of $750mV$), an ECL converter chip transforming ASD-8 signals to ECL norm signals, is designed and constructed for the Straw tracker in central electronic lab. of the research center Jülich [86].

4.6 Optimization of the ASD-8 Input Board

The electronic chain was oscillating. We observed that the oscillation is coupled back to the analog part of the electronic (ASD-8 input board) due to the feed back from preamplifier in the ASD-8 chip. As a first attempt to get rid of the oscillations, the grounding of the front end electronics was improved without success. Then we modified the ASD-8 input board which plays very important role on the stability of the ASD-8 chip, and the efficiency of the detector system. In the old board configuration shown in the Fig.4.7, a $1pF$ capacitor and two resistors of $R_1 = 56\Omega$ and $R_2 = 18\Omega$ were used.

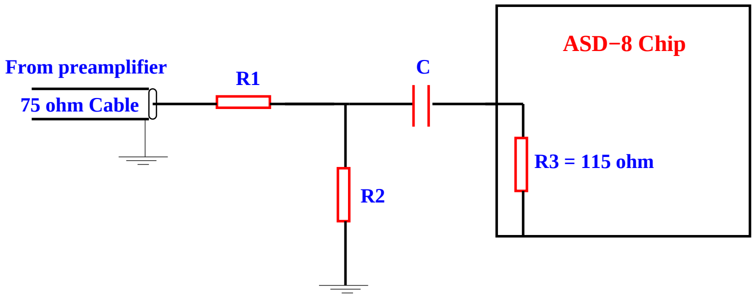

Figure 4.7: The schematic of the ASD-8 input board. R1 and R2 are selected such that 75 ohm impedance matching is fulfilled

Four different board configurations shown in the Table 4.1 were tested. Except for the $1pF$ configuration, with all of these three configurations, we obtained positive results. The whole system was oscillation free and stable. In order to select the best solution or to see the differences among them, the relationship between ASD-8 threshold and minimum signal amplitude exceeding this threshold was measured.

$R1(\Omega)$	$R2(\Omega)$	$C(pF)$	
56	18	1	oscillation
68	4.7	4.7	no oscillation, best efficiency
68	4.7	6.8	no oscillation, less efficiency
75	1.8	10	no oscillation, less efficiency

Table 4.1: Four configurations for the input board.

We used a pulser to simulate the straw signal. The simulated signal is connected directly to the preamplifier. As the threshold increases, we increased the amplitude of the straw signal until it exceeds this threshold and using an oscilloscope we recorded both values. As seen in the Fig.4.8 the best solution is the configuration with the capacitor of $4.7pF$. It enables the detection of the *smaller signals* and *more stable* state for the whole system.

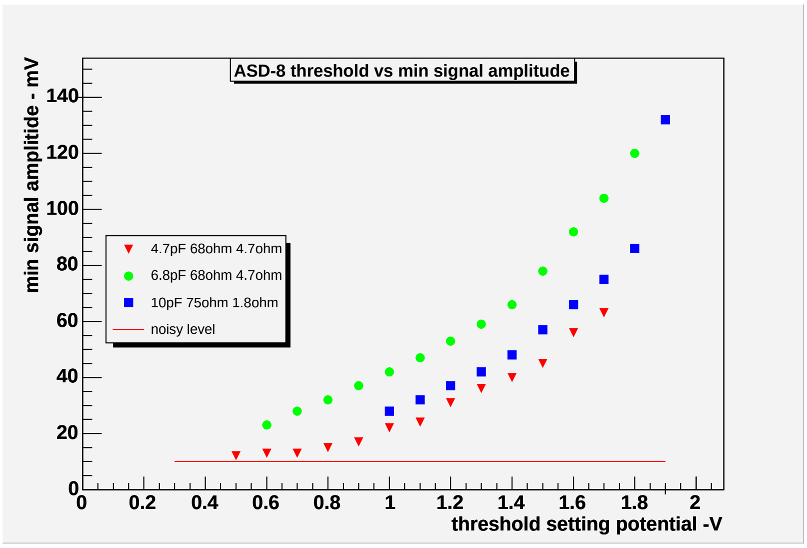

Figure 4.8: The ASD-8 threshold vs minimum signal amplitude

In order to see how these configurations affect the signal transmission, a simulation of the input board for $1\,pF$ and $4.7\,pF$ configuration is made [14] (observation behind the capacitor C at the ASD-8 input board is not possible). A triangle signal with the amplitude of $150mV$ and rising time of $2nsec$ is used as an input in the simulation.

As seen in Fig.4.9, the configuration with $1pf$ capacitor (right picture) changes the signal form very much due to the strong differentiation, producing a bipolar signal. This leads to efficiency problem in ASD-8, since the discriminator needs some certain amount of energy to work. With the bipolar signal the amount of charge in turn the energy delivered to the ASD-8 is less. Unlike the $1pF$ capacitor configuration, the other configurations do not change the form of the signal much as seen in left picture in Fig.4.9, the polarity of the potential changes very close to the end of the original signal. In the $1pF$ configuration it changes nearly in the middle of the input signal which means that just the typical lower frequencies in the straw signals are suppressed.

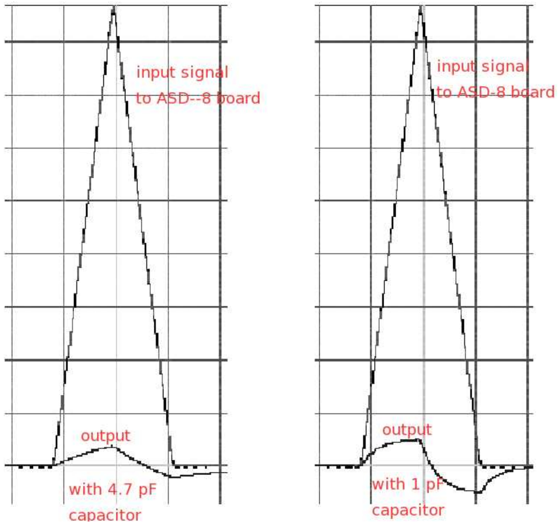

Figure 4.9: Left picture is the simulation of the input board with $4.7pF$ capacitor. The signal shape of the straw output remains nearly unchanged. Right is the simulation of the input board with $1pF$ capacitor. Triangle signal is given to the board as an input signal.

Chapter 5

Tests and Measurements with Straw Tubes

5.1 Introduction

To control production and performance of the straws, series of measurements and tests have been done. Some of them (high rate performance of the straws with beam, aging effect, first three dimensional tracking with cosmic rays etc.) were performed by using the straw prototype detector *"Cosmic Ray Test Facility"*. It is the first realistic application of the Jülich straws (see chapter 7).

5.2 Wire Tension Measurement

The wires in the straw tubes have to be held under proper mechanical tension. Too low tension leads to deviation of the wires from the ideal position caused by gravitational and electrostatic forces. Deviation in the position in turn results in changes in spatial resolution and reduction in high voltage stability. On the other hand, too strong tension can pull the wires out of the crimp pins or break the wires.

The wires in the tubes are stretched by using a weight of $40g$ and overpressure of $1.25bar$ (2.25 bar absolute) inside the straw tubes [87]. After the construction, tensions of the all straws are measured to check the quality of the production. The wire tension T is derived from the resonance frequency f of the mechanical wire oscillation via the relationship:

$$T = 4f^2L^2\rho_L$$

where L being length of the wire and ρ_L the wire mass per unit length [88]. The oscillations are excited with low-frequency AC current which is driven through the wire in the presence of a magnetic field. The resonance frequency can be found by inspection of phase relation between the current and voltage driving the wire oscillation. The details of the measurements are explained in [87]. The histogram in Fig.5.1 shows the result of the measurements for 448 straw tubes. The RMS of the wire tensions is $\approx 0.6g$ showing the high quality of production.

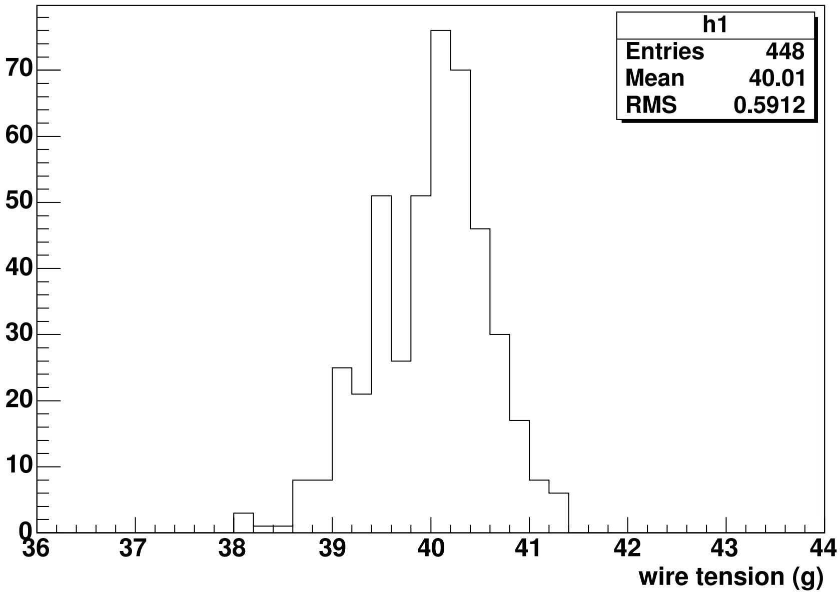

Figure 5.1: measured wire tension/g of 448 straws

5.3 Test of Gas Leakage from the Straws

COSY-TOF is a huge ($\approx 30m^3$) vacuum tank at some $10^{-3}mbar$. It is very important for the functioning (especially for the cryo target) that the vacuum state of the tank stays the same after the installation of the full straw tracker inside it.

The gas leakage from the straw tubes in vacuum is measured by Dr. Wintz by using following method: 24 straw tubes filled with 100% at a time CO_2 and Ar up to a $1.2bar$ are placed in a vacuum container (having the volume of $\approx 11.5l$ and the pressure of $\approx 10^{-3}$). When vacuum pump is switched off, the gas leakage of the straws leads to a pressure rise. By measuring pressure rise in the vacuum container, it was obtained that the leak rate Q_L of 24 straw tubes in the vacuum container is $3.3 * 10^{-3} mbar\ l/sec$ [89]. Using this information, one can calculate the end pressure of the TOF with 3000 straw tubes by using basic equation of the flow [90]:

$$V(dP/dt) = Q_L - SP$$

where S is pumping speed (Roots pump with $S \approx 70l/s$ in the TOF tank), Q_L is gas leakage, V total volume and P pressure of the vacuum tank.
At steady state ($dP/dt = 0$), the end pressure of the vacuum tank due to the gas leakage from 3000 straw tubes will be:

$$P_{end} = \frac{Q_L}{S} \approx 6.10^{-3}\ mbar$$

This amount of leakage through diffusion produces no danger for the vacuum state of the TOF.

5.4 Plateau Measurements

We measured the high voltage dependency of the count rate and signal amplitude by using a Fe^{55} source radiating photons with a energy of $5.9keV$. The Fe^{55} source is fixed few mm over the straw tube. With the help of a scalar the rate of the absorbed photons from Fe^{55} source and with an oscilloscope (Tektronix TDS 754D) the signal amplitudes and their dependencies on the high voltage are measured.

Fig.5.2 shows the relationship between count rate and high voltage for three different gas pressures. We can divide each curve into three regions. In the first region, the count rate increases linearly with increasing high voltage. In this part electric field may be insufficient to separate the ion pair from each other and the two particles may recombine to reform the gas atom. In the second region which is called plateau, the count rate is constant. All primary ionization processes are converted into registered signals. The gas amplification is rising along the plateau (Fig.5.3). After the plateau, the count rate increases sharply with increasing high voltage. This is due to the on set of steady gas discharging.

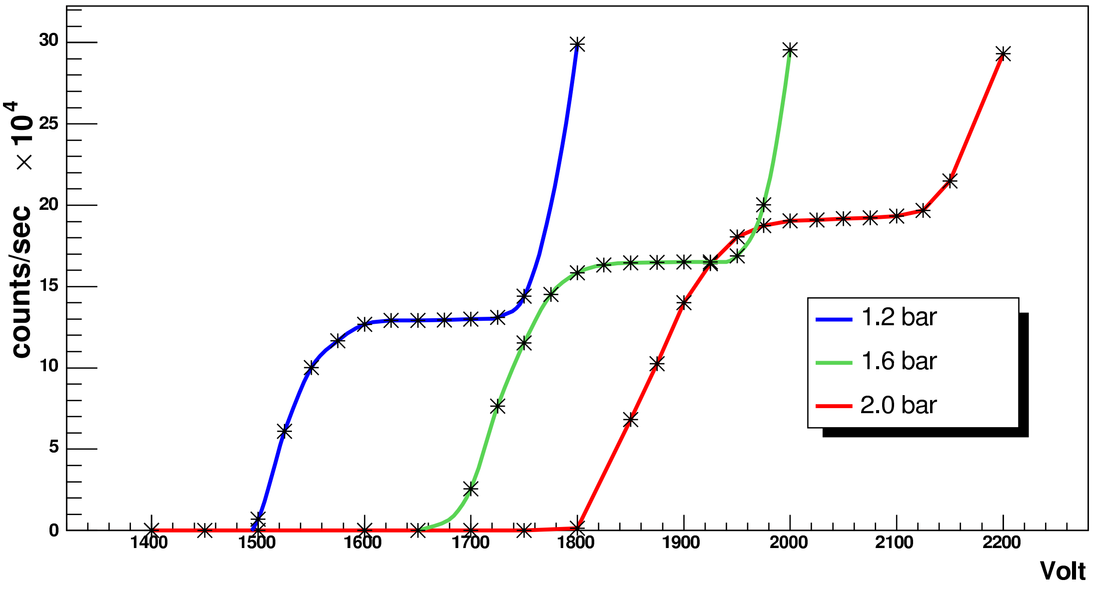

Figure 5.2: The relationship between HV and count rate with a $5.9keV$ γ source (Fe^{55}) for three different pressures

The straws work in the region of the plateau with a length of $150V$. Setting the high voltage to the end of the plateau gives the highest possible gas gain (signal amplitude vs high voltage, shown in Fig.5.3) improving the efficiency and resolution, but at the same time this leads to increase in dead time of the counter, since more electrons and ions are produced in the gas amplification process. The higher space charge needs more time to be collected.

Low dead time can be achieved when running at small amplification. This however needs good low noise preamplifiers.

Fig.5.2 shows that, the plateau shifts to higher voltage, and count rate increases with increasing pressure. The higher pressure means higher resistivity to the charge movement. As a result more electric field is needed for the charge collection.

If a beam of photons of intensity I_0 is incident upon a gas with N absorber atoms per unit volume, each of effective cross section σ, then the intensity I that penetrates to the other side goes as $I = I_0 \, exp[(-N\sigma)x]$, where x is the thickness [91]. With increasing pressure (N increases), I decreases and as a result count rate $(I_0 - I)$ increases.

The relationship between high voltage and signal amplitude is measured for three different gas pressures. Signals are measured behind the preamplifier. As seen in Fig.5.3 the amount of collected charge and the high voltage are nearly linearly dependent to each other. Above a certain amplitude, the signal amplitude stays constant at $250mV$ due to the saturation of the preamplifier.

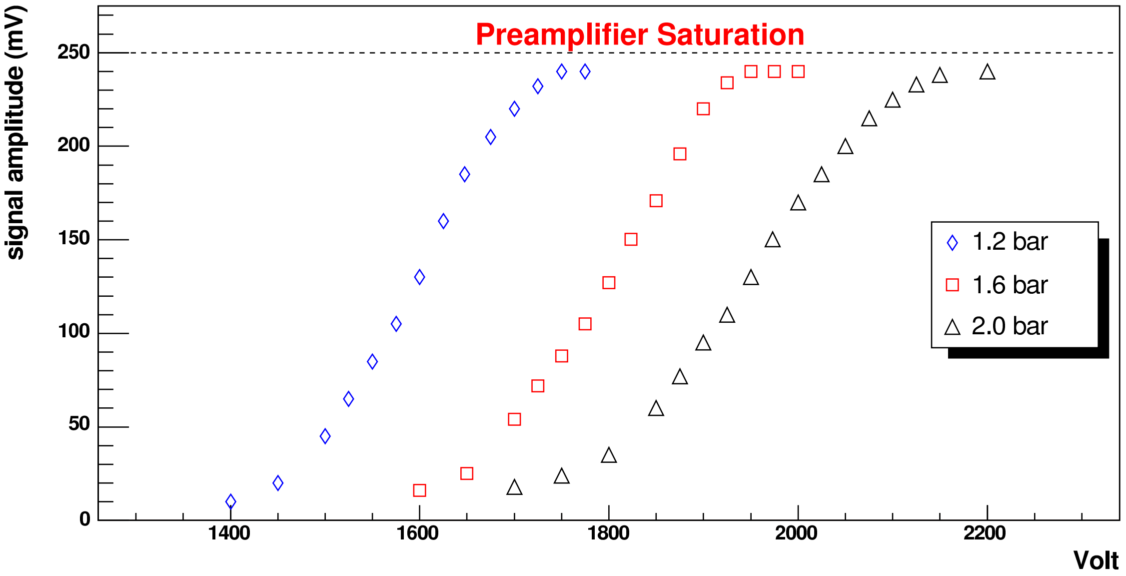

Figure 5.3: HV vs signal amplitude for three different absolute pressures of 1.2, 1.6, $2bar$.

5.5 Functionality Test with Beam

During the beam time in February-2003, one of the small hodoscope of the ”cosmic ray test facility” made from two perpendicular double planes (2×16 straws per each double plane) was exposed for 5 days to the direct deuteron beam with the momentum of $2.15GeV/c$ and the rate of $6 * 10^6 s^{-1} - 13 * 10^6 s^{-1}$.

Straw tubes in the hodoscope were filled with the gas mixture of $Ar/CO_2(82/18)$ to a pressure of $1.4bar$ absolute and operated with a high voltage of $1800V$.

The aim was to test the performance and possible aging effects of the straws with a very high rate beam leaving the TOF vacuum tank through a 100μ Mylar window and passing then through fiber hodoscopes with $4mm$ total scintillator thickness. The beam was spread out by divergence and straggling over a spot of about $5cm$ diameter on the straw plane. The experimental setup is shown in Fig.5.4. The straw planes were placed in air $10m$ far from the target position.

The straw signals were amplified and then transmitted to the electronics area via $25m$ long coaxial cables of 75Ω impedance and only $0.9mm$ diameter.

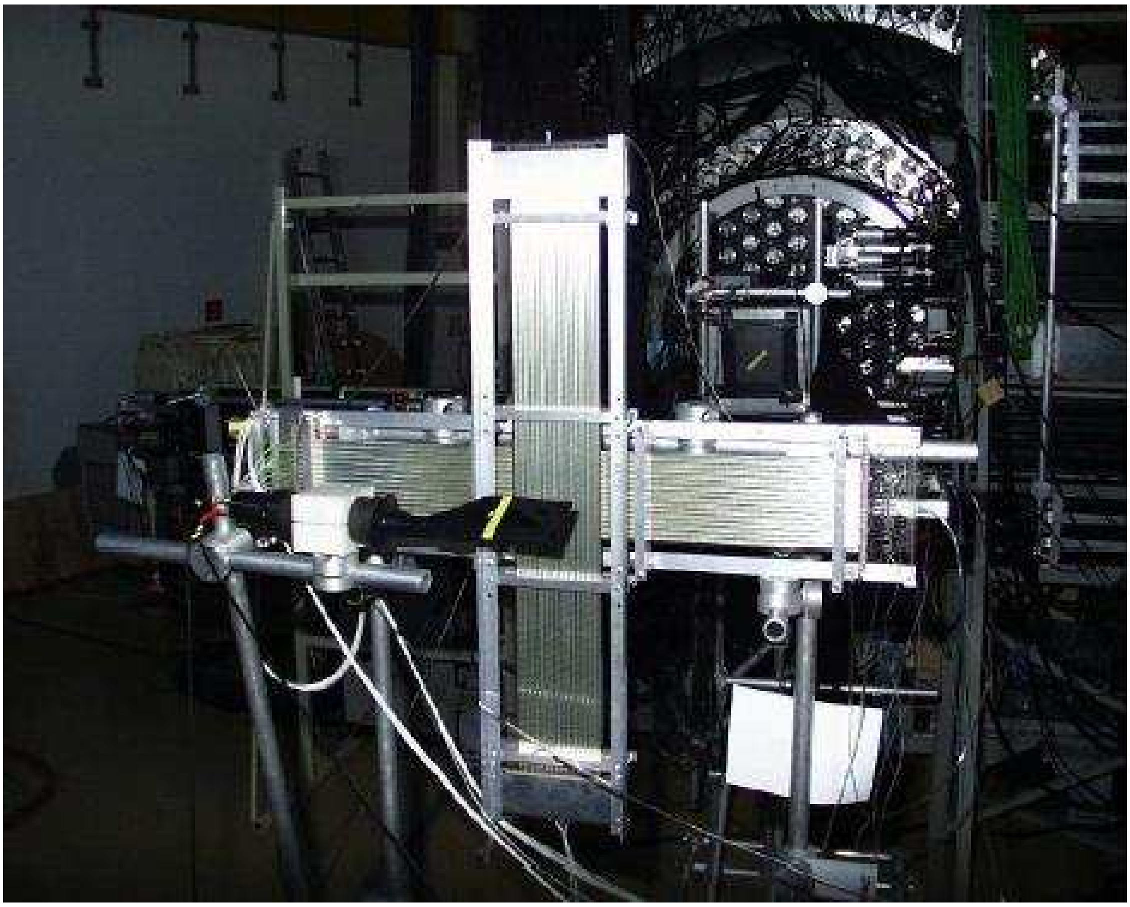

Figure 5.4: Two crossed straw frames placed behind the TOF for the performance test with the beam. Directly at the exit of the TOF tank one can see the quadratic frame of the $4mm$ thick fiber hodoscope which creates straggling.

During the 5 days we have not seen any high voltage break down or dark current. on the contrary very clean ionization current from the beam.

Fig.5.5 shows two analog- and one digital channels of the straws. In the oscilloscope picture, one sees 12 digital signals in $4\mu sec$ indicating the particle rate on the wire of $3 * 10^6$.

Fig.5.6 shows the beam profile measured for one straw plane.

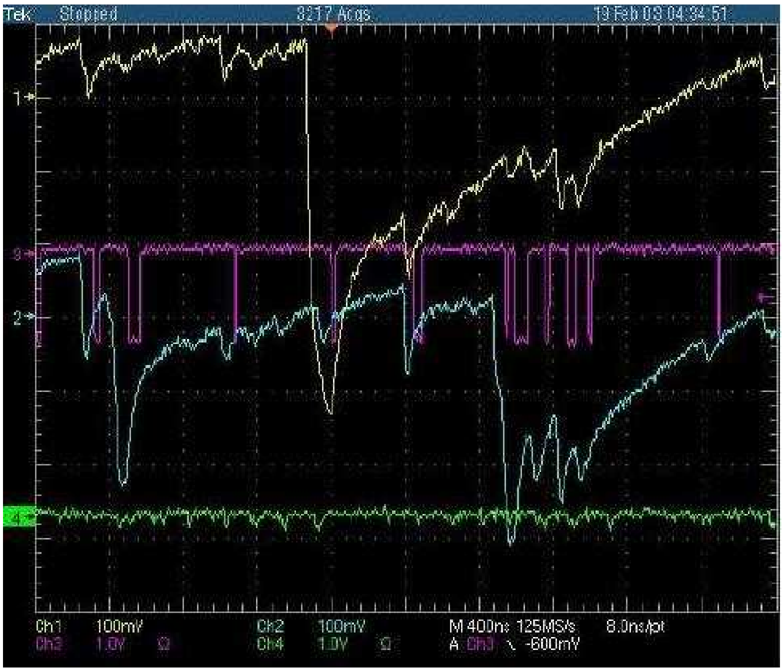

Figure 5.5: Yellow and blue: straw analog signals from the deuteron beam from COSY, pink: digital output derived from the blue signals. (Green is not used)

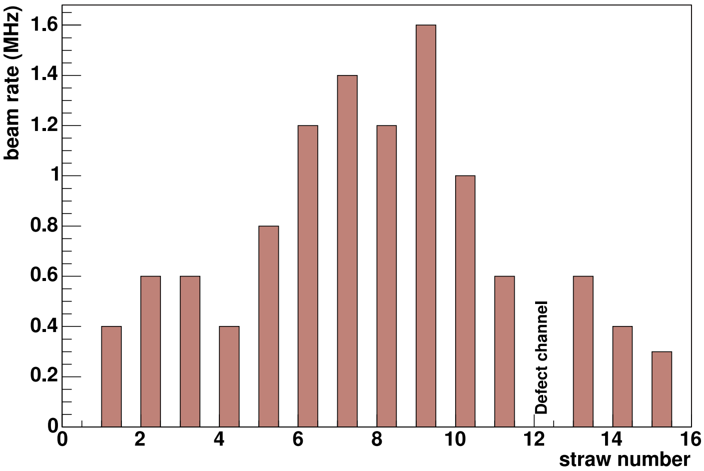

Figure 5.6: Beam profile measured with one plane with 15 straw tubes. Channel 12 was defect.

5.6 Aging Effects

The use of drift chambers in a strong radiation environment can lead to the loss of gain, reduction of plateau, excessive currents, self-sustained current discharge and sparking. All these problems are generally combined under the term "*aging*".

On the straws of the prototype exposed to the beam (beam time Feb. 2003) we found aging effects. Scanning with a Fe^{55} source along an irradiated straw tube a signal amplitude reduction (loss of gain) was found in the strongly illuminated regions. The same measurment on a straw which was not strongly illimunated gives flat response.

Fig.5.7 shows for two straw tubes maximum signal amplitude (averaged over 200 signals) versus distance. In the upper figure (illuminated straw), we see that, the signal amplitude decreases at two intervals ($25 - 32cm$ and $42 - 64cm$) to nearly 50%. These strong aging effects appeared after $\approx 10^{11}$ deuterons per cm wire length under counting conditions with high voltage of $1.8kV$. On the other hand, in the lower picture (unilluminated straw), we do not see any change in the signal amplitude. The small amplitude decrease along the counting wire towards the preamplifier position is due to the reflection of the signal (signal close to the preamplifier is wider but smaller).

Fig.5.8 shows the oscilloscope pictures of the reduced signals at the positions $\approx 50cm$ and normal signals at $\approx 45cm$ in the illuminated straw tube.

It has been commonly experienced that the aging effects are the result of a wire surface degradation of the anode wire and that this occurs frequently, but not always, in the form of an organic "*deposit*" that is a solid, but may also be liquid. During wire avalanches many molecules break up by collisions with electrons, de-excitation of atoms, and UV-photon absorption processes.

Especially for chamber gases which contain organic componenets like methane, isobuthan etc., the breaking of the chemical bonds in molecules and formation of free radicals requires only $3 - 4eV$ (very low compared with the ionization process requaring greater than $10eV$) and could lead to a large abundance of free radicals over the ions in the wire avalanches [92]. Since free radicals are chemically very active they will either recombine back to orginal molecules or other volatile species, or form new cross-linked molecular structures, which could react further to produce chain like polymers of increasing molecular weight, thus lowering the volatility of the resulting product. When the growing of polymerized chains becomes large enough for condensation to occur, it will diffuse to the electrode surface and deposit there.

For $ArCO_2$ mixtures aging effects should be less important. Although CO_2 is a stable quencher, the gradual decomposition of CO_2 in Ar/CO_2 mixtures also takes place and stable operation was found to be possible up to charges of $0.5 - 0.7C/(cm\ wire)$ [92]. With the beam rate of 10^{11} per cm wire length, a gas amplification of $3 * 10^5$ and 10^2 primary electrons per beam particle very roughly a charge of $\approx 0.5C/(cm\ wire)$ were collected during the beam time. The collected charge is comparable with the limiting total charge given in the literature. That explains the reduction of the gas gain in our straws.

It is also reported [92] that the wire chambers lifetime could be affected by the purity of the gas mixture, materials used in contact with the gas and superious contaminants.

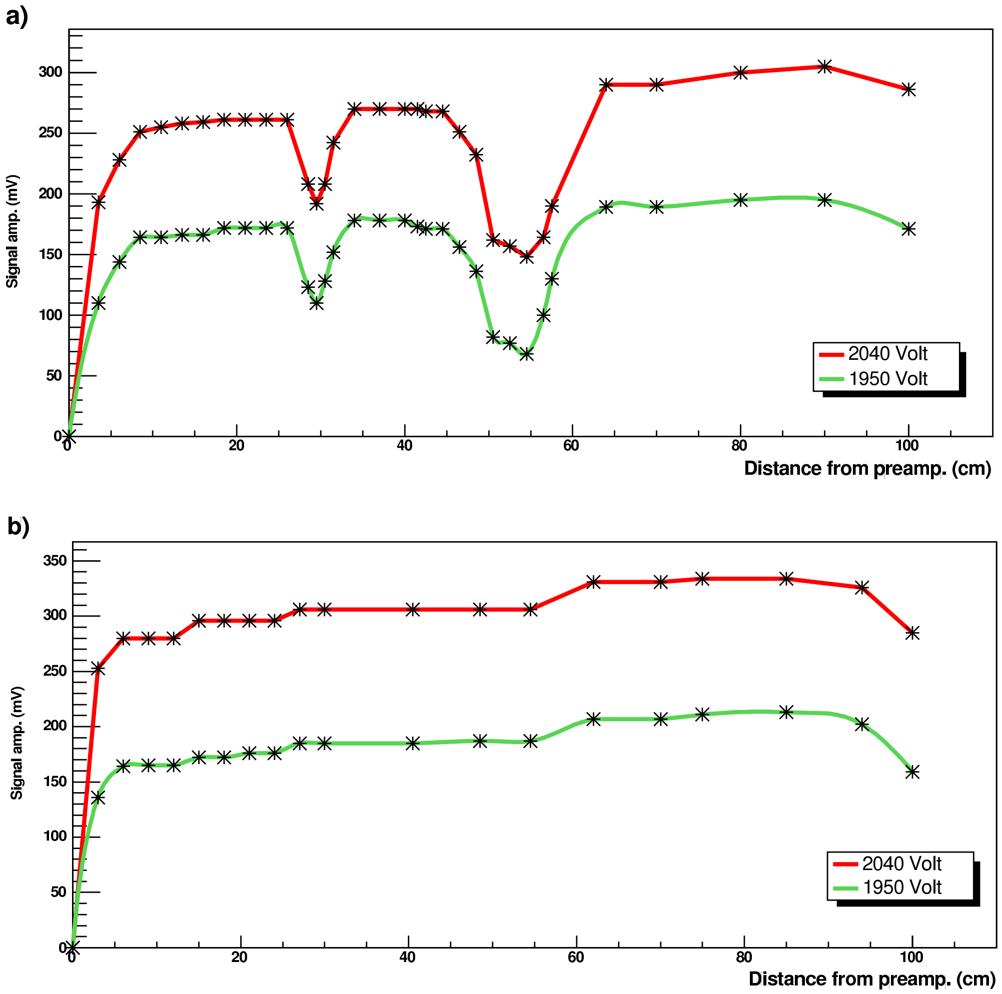

Figure 5.7: Signal amplitude from Fe^{55} source versus distance along the wire for two straw tubes at 2040 V and $1950V$. The plot a) corresponds to a straw irradiated locally with upto 10^{11} deuterons per cm counting wire. b) shows a straw which was not strongly irradiated. The zero point is the preamplifier side of the tube.

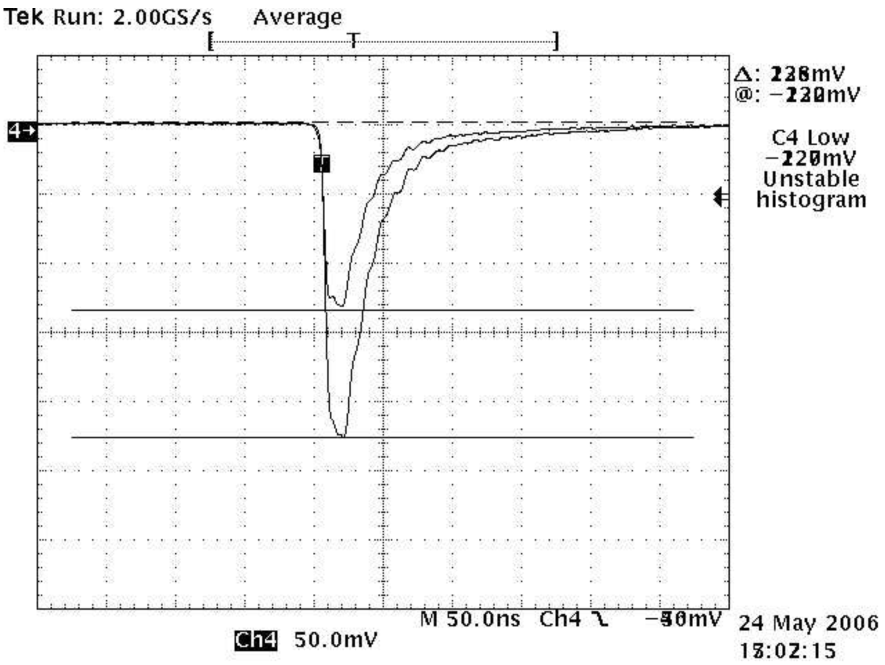

Figure 5.8: Averaged signals of the illuminated straw tube from Fig.5.7 at the distances of $\approx 50cm$ (small signal from degraded region) and $\approx 45cm$ (big signal from good counting region).

5.7 Visual Inspection of the aging Effects

The irradiated straw (Fig.5.7) was opened. In the irradiated region there are both clear traces on the aluminum surface and on the counting wire.

Fig.5.9 shows microscope picture of the irradiated region on the counting wire scaled up 50 times. The black isolated spots with a length of $20\mu m$ - $80\mu m$ shows the aging effect clearly.

Figure 5.9: Microscope picture of the irradiated region on the 20μ $\emptyset$ gold plated tungsten counting wire. Horizontal and vertical lengths of the picture are $0.77mm$ and $1.12mm$ respectively.

Fig.5.10 shows the wire region which was not irradiated. No black spots are seen.

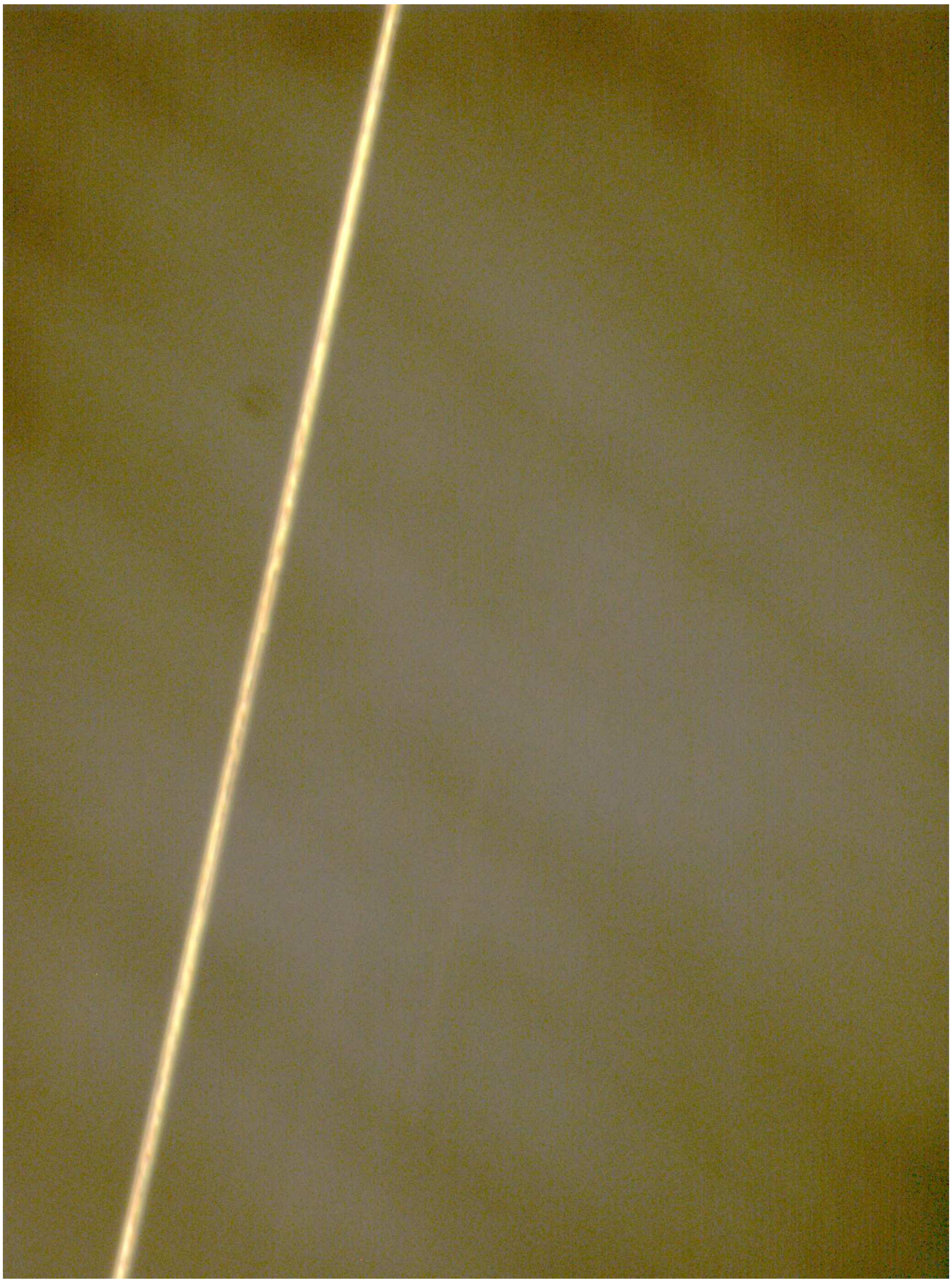

Figure 5.10: Microscope picture of the same wire as in Fig.5.9 in an unirradiated region. Horizontal and vertical lengths of the picture are $0.77mm$ and $1.12mm$ respectively.

Fig.5.11 shows the irradiated region of the aluminized Mylar cathode. Clear traces of aging effects are seen on the aluminum surface in the form of cloudy strips with a width of $50\mu m$ - $300\mu m$ and orthogonal to the counting wire direction.

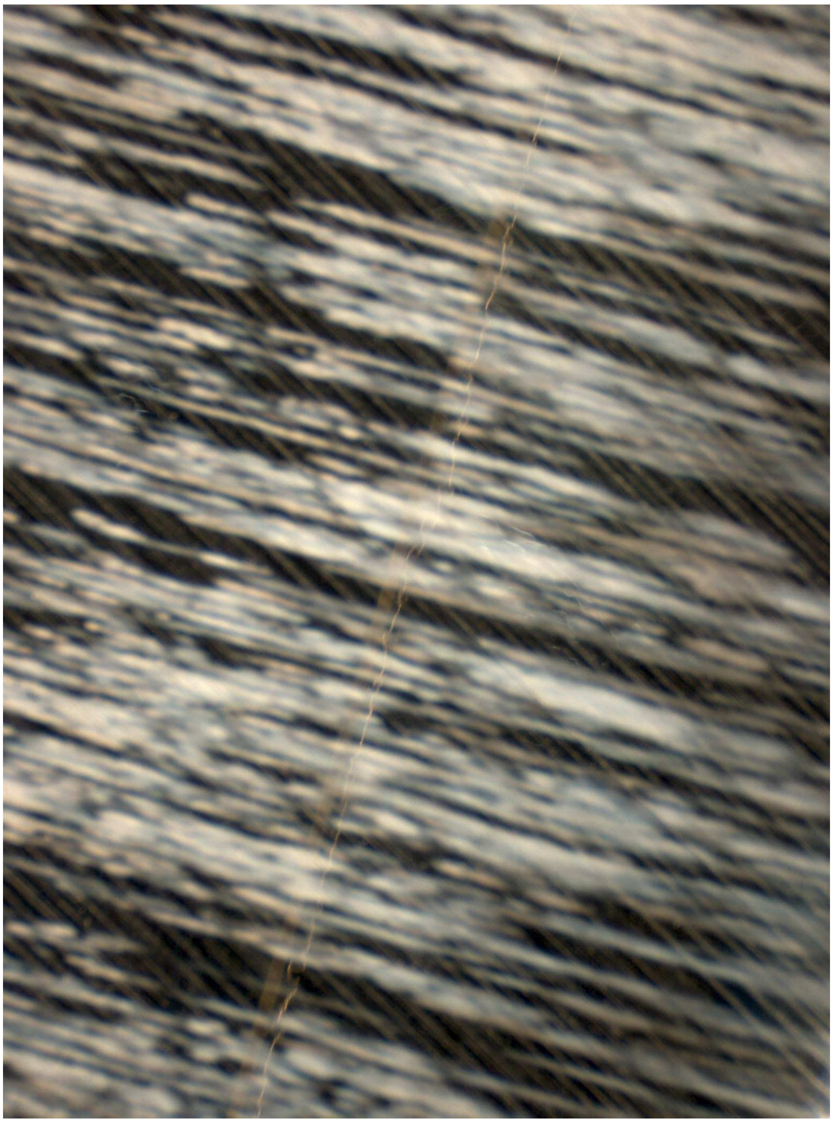

Figure 5.11: Irradiated region of the aluminized Mylar (magnification lower by a factor 8 with respect to Fig.5.9 and Fig.5.10). Clear traces of aging effect are seen on the aluminum surface as cloudy strips precisely orthogonal to the wire direction. The underlying pattern of inclined fine strips is a property of the aluminum mirror on the (undisturbed) Mylar surface. Horizontal and vertical lengths of the picture are $6.17mm$ and $8.95mm$ respectively.

Fig.5.12 is the same picture as in Fig.5.11 but scaled up 8 times.

Figure 5.12: Same irradiated region on the cathode as in Fig.5.11 scaled up 8 times (same magnification as in Fig.5.9 and Fig.5.10). The black regions are undisturbed, shiny aluminum mirror surface. The cloudy white strips are $50\mu m$ to $300\mu m$ wide and up to cm long. There the mirror surface is damaged. Horizontal and vertical lengths of the picture are $0.77mm$ and $1.12mm$ respectively.

Fig.5.13 shows the region of the aluminized Mylar which was not irradiated. We see no cloudy strips as in Fig.5.11

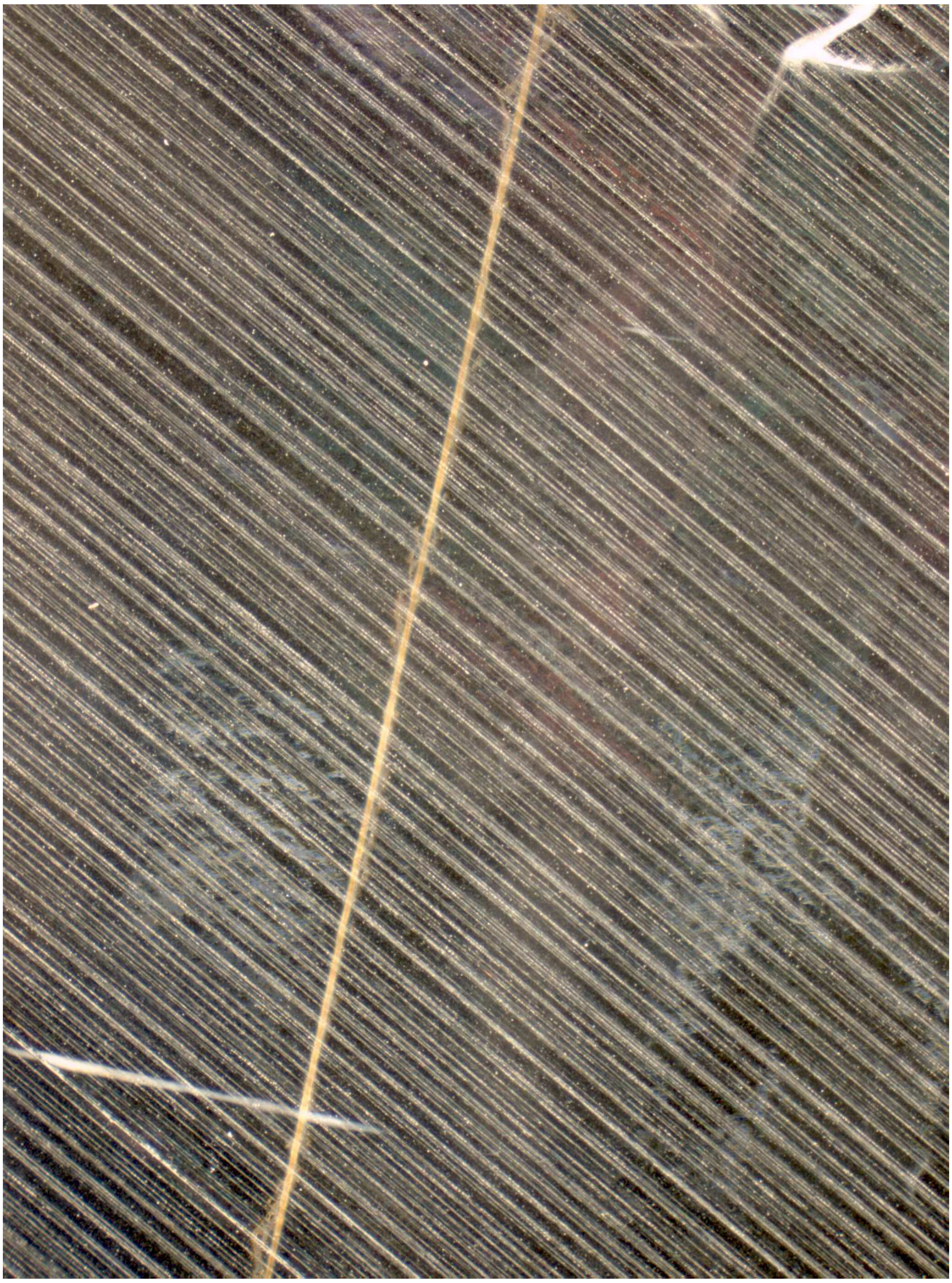

Figure 5.13: Region of the aluminized Mylar which was not irradiated. No cloudy strips are seen. The upward going line is the counting wire. This pattern can be directly compared to Fig.5.11 which has the same scale and orientation with respect to the counting wire. Horizontal and vertical lengths of the picture are 6.17*mm* and 8.95*mm* respectively.

From the visual inspection of the anode wire Fig.5.9, we see that radius of the wire has not increased so much to explain the reduction of the signal amplitude. The reason for that and for the strips on the Mylar is the whiskers which is very thin ($\approx 10nm$) hairlike carbon deposits on the wire. Due to the very high electric field around the whiskers the counting gas is ionized continously and space charge is produced around the wire. This is the produced space charge capturing the primary ions by recombination and leading to signal amplitude reduction. The strips on the Mylar is due to the oxidation of the aluminum by the oxygen atoms released from the decomposition of CO_2.

5.8 Spatial Resolution and Efficiency of the Straw Tube

Intrinsic resolution of the straw tube is influenced by two factors: diffusion of the electron cloud drifting to the anode wire and the statistical spread of the primary ionization clusters along the track. While clustering is dominating close to the anode wire, diffusion dominates at the region far from the anode wire.

The spatial resolution and efficiency of the single straw tubes are studied inside a vertical double-layer frame by means of cosmic ray tracks by Dr. Wintz [93]. The tracks are reconstructed after R(t)-Calibration (see 7.3.2) in two dimension by applying a linear fit of the track parameters (direction and foot points of the track) minimizing the normalized χ^2 (see 7.3.3).

Fig.5.14 shows the χ^2-distribution of the 1054 reconstructed tracks and isochrone residuals Δr_i of the 5645 straw hits. Symmetric residuals' distribution around a small mean of $4\mu m$ is indication of no systematic error. The deviation (σ) from the mean is about $85\mu m$

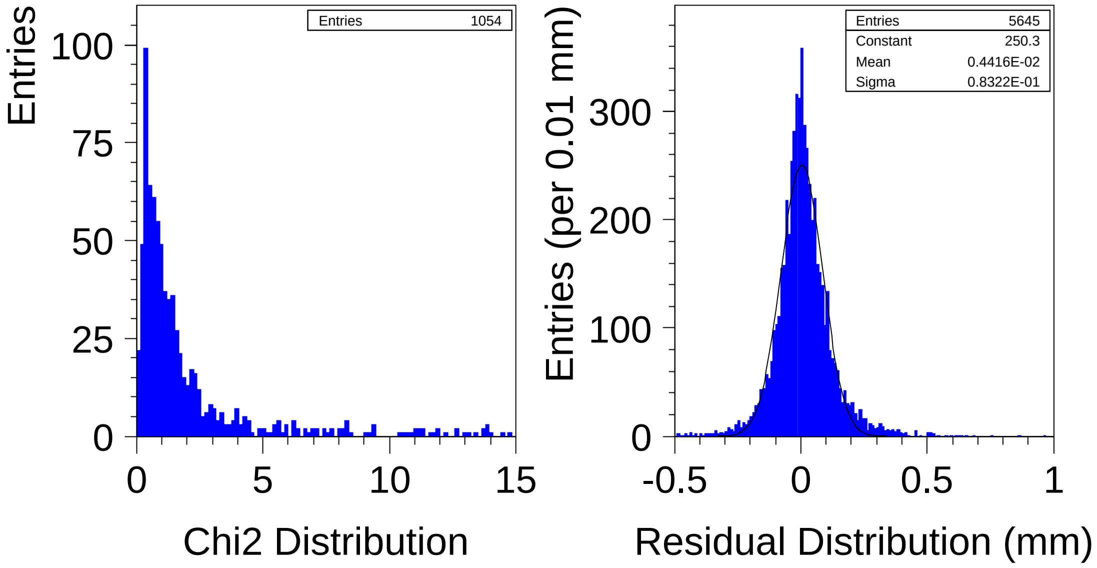

Figure 5.14: χ^2-distribution and isochrone residuals Δr_i of all reconstructed tracks. Mean and deviation (σ) of the residuals Gauss-fit are $4\mu m$ and $83\mu m$ respectively. Figure is taken from [93]

Fig.5.15 shows the radial dependence of the resolution obtained from reconstructed tracks. The resolution gets worse closer to the anode wire as expected due to the effect of the clustering. A good agreement between measured and simulated (for the simulation of the straws Garfield program package is used [94]) resolution is also seen.

In order to investigate the efficiency of the straw tube along the radius, 14 neighboring straws are used and minimum 5 straw hits are required for the track reconstruction. After reconstruction of the track, all isochrones are checked in this 14 straws. If no isochrone within

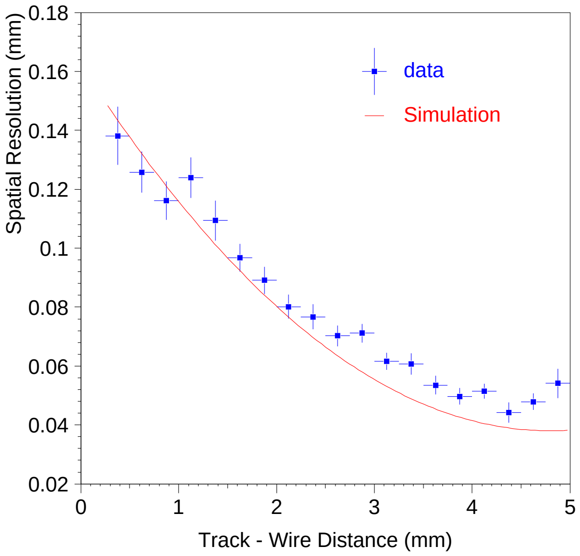

Figure 5.15: Spatial resolution of the straw tube.

a distance of 5σ to the track is found, this straw at this distance is counted as inefficient. A mean efficiency of 98.6% is found over the full straw radius of 5mm (Fig.5.16). Decrease in efficiency at a distance above 4.7mm is due to the decreasing track length in the counting gas consequently decreasing ionization. In this region the the number of ionization charges is too low to produce a signal exceeding the discriminator threshold.

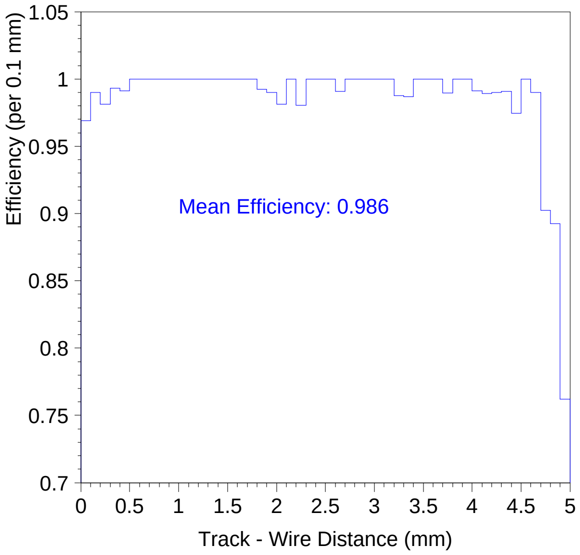

Figure 5.16: Efficiency vs tube radius

Chapter 6

Expected Improvements by the Straw Tracker

In order to illustrate the improvement with the straw tracker the experimental TOF data of the reaction $pp \rightarrow d\pi^+$ from the beam time Jan/2000 (using the existing fiber hodoscopes) and simulation data of the reaction $pp \rightarrow d\pi^+$ with the straw tracker are compared.

6.1 Selection of $pp \rightarrow \pi^+ d$ Events from the Beam Time Jan/2000

The data from the Jan/2000 beam time were analyzed by Dr. Wissermann. Results are presented in [95]. In order to obtain plots where experiment and straw tracker simulation data could be compared, some runs of Jan/2000 were analyzed in the frame of this thesis. Analysis routines of Dr. Wissermann were used. The calibration of the experimental data and data analysis software *TofRoot* is described in the appendix A and B

In two body reactions, the momenta of the outcoming particles can be calculated either from the time-of-flight or geometrically from the polar angles of the particles alone (in two particle reactions ejectiles and beam are co-planar).

The relative momentum resolution $\Delta p/p$ is given in terms of the time resolution Δt (ignoring the error in position) as [96]:

$$\frac{\Delta p}{p} = \gamma^2 \cdot \frac{\Delta t}{t}$$

Unfortunately, at β approaching one, it is not possible to calculate the particle momenta with reasonable resolution. However if one partner in the exit channel has high velocity (forward in center of mass (cm) frame) then the other (backward in cm) comes with particularly small velocity. Under such circumstances at least one momentum may be well measured.

A vector addition of the two outgoing directions to the beam momentum vector (conservation of momentum) allows to determine the absolute momenta for the two outgoing tracks (Fig.6.1) geometrically. In Fig.6.1 the hits in the detector plane are used together with the start point the target to determine the polar angles θ_1, θ_2 of two planar outgoing particles. The longitudinal and transversal component of the particles are given in terms of the scattering angles by:

$$|\vec{p}_T| = |\vec{p}_B| \cdot \frac{tan(\theta_1) \cdot tan(\theta_2)}{tan(\theta_1) + tan(\theta_2)} \tag{6.1}$$

$$|\vec{p}_{l1}| = |\vec{p}_B| \cdot \frac{tan(\theta_2)}{tan(\theta_1) + tan(\theta_2)} \tag{6.2}$$

$$|\vec{p}_{l2}| = |\vec{p}_B| \cdot \frac{tan(\theta_1)}{tan(\theta_1) + tan(\theta_2)} \tag{6.3}$$

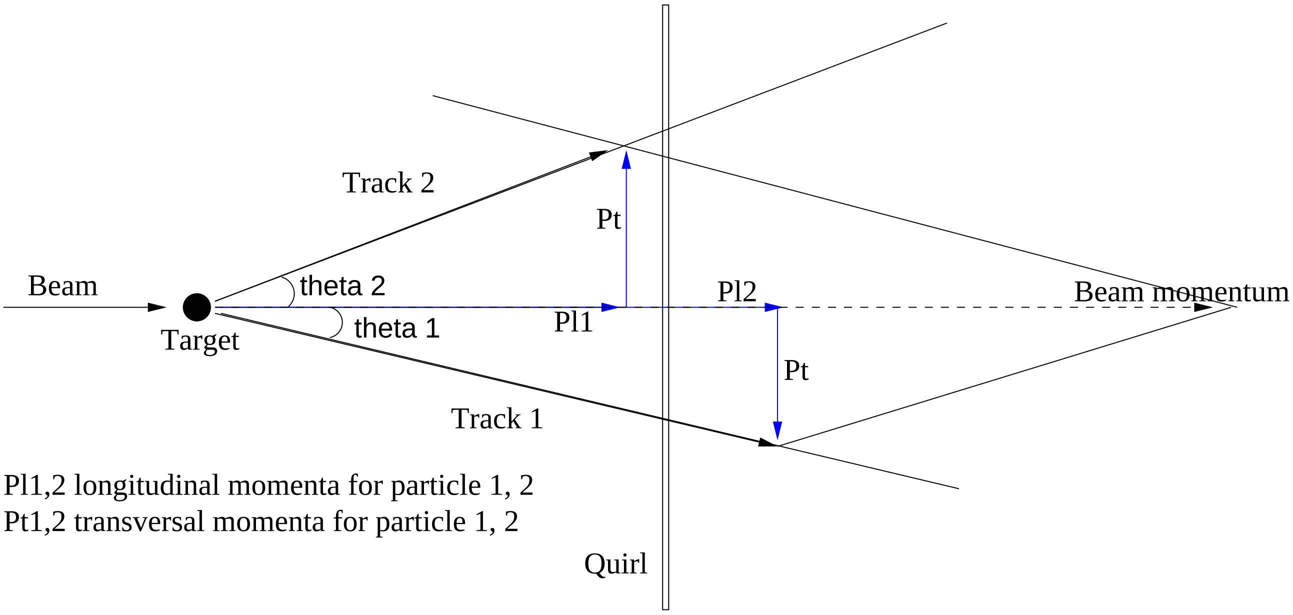

Figure 6.1: Geometrical impulse reconstruction from the vectorial sum of two outgoing directions to the beam momentum vector.

After obtaining the momenta of the outgoing particles by assuming two particles reaction, a χ^2 test is applied in order to distinguish (select) the events $pp \rightarrow d\pi^+$ from:

1. $pp \rightarrow pp$
2. $pp \rightarrow pp\gamma$
3. $pp \rightarrow pp\pi^0$
4. $pp \rightarrow pn\pi^+$

The test includes the angular and time-of-flight information from TOF. The coplanarity imposed by the two particle kinematics is the main geometrical selection criterion: due to the conservation of momentum, beam direction and the scattered two particles must lie in the same plane:

$$(\vec{p}_1 \times \vec{p}_2) \cdot \vec{p}_{beam} = 0$$

The time-of-flight information is also utilized advantageously: one can calculate the expected time-of-flight from the assigned four momenta and detector geometry. This is then compared to the actually measured time-of-flight:

$$\Delta TOF_{1,2} = (TOF_{1,2})_{meas} - (TOF_{1,2})_{calc}$$

Besides this information, the deviation from the expected missing mass Eq.6.4 and the difference between β values calculated from time-of-flight and dE/dx measurements in the Microstrip detector are also utilized in the χ^2 test. The result of the χ^2-test is shown in Fig.6.2, the first peak separates the $pp \rightarrow d\pi^+$ events from the rest.

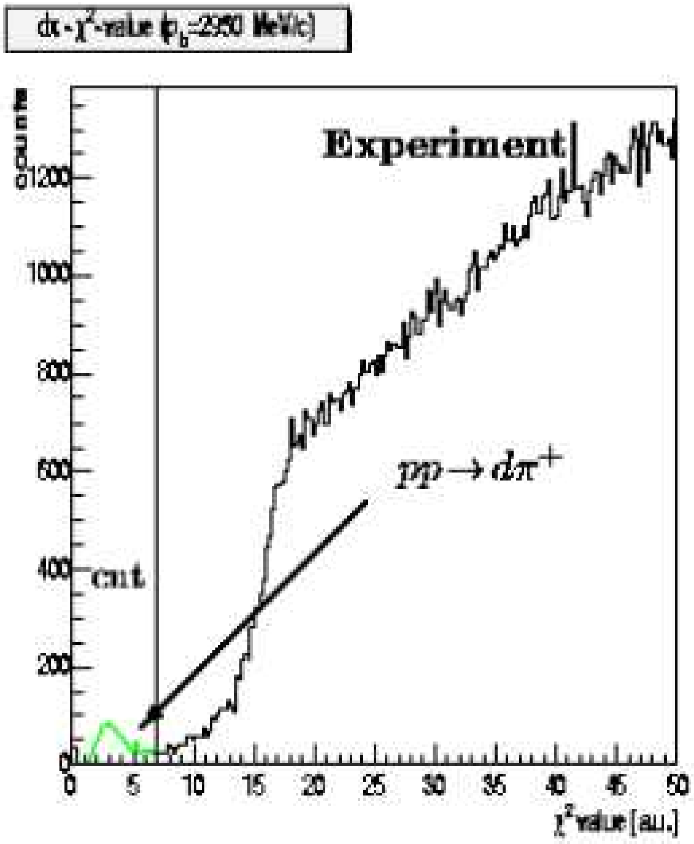

Figure 6.2: χ^2-value distribution for the reaction $pp \rightarrow d\pi^+$. The first peak corresponds to $pp \rightarrow d\pi^+$ events. Figure is taken from [95]

The world data on total cross sections together with Dr. Wissermann's results ($\sigma_{tot} = 46.6$ at $2950 MeV/c$ and $\sigma_{tot} = 31.5$ at $3200 MeV/c$) and differential cross sections from Dr. Wissermann's analysis (for beam momenta $2950 MeV/c$ and $3200 MeV/c$) are shown in the Fig.6.3 and Fig.6.4 respectively. These TOF data are in reasonable agreement with the literature. However the overall precision of the world data around $3 GeV/c$ beam momentum is still surprisingly limited.

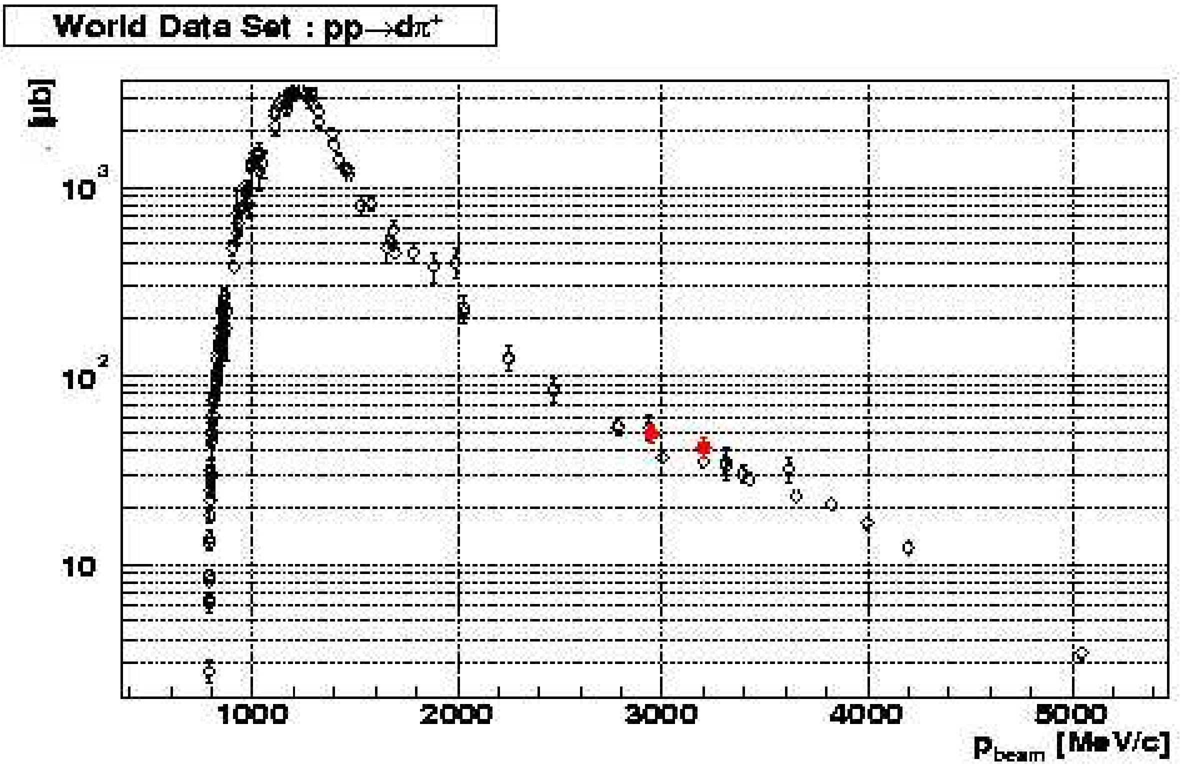

Figure 6.3: Collection of the world data on total cross section for the reaction $pp \to d\pi^+$. The red points are the result of the Dr. Wissermann's analysis ($\sigma_{tot} = 46.6$ at $2950 MeV/c$ and $\sigma_{tot} = 31.5$ at $3200 MeV/c$). Figure is taken from [95].

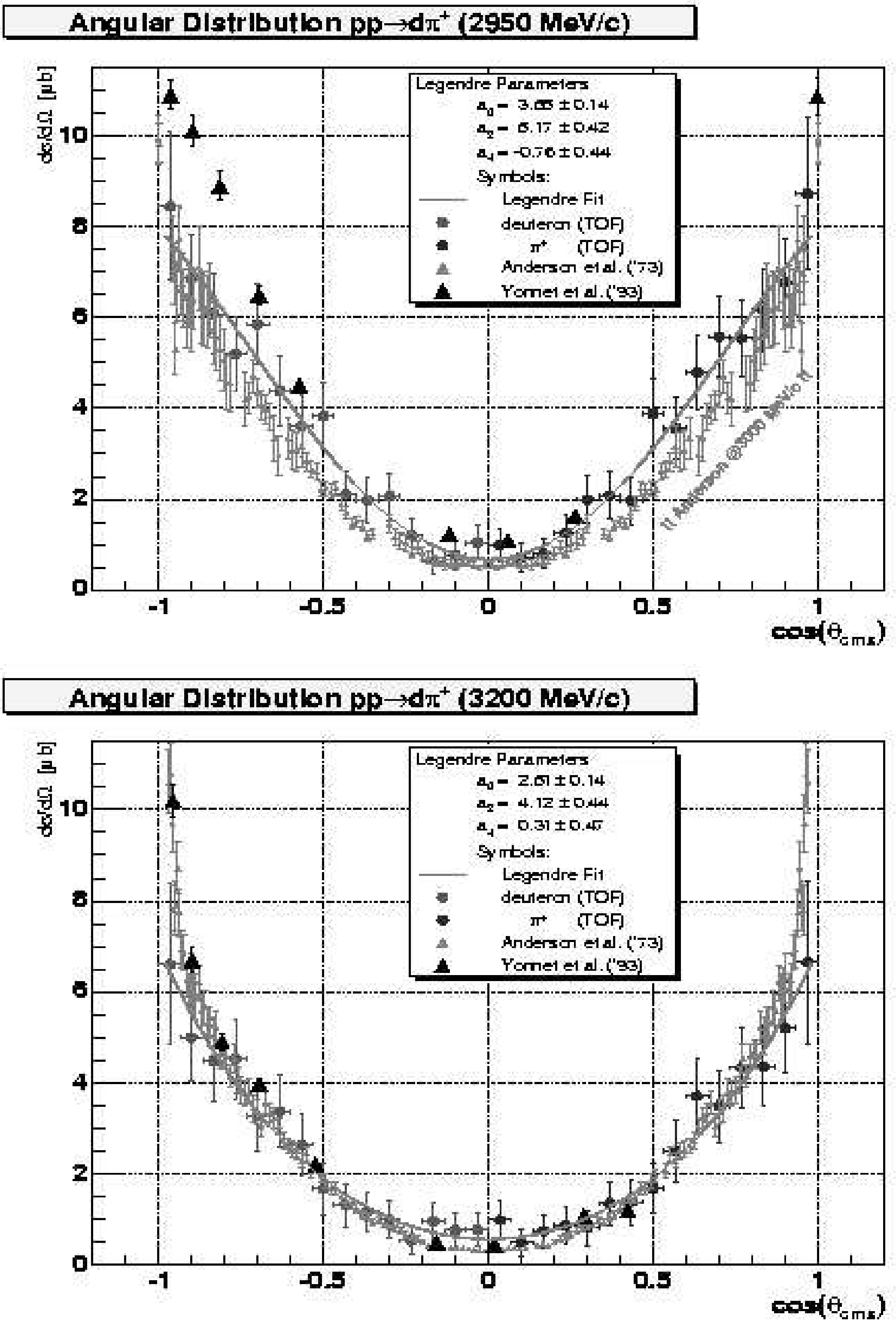

Figure 6.4: Angular distribution for $pp \to d\pi^+$. Figure is taken from [95].

6.2 Simulation of $pp \rightarrow d\pi^+$ events with the Straw Tracker

The simulation of the straw tracker (geometry and response of the straw tracker in COSY-TOF) was added to the existing Monte Carlo simulation program of COSY-TOF in order to demonstrate improvements with the tracker on the resolution in a simple reaction. The data analysis programs for the straw tracker (tracking and event reconstruction) had to be implemented.

The Juelich Monte Carlo simulation program is based on the GEANT-3 package [97] developed at CERN. GEANT is a toolkit for both full and fast Monte Carlo simulation of detectors in High Energy Physics. The principal applications of GEANT in High Energy Physics are:

- the transport of particles (tracking) through an experimental setup for the simulation of detector response;
- the graphical representation of the setup and of the particle trajectories.

In view of these applications, the GEANT system allows to:

- describe an experimental setup by a structure of geometrical volumes.
- accept events simulated by Monte Carlo generators.
- transport particles through the various regions of the setup, taking into account geometrical volume boundaries and physical effects according to the nature of the particles themselves, their interactions with matter, and the magnetic field.
- record particle trajectories and the response of the detector components.
- visualize the detectors and the particle trajectories.

During the tracking through the simulated experimental setup, the distance between track and each detector element is calculated. If the track passes through an element, at each tracking step the energy loss is calculated and a new momentum is assigned to the track. If this element is defined as a sensitive detector, the total energy loss in it is saved as an ADC value. At the end of tracking, one can get out from the energy loss whether an element is hit or not. GEANT delivers also the entrance and exit coordinates in a detector element which we used to simulate drift times in straw tubes. Using the entrance and exit points defining the track, one can calculate the minimum distance between anode wire and track from Eq.7.5. Using the resolution curve of the straw tube shown in Fig.5.15, one can vary the obtained distance to simulate the diffusion and clustering in the tube. As a last step, TDC values as a response of the straw tubes are calculated by using R(t) calibration function obtained from the measured TDC spectra of the straw tubes (see section 7.3.2). More information about the Juelich Monte Carlo simulation program can be found in [52].

6.3 COSY-TOF with and without Straw Tracker

From the $pp \to d\pi^+$ events selected out of the experimental data, the angular and missing mass resolution of TOF were determined. Using the GEANT3 software package the Straw tracker is simulated with the same experimental conditions as in the beam time of Jan/2000 in TOF as explained in section 6.2.

Fig.6.5 and Fig.6.6 show the longitudinal versus transversal momentum components of the d and π^+ calculated from Eq.6.1 - Eq.6.3 using polar angles θ_1 and θ_2 of the particle tracks from the real data of the beam time Jan/2000 (both geometry and time of flight informations were used at event reconstruction) without the straw tracker and simulation data with the straw tracker (only geometry information was used) respectively. The significant improvement in the momentum resolution is seen clearly from the both figures. It is due to the improvement of the tracking resolution.

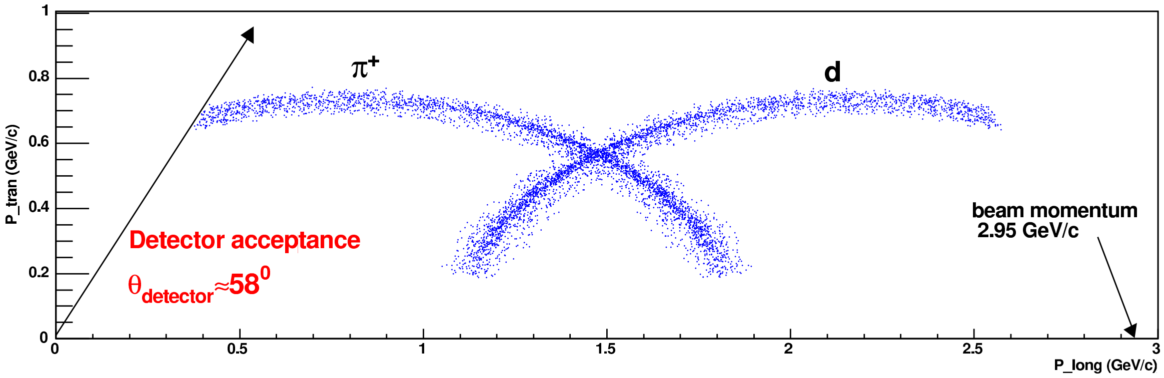

Figure 6.5: The longitudinal and transversal momentum components as obtained from the experimental data, using the actual TOF setup without straw tracker. Geometry and time of flight informations were used at the event reconstruction.

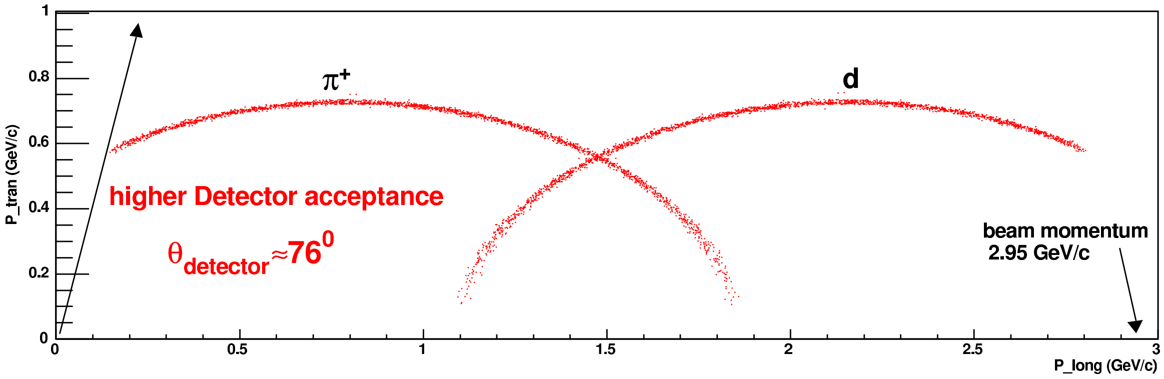

Figure 6.6: The longitudinal and transversal momentum components from the simulation data, with the straw tracker replacing the fiber hodoscopes. Only geometry information was used. Both resolution and acceptance are improved

The missing mass analysis in particle physics is a crucial tool for the identification of particles or events. Improvement in the missing mass resolution leads, besides the expressiveness, to reduction of the background reactions in the results. Due to the misinterpretation of the experimental data (since there is no perfect measurement), background reactions are always included in the results with a certain amount. The better the missing mass resolution is, the less background reactions are included in the results. This can be understood by inspection of Fig.6.7 and Fig.6.8. If we assume an uniformly distributed background (≈ 3 events per bin, estimated from the Fig.6.7) over the missing mass histogram, the amount of the background in the missing mass distribution of the experimental data is much higher than in the simulated distribution in Fig.6.8. The wider the missing mass peak, like in the experimental data, the more background events are included.

From the conservation of the total invariant mass (Eq.6.4), one can calculate the square of the missing mass for the reaction $pp \rightarrow d\pi^+$ in which four momenta of beam and target (P^b_{proton} and P^t_{proton}) are known.

$$(P^b_{proton} + P^t_{proton} - P_d - P_{\pi^+})^2 = P_X^2 = m_X^2 \tag{6.4}$$

where P_X is the four momentum of the unknown particle and must be a zero four vector if the reaction is $pp \rightarrow d\pi^+$. The square of missing mass spectra from real and Monte-Carlo data are shown in Fig.6.7 and Fig.6.8. We see that the resolution of the missing mass is also improved by a factor ≈ 10 with the improvement in the geometrical resolution.

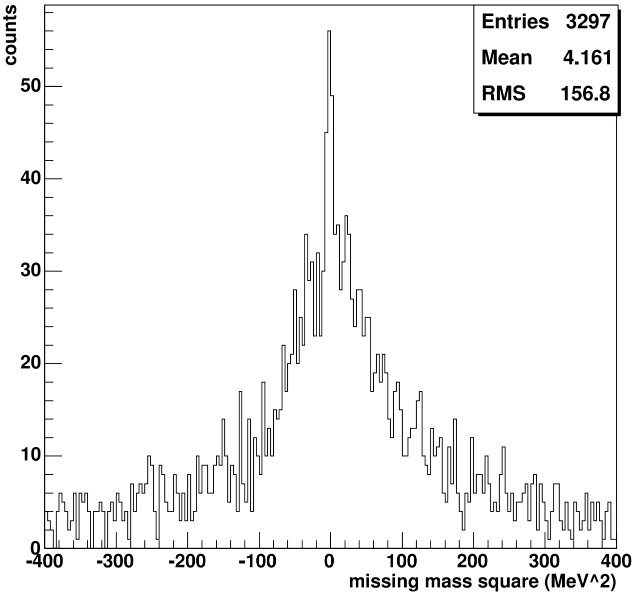

Figure 6.7: Missing mass spectra for the reaction $pp \rightarrow d\pi^+$ from experimental data of Jan/2000 (without straw tracker).

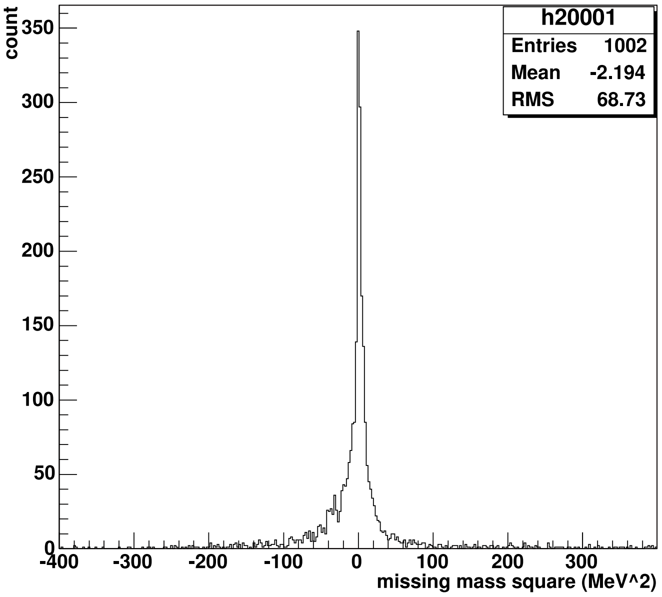

Figure 6.8: Missing mass spectra for the reaction $pp \rightarrow d\pi^+$ from simulation data with Straw tracker.

Chapter 7

Cosmic Ray Test Facility

Based on the developments for COSY-TOF straw tracker a small cosmic ray test facility was built (7.1). It allowed to do realistic tests, optimization and application of the tracker components. Measurements on scintillators and single straw tube were carried out with cosmic rays.

Primary cosmic rays are high energy charged particles, originating from outer space, which strike the Earth from all directions. Most cosmic rays are nuclei, ranging from the lightest to the heaviest elements in the periodic table. The high energy cosmic rays undergo collisions with atoms of the upper atmosphere, and produce a cascade of "secondary" particles that shower down through the atmosphere to the Earth's surface. Secondary cosmic rays include pions which mostly decay before they reach the surface and produce muons, neutrinos, and gamma rays, as well as electrons and positrons produced by muon decay and gamma ray interactions with atmospheric atoms. Most secondary cosmic rays reaching the Earth's surface are muons ($\approx 80\%$), with a mean energy of $4\,GeV$ and an average intensity of about $200/(m^2\,sec)$ [98].

The cosmic ray test facility 7.1 consists of 4 double planes of 128 straw tubes in total (16 straw tubes per plane), read out electronics, two scintillators for the trigger signal and the data acquisition system (DAQ). The planes are arranged two orthogonal hodoscopes sandwiched between the two trigger scintillators. It is possible to reconstruct tracks of the cosmic ray particles in three dimensions. Fig.7.2 shows the schematic side view of the cosmic ray test facility with distances.

The read out electronics (see 4) consists of preamplifiers directly connected to the straw anode wires, ASD-8, and an ECL converter. The signals from the preamplifiers are transmitted to the ASD-8 digitizing unit via $5\,m$ long cables having the impedance of 75Ω. After the digitalization and conversion into the ECL norm, the signals are delayed for $\approx 200\,nsec$ via electronic delay. Finally they are transmitted to the TDC module via twisted pair cables.

The delay became necessary since only old TDC modules were avaliable which worked with common start. First twisted pair cable delays were tried which however deteriorated the quality of the digital signal so much, that the TDC response even lost efficiency down to 85%. The electronic delays give full efficiency but still reduced time resolution.

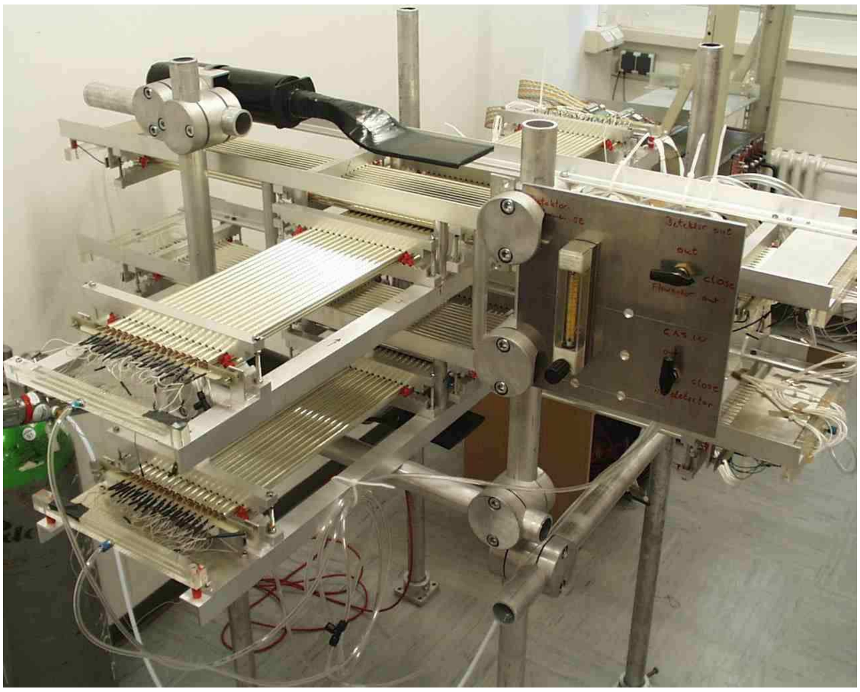

Figure 7.1: The cosmic ray test facility. Two orthogonal hodoscopes made from 90^o crossed straw tube double planes are sandwiched between the two plastic scintillators which provide a trigger coincidence.

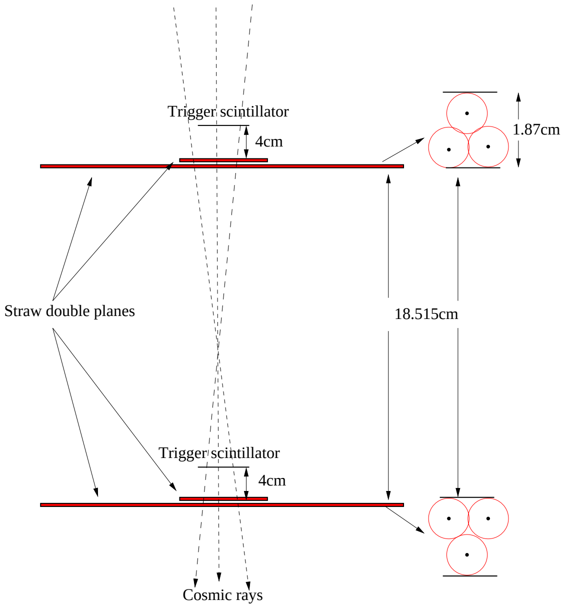

Figure 7.2: Schematic side view of the cosmic ray test facility with distances as it was used for the tests.

7.1 The Trigger

An external trigger is set up from a coincidence between two organic scintillators. Organic scintillators are used for timing and trigger since they are very fast due to the short decay time (few nanoseconds) of excited molecules in them. The scintillators have a size of $0.5 \times 10 \times 35\,cm^3$ and are connected to Philips XP-2212 photomultiplier tubes (PMT) at one end.

Their analog output signals are fed into discriminators. They are converted into digital signals with fixed width of $50nsec$, and then sent to a coincidence module. The *AND* output is the "*trigger signal*". The trigger starts the time measurement in the TDC modules and enables QDC, ADC channels, and transfer of the data to the storage. In Fig.7.3 the whole electronic chain is shown.

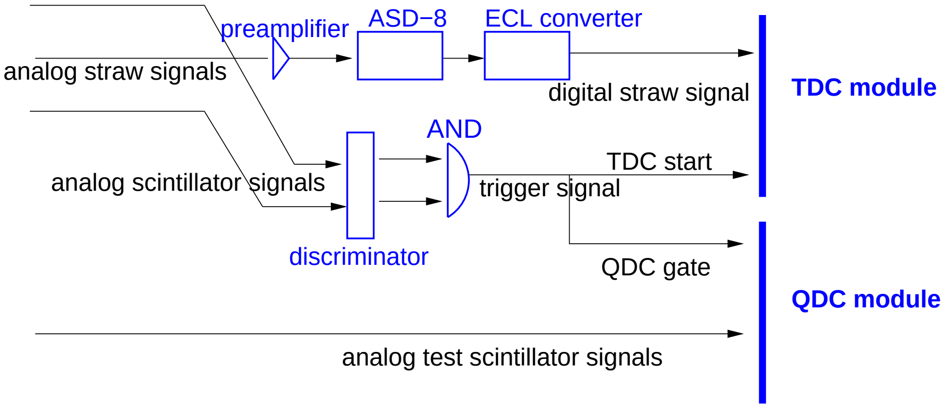

Figure 7.3: The electronic setup used in the measurements.

7.2 Data Acquisition System (DAQ)

A separate DAQ system was constructed for the test facility by Dr. Wüstner and Dr. Sefzick. Its architecture (COSY-TOF's DAQ system uses it too) is based on available standards (VME, FASTBUS, CAMAC, VICbus) and UNIX workstations (Fig.7.4). Based on this hardware a flexible and modular data acquisition software was designed allowing the configuration of various experiment arrangements. The software design for run control is arranged according to a client server connectivity model [99]. It provides services for starting, stopping, and downloading programs into a fronted device, reading its variables and handling the connections between nodes in a communication system. The protocol governing the communication between client and server is called "*Experiment Message Specification (EMS)*". It uses Ethernet and wide spread TCP/IP protocol as the transport system [100].

For the cosmic ray test facility, the VME hardware standard with a V1488 TDC module (Time to Digital Converter) and a V265 QDC module is used for the digitizing of the time and charge.

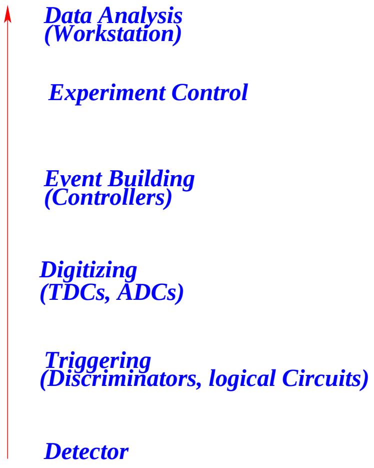

Figure 7.4: The DAQ Process.

7.3 Cosmic Ray Tracking

7.3.1 Measurement

Although the setup shown in Fig.7.1 consists of 128 straw tubes, we used only 64 straw channels (8 straws per plane) due to the shortage in the electronic delay units (CAEN C469 Gate and Delay Generator). The straws were at $2\,bar$ absolute pressure and $2040\,V$ high voltage during the measurements.

What we measure are the drift times of the electrons coming from the cosmic tracks. A trigger signal is starts the time counting in the TDC modules for the drift time measurement. The stop signals for the drift time measurement come from the individual single straw responses. The time difference is digitized by the TDC module and sent to the computer for storage.

Fig.7.5 shows typical TDC spectra from 4 straw tubes. All spectra are free of background and show the same characteristics. In order to reconstruct the tracks of the cosmic rays, we must convert these time informations into radial distances (see 3.3). It is done by a calibration process called *R(t)*-Calibration.

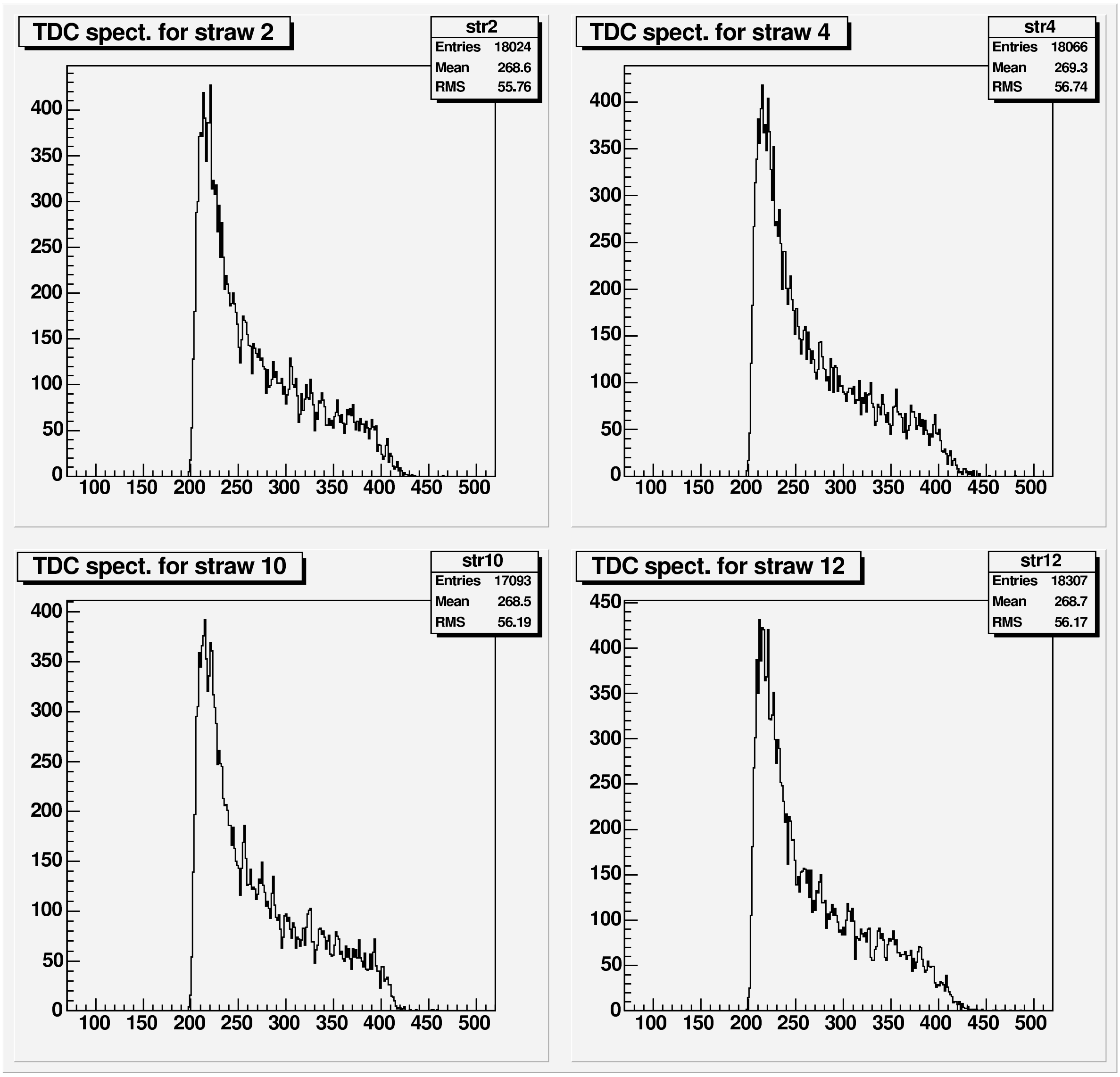

Figure 7.5: Measured drift times from 4 different straw tubes. x-axis is drift time (nsec) and y-axis is the counts.

7.3.2 R(t)-Calibration

The R(t)-calibration can be obtained from the shape of a measured drift time distribution. If we assume that the track density over the drift tube is independent of the distance to the wire, the probability $P(r)$ that a hit corresponds to a track between distance r and distance $r + dr$ from wire is given by

$$P(r)dr = c_1\eta(r)dr \tag{7.1}$$

where η is the hit efficiency of the tube and c_1 is a normalization constant. If the drift time t is a one to one function of the distance r, the drift time distribution is related to the distance distribution (7.1) by

$$P(r)dr = P(t)dt \tag{7.2}$$

For times in the interval $[t_a, t_b]$, $R(t)$ relation can be obtained by integration of the tdc spectrum and the efficiency profile,

$$\int_{r_a}^{r} P(r')dr' = \int_{t_a}^{t} P(t')dt' \tag{7.3}$$

If we assume that the efficiency is constant over the whole interval $[t_a, t_b]$, Eq.7.3 reduces to

$$R(t) = r_{wire} + \frac{\int_0^t P(t')dt'}{\int_0^{t_{max}} P(t')dt'}(r_{straw} - r_{wire})$$

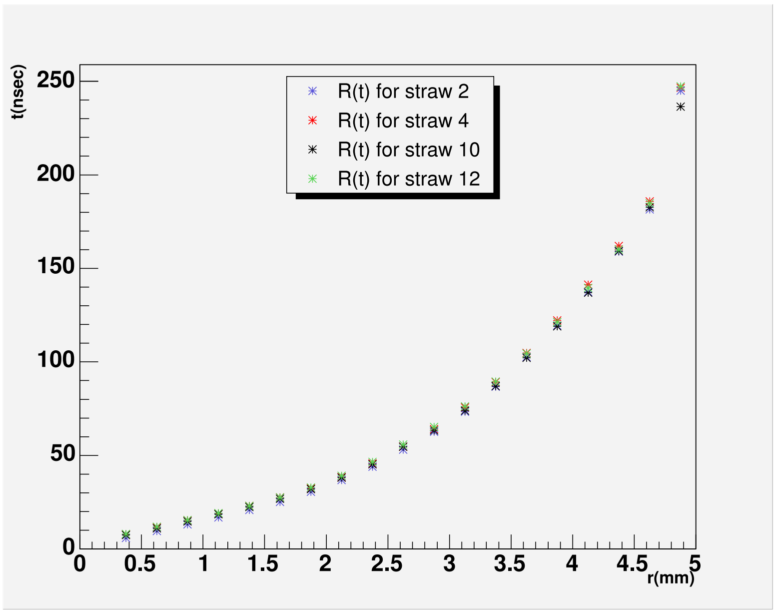

Figure 7.6: R(t) curves for the 4 straws from Fig.7.5 with 2 *bar* absolute pressure and 2040 *V* high voltage.

7.3.3 Tracking

In order to reconstruct the tracks of the cosmic particles in 3 dimensions unambiguously, 8 straw tubes (one and only one response from each plane) are required.

Each straw response corresponds in three dimensions to a cylinder with a radius r_i calculated from the drift time by using the R(t) curve. The cosmic tracks are reconstructed by applying a linear fit of the track parameters $P_{j=1\ldots 6}$ (denoting direction $\hat{g}_i$ and foot points $\vec{P}_i$ of the track), minimizing the χ^2:

$$\chi^2 = \frac{1}{N}\sum_{i=1}^{N}(\frac{\Delta r_i(P)}{\sigma_{r_i}})^2 \tag{7.4}$$

where $\Delta r_i = (DCA_i - r_i)$ is the shortest distance between track and cylinder r_i in straw i calculated by using "Distance of Closest Approach (DCA)" (Eq.7.5). σ_r denotes the spatial resolution at r_i and N the straw number on the track.

$$DCA = \frac{(\hat{g} \times \hat{g}_i)}{|\hat{g} \times \hat{g}_i|} \cdot (\vec{P} - \vec{P}_i) \tag{7.5}$$

where $\hat{g}$, $\hat{g}_i$ direction vectors and $\vec{P}$, $\vec{P}_i$ foot points of the wire and track.

We used the minimization package "TMinuit" of the ROOT framework [101] to find the track parameters giving the lowest value of the χ^2 in Eq.7.4. In Fig.7.7, the χ^2-histogram for 4815 reconstructed tracks is shown. Since we used a resolution (σ_r) of 0.250 mm which is larger than in reality in Eq.7.4, the peak in χ^2 histogram, expected at 1, is shifted to about 0.4. The resolution is therefore in the region of 0.16mm

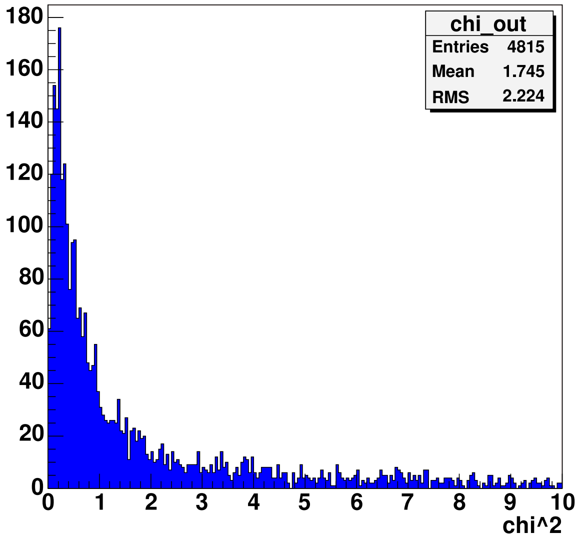

Figure 7.7: χ^2 histogram for 8 responses tracks

Fig.7.8 shows an example of a fitted track together with straw tubes (black circles) and cylinders (red circles) in two dimension.

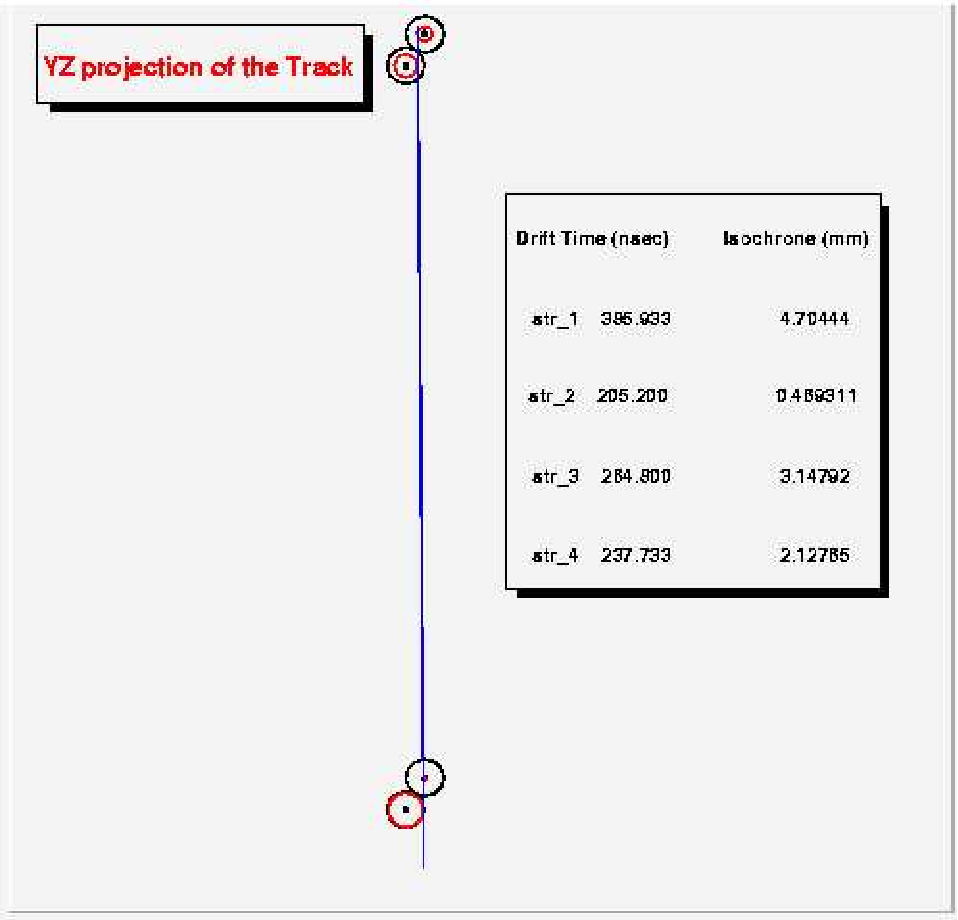

	Drift Time (nsec)	Isochrone (mm)
str_1	395.933	4.70444
str_2	205.200	0.469311
str_3	264.800	3.14792
str_4	237.733	2.12785

Figure 7.8: Fitted plane in which track (blue line) lies together with straw tubes (black circles) and the cylinders (red circles) in 2 dimension (YZ-plane projection along x axis). Straw numbers (str_1,2,3,4) increase from bottom to top.

7.4 Efficiency of the Test Facility

A cosmic track hitting 8 straws should provoke responses from 8 straws in ideal case. Fig.7.9 shows the distribution of the number of responding straws in the cosmic ray test facility. In this histogram the events with more than one response per plane are not included (at most one hit per plane is allowed).

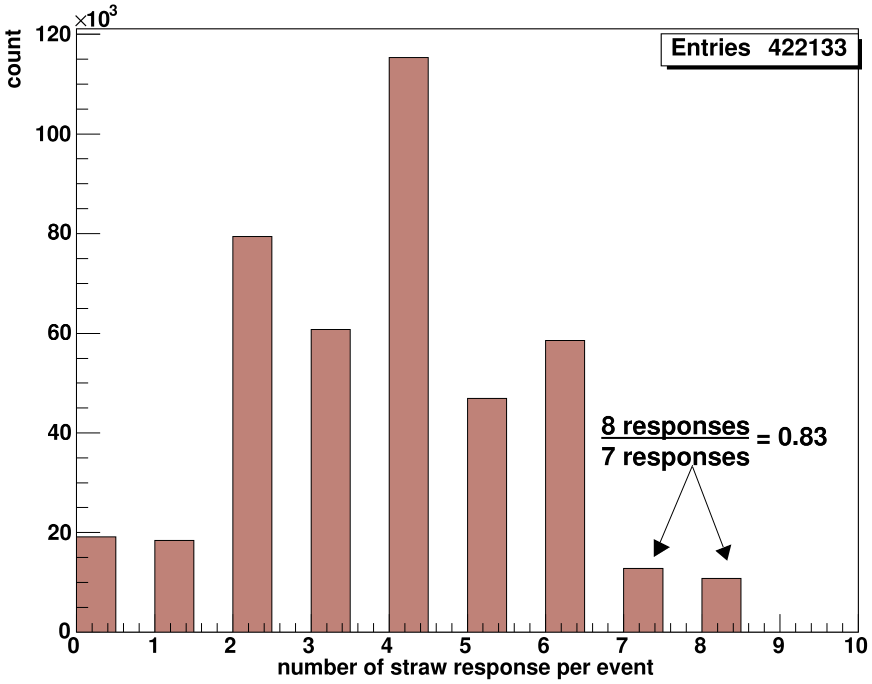

Figure 7.9: Distribution of firing straws out of 8 straw responses (one per plane at most) in the test facility. The corrected ratio (8 *responses*/7 *responses*) under geometry consideration amounts to ≈ 95.

In order to estimate the single straw tube efficiency in the test facility we used the relative efficiency of event types *"7 responses out of 8 straws"* and *"8 responses out of 8 straws"*. From Fig.7.9 we have 8 *responses*/7 *responses* ≈ 0.83. In the case of 7 responses out of 8 hits we have 3 fully functioning double planes. In one of the double planes only one straw responds. There is $1cm$ width with only one straw in the double plane ($\pm 5mm$ offset) of $8.5cm$ total width. So $1cm/8.5cm \approx 12\%$ of the 7 responses (one missing) is due to geometry not due to inefficiency.

So we have to reduce the "7 responses" number in Fig.7.9 by this percentage and get 8 *responses*/7 *responses* ≈ 0.95.

If there would be no systematic errors and all straws behave in the same way then statistical considerations would lead to response distributions with ratios which are defined by the single straw efficiency ϵ alone. Only 7 and 8 response events are comparable due to the same well defined geometrical acceptance.

In order to find out the straw efficiency we have calculated the dependency between probability of getting a certain number of responses per event and the efficiency of straw tubes (see appendix C for the calculation). Fig.7.10 shows probabilities of getting 7 and 8 response events versus the single straw efficiency. The point at which the relative probability

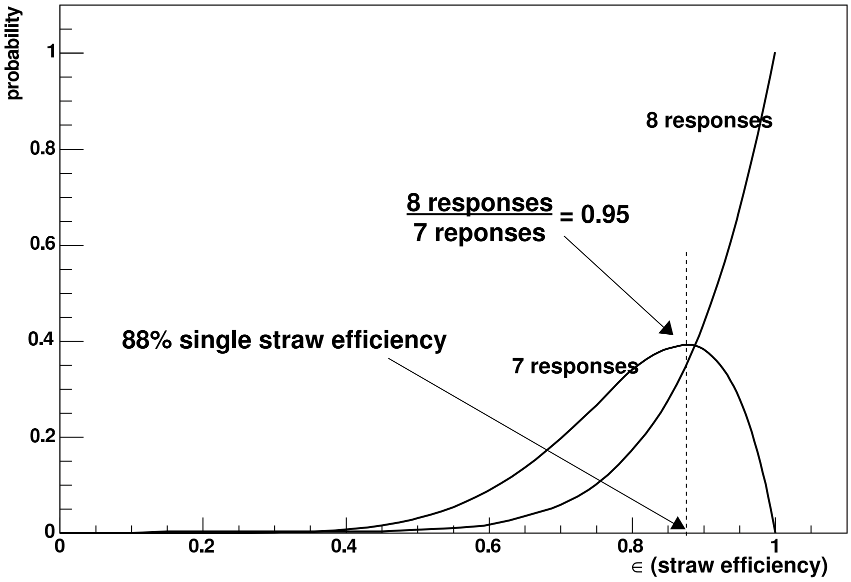

Figure 7.10: Dependence of firing number of straws out of 8 planes as function of a common single straw efficiency ϵ.

P_8/P_7 is equal to 0.95,

$$P_8(8)/P_8(7) = \frac{\epsilon}{8(1-\epsilon)} = 0.95 \tag{7.6}$$

results in an efficiency $\epsilon \approx 88\%$. The observed inefficiency of $\approx 10\%$ is mostly due to the aging effects of some of the straws exposed to the beam (see 5.5).

Of course we see that the numbers for less than 7 responses per 8 planes are by far higher than expected by a purely statistical interpretation. This can be understood by inspection of Fig.7.11 and is related to a much bigger acceptance for 6 (or less) response events.

Fig.7.11 shows the multiplicity distribution of the four double planes (in logarithmic scale). The clear peak at two responses per double plane shows proper functioning. The zero response in the situation where straws (3. and 4. plane) and trigger scintillators are parallel are as expected lower than in the situation where straws (1. and 2. plane) and trigger scintillators are orthogonal to each other. If the straws are orthogonal to the trigger paddles the only $8cm$ occupied by straws out of the $30cm$ long paddles can make only relatively few straw responses and as consequence a fraction of about $(30-8)/30$ 2.2 out of 3 triggers have no straw response. This explains why 4 response events are maximum (7.9); two double planes parallel to the trigger scintillators have the maximum overlap area with scintillators (giving maximum cosmic ray illumination area). By addition of other planes the the overlap area with trigger scintillators decreases, therefore the number of events having higher straw responses (> 4 straw responses) too.

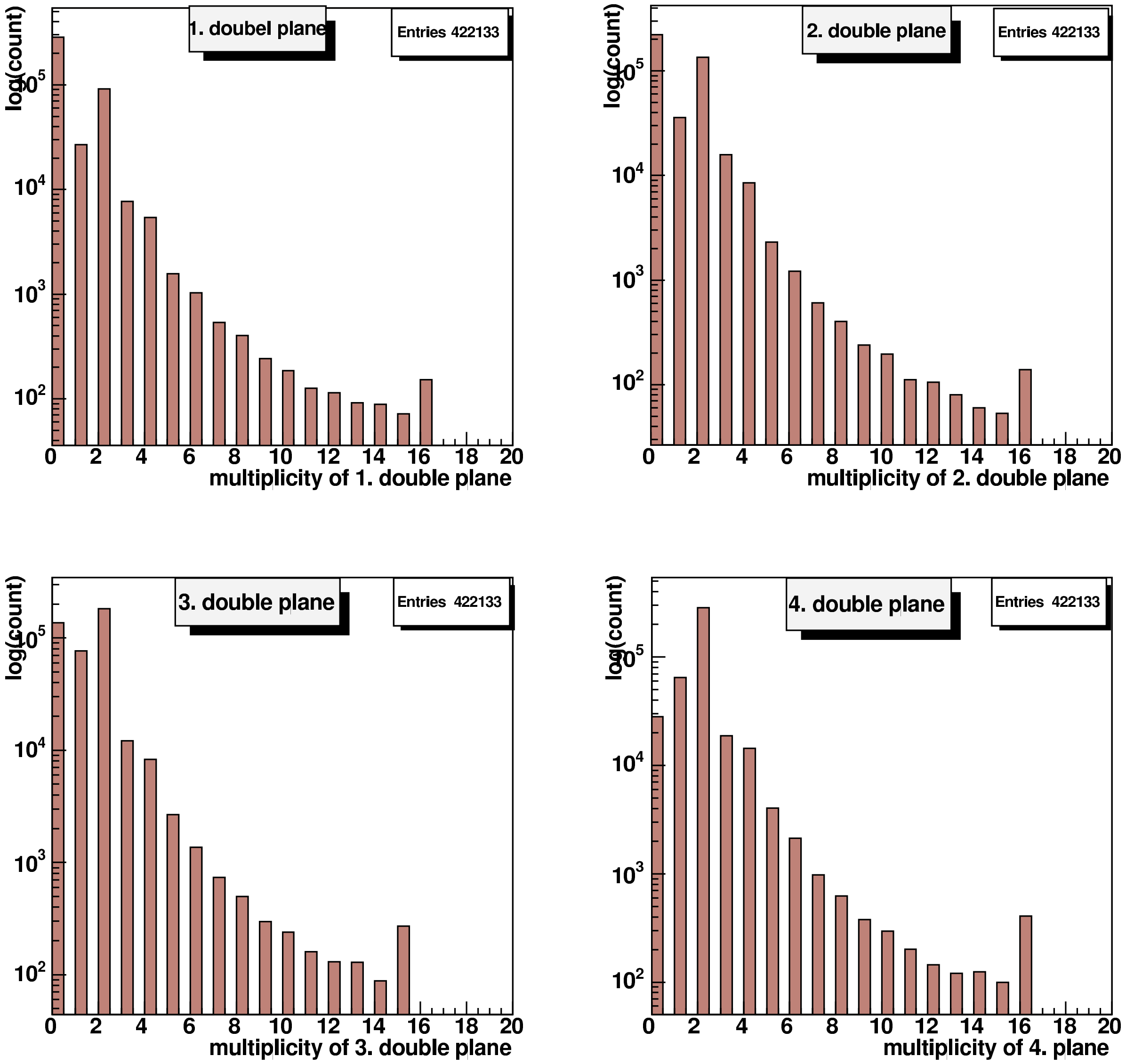

Figure 7.11: Response multiplicity of the 4 double planes. 1. and 2. double planes are orthogonal and 3. 4. planes parallel to the trigger scintillators.

In Fig.7.11 the cross talk dominating at 1 response (but existing up to 16 responses) is also seen. The electronic shielding of the system must be improved in order to minimize the cross talk.

7.5 Geometry Reconstruction with the Test Facility

In order to assure that the test setup works properly, we reconstructed the geometries of two different test scintillators. One is with a circular shape having a diameter of 5 *cm* and thickness of 5 *mm* and the other one is a square shaped scintillator with a size of $4 \times 3.8 \times 0.2cm^3$.

The reconstruction of the cosmic particle tracks provides us with the illuminating field. Fig.7.12 shows simulated hit distributions between two trigger scintillators (the radii corresponds to the hit density). One sees that the hit density is not flat due to the geometrical acceptance of the scintillators. Especially in a plane in the center one expects highest track density in the middle. Close to the trigger scintillators the expected hit distributions become flat.

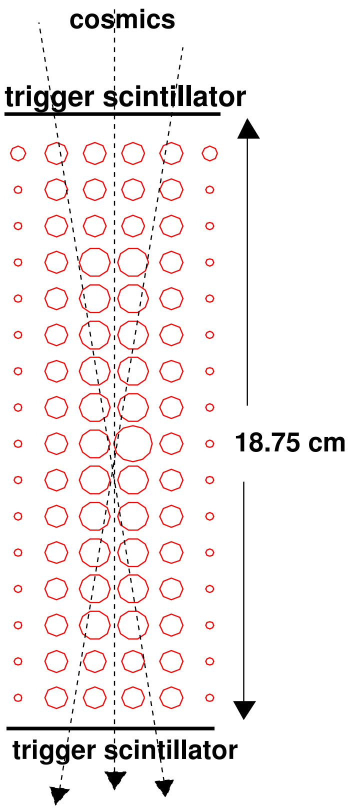

Figure 7.12: Simulated cosmic hit distribution between the two trigger scintillators. Close to the scintillators the hit distribution is uniform. Between the scintillators the hit distribution peaks in the center.

Fig.7.13 shows the measured points where the cosmic tracks pass the plane of the circular test scintillator. The illuminating field distribution is more irregularly modulated than the geometrical acceptance of the trigger scintillators alone could explain. This is due to the nonuniform efficiencies of the damaged straws (see section 5.5). Whenever one uses such a test facility this illumination density must be provided. It allows to calibrate the efficiency distribution on the test object.

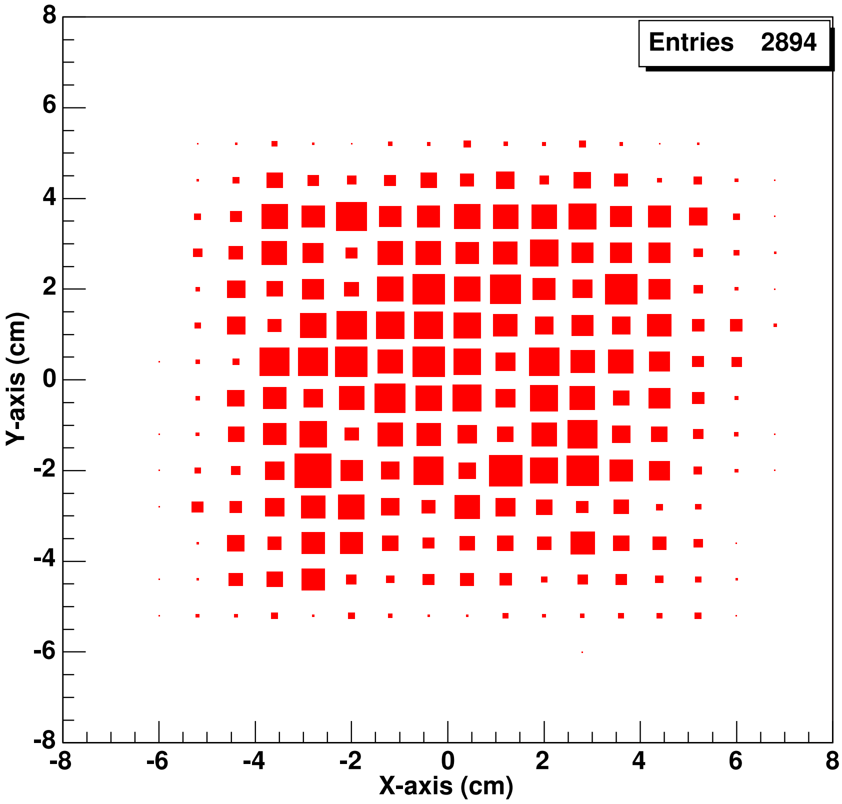

Figure 7.13: Illumination distribution of cosmic tracks on the circular test scintillator plane. 8 and only 8 fired straws from 8 planes are required. The observed density fluctuations come from a folding of different straw efficiencies. A $\chi^2 < 5$ (Fig.7.7) cut on track fitting is applied.

The test scintillators are connected to QDC and TDC modules for an identification of their position dependent responses. Fig.7.14 shows the QDC and TDC spectra of the circular test scintillator.

The events in which the test scintillator is hit, are selected by setting a cut on scintillator's TDC and QDC. For the circular scintillator we set $270 \leq tdc \leq 290$ and $qdc \geq 90$.

Fig.7.15 shows the remaining hit points of the cosmic ray illuminating field when these coincidence conditions and a $\chi^2 < 5$ (Fig.7.7) are required on the circular scintillator. 610 hits are in the figure. The few points remaining outside are not background. They are due

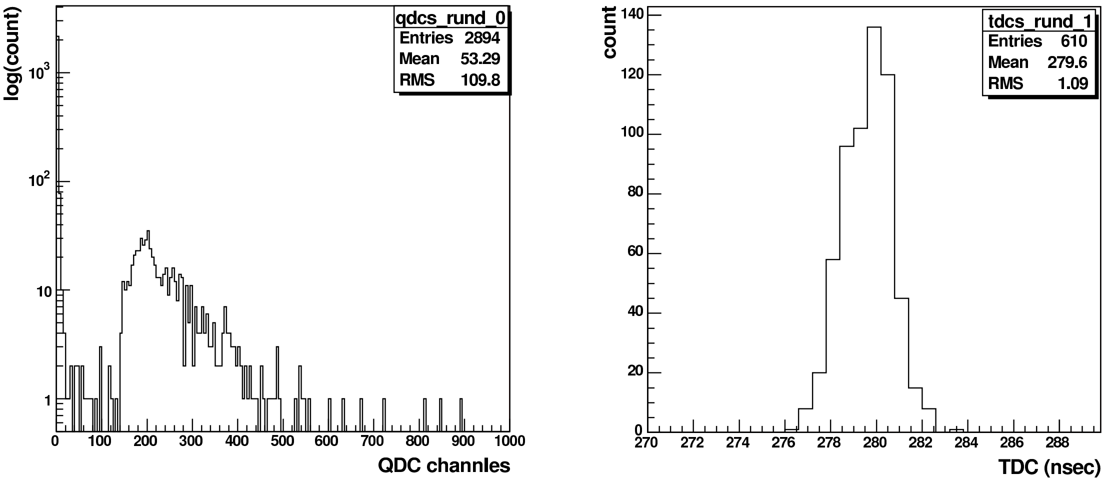

Figure 7.14: QDC (left) and TDC (right) values of the circular test scintillator.

to the Cherenkov radiation from the plexiglass light guide (see 7.7).

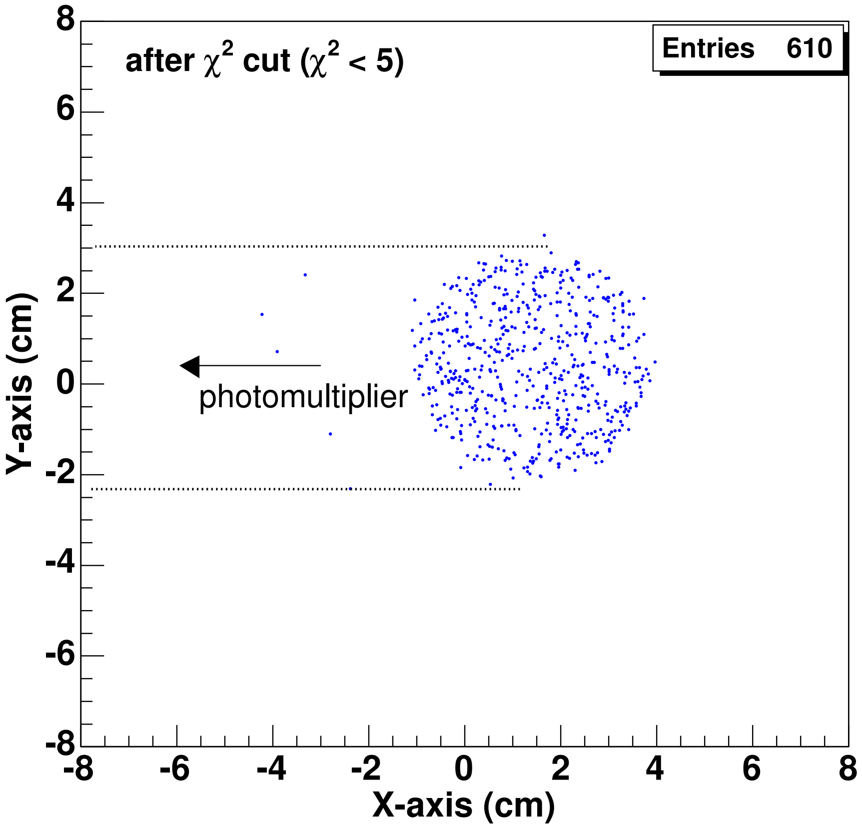

Figure 7.15: Geometry of the circular test scintillator with some few Cherenkov light responses from the plexi light guide.

Fig.7.16 shows all hit points of the cosmics on the test scintillator planes (same as Fig.7.13) and the points with the test scintillator used as a veto (right). There we find about 20 events remaining in the scintillator position if we exclude hits with scintillator response. The 3% of irregular events might be either due to wrong track interpretation due to the cross talk or to discriminator inefficiency for the test scintillator. This second explanation seems to be unprobable. We had the discriminator level for the TDC below the single electron amplitude. The chance to have 3% zero triggers would mean, that the average scintillator amplitude would be below ≈ 3.5 dynode electron amplitude. The real signal (Fig.7.14) is definitely higher.

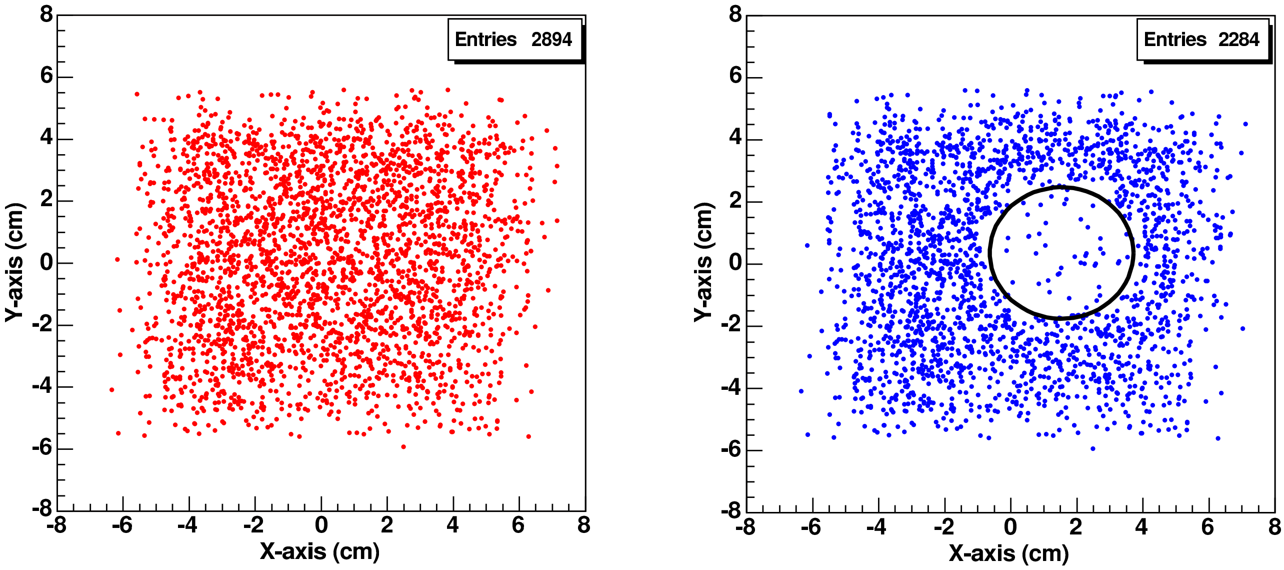

Figure 7.16: Left: hit points of the all cosmic tracks (same as in Fig.7.13) on the test scintillator's plane. Right: hit distribution with the test scintillator response as veto.

Fig.7.17 shows the illuminating field distribution on the square scintillator's plane. There is difference compared to Fig.7.13 that can be simply explained by the different position of the two planes.

The TDC and QDC cut for the square scintillator (Fig.7.18 shows the TDC and QDC spectra) are $190 \leq tdc \leq 220$ and $qdc \geq 450$ respectively.

Applying these QDC, TDC conditions and χ^2 cut we get the hit distribution in Fig.7.19. It shows the geometry of the square test scintillator with very few hits outside. The mirror light guide used here does not give Cherenkov light.

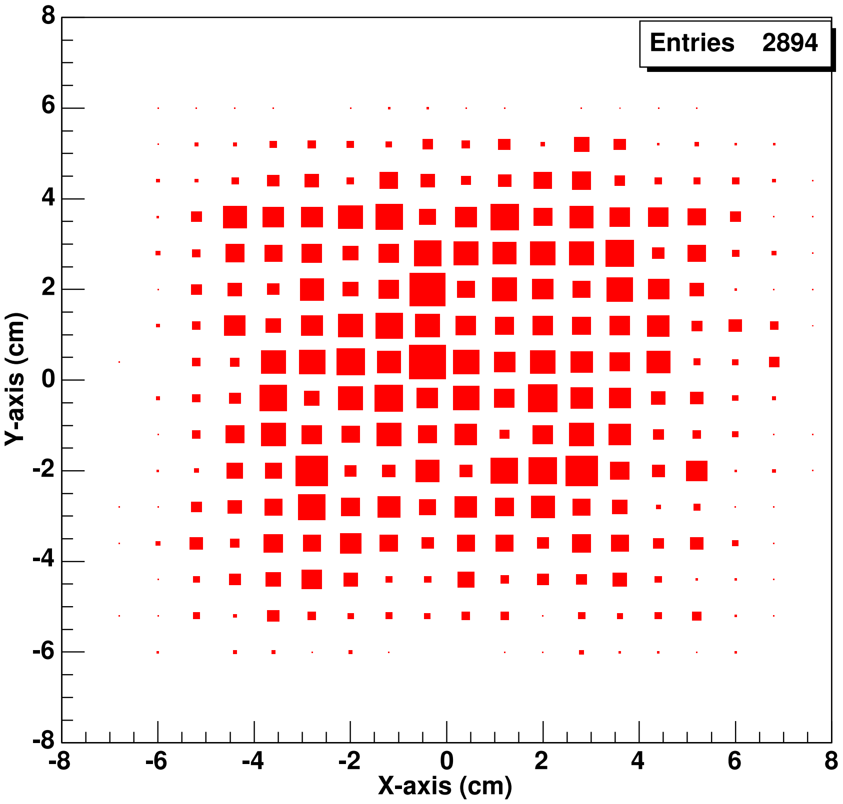

Figure 7.17: Illumination distribution of cosmic tracks on the square test scintillator.

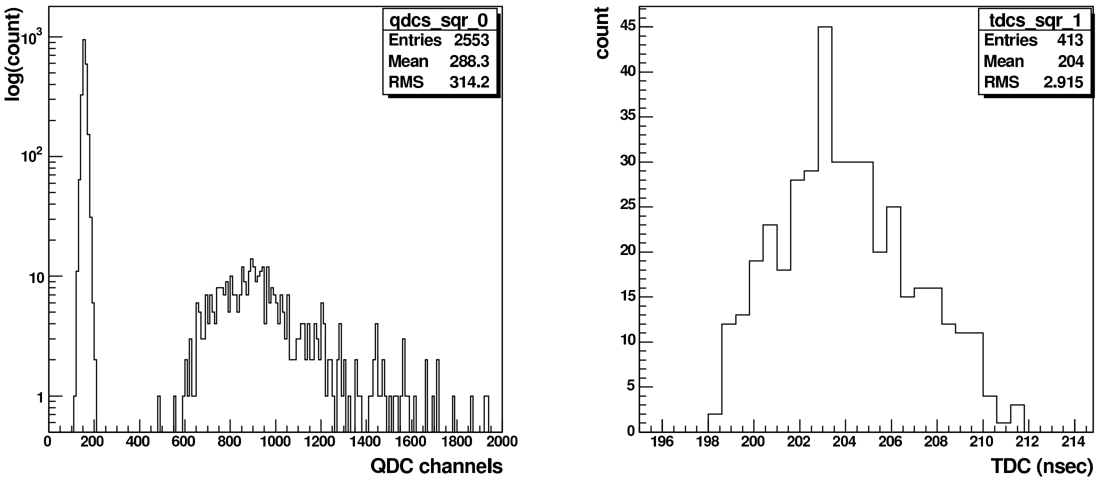

Figure 7.18: QDC (left) and TDC (right) values of the square test scintillator.

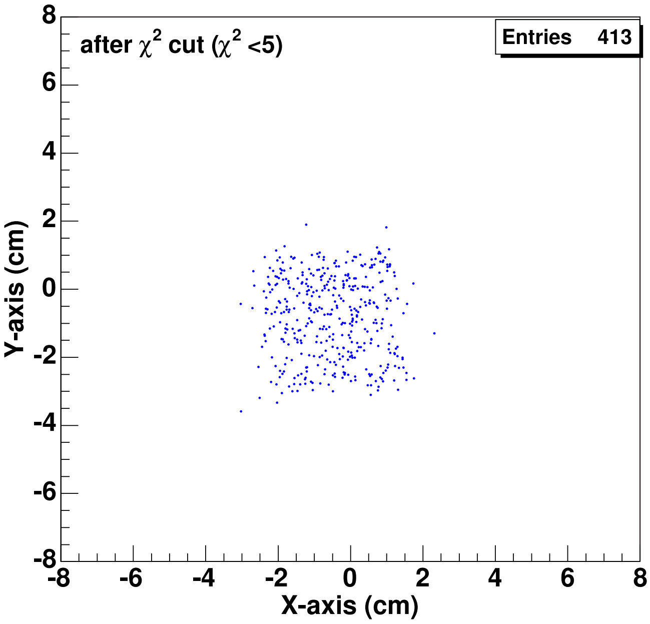

Figure 7.19: Geometry of test scintillators, after $\chi^2 cut$.

Fig.7.20 shows all hit points of the cosmics on the square scintillator planes like illuminating field Fig.7.17 and the remaining sample with the test scintillator hits used as a veto (right).

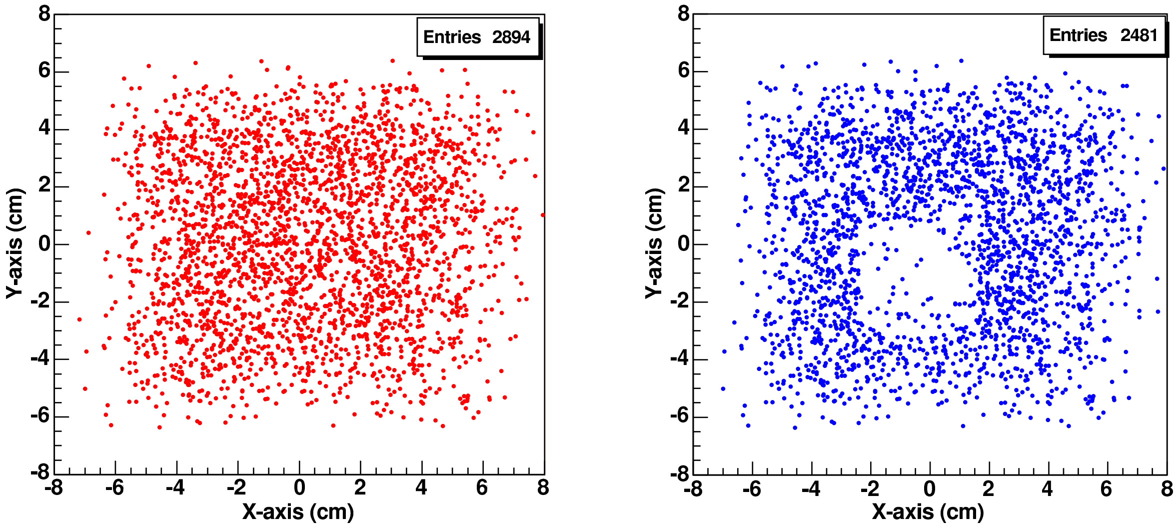

Figure 7.20: Left: hit points of the all cosmic tracks on the square test scintillator's plane (same as in Fig.7.17). Right: hit distribution with the test scintillator response as veto.

7.6 Position Dependency of the Scintillator Response

The test facility allows to measure the light output from cosmics tracks depending on the hit positions (see section 7.5). This may produce quite strong effects (see appendix B).

Fig.7.21 and Fig.7.23 shows the QDC values along the axis of light guide (a) and along the transversal axis (b) for circular and square scintillators respectively. We see from the right figure in Fig.7.21 that the light gain along the y-axis is uniform, but in the left figure it is seen that the light gain increases strongly with increasing x by going away from the light guide.

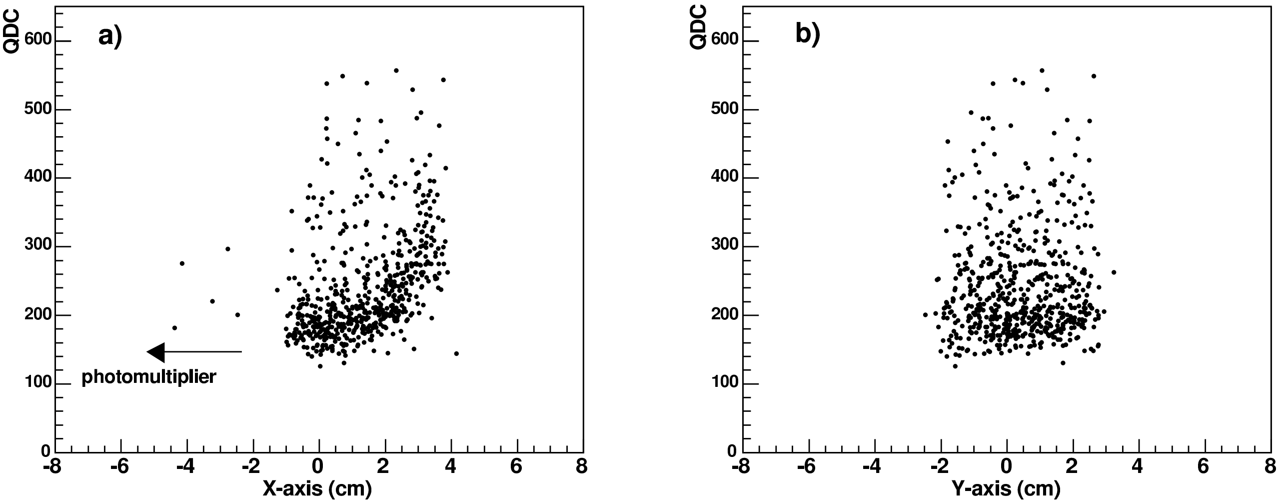

Figure 7.21: QDC values for light output of the circular test scintillator along the axis of light guide a) and along the transversal axis b).

This strong enhancement of the light output is based on focusing of the light, reflected from the open 180^0 cylindrical boundary of the scintillator into the light guide which is glued on the other 180^0 of the cylinder surface [14]. This principle is indicated in Fig.7.22.

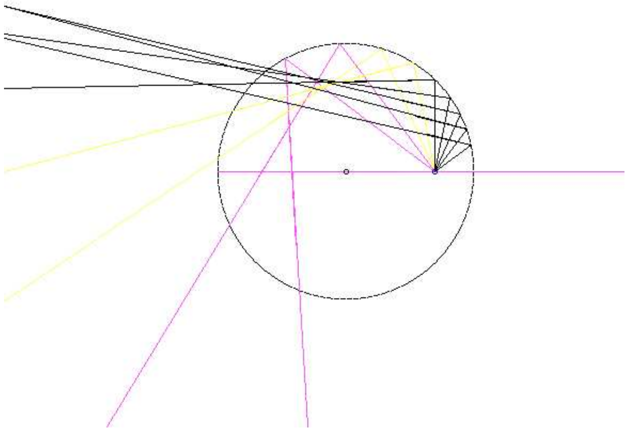

Figure 7.22: Quasi focal point in a circular scintillator which gives about parallel reflected light from the cylindrical boundary [14]. This focusing disappears when the light is emitted from points closer to the light guide (left).

The square scintillator with its mirror light guide shows a uniform distribution (Fig.7.23).

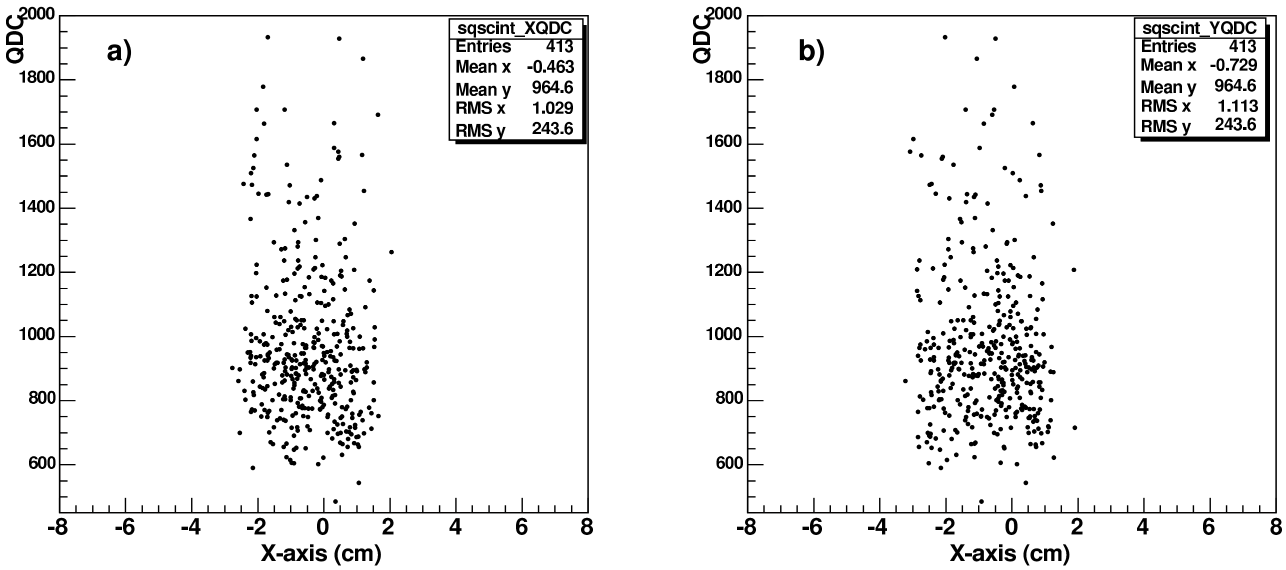

Figure 7.23: QDC values of the square test scintillator along the axis of light guide a) and along the transversal axis b).

7.7 Measurement of the Cherenkov Radiation

Cherenkov radiation is emitted whenever charged particles pass through matter with a velocity v exceeding the velocity of light in the medium [102],

$$v > v_t = \frac{c}{n} \tag{7.7}$$

where n is the refractive index of the medium, c velocity of the light in vacuum and v_t threshold velocity.

The square scintillator with its $10cm$ long mirror light guide shines its light into a $4cm\emptyset$, $10cm$ long plexiglass light guide in front of the PM tube. Fig.7.24 shows the reconstructed hit distribution (left figure) and QDC values (right) of the response when this the plastic light guide is moved into the illuminating field of cosmic track (the scintillator in this case far out of the triggered region).

Fig.7.24 has no sharp boundary. This may be due to the reduced track lengths and light output at the plexi cylinder boundary. The QDC spectrum from Cherenkov light (Fig.7.24 right) is dominated by the single dynode electron peak which appears at about 160 on the amplitude scale while zero amplitude is at about 130 in Fig.7.24. The single electron amplitude is about 30 units.

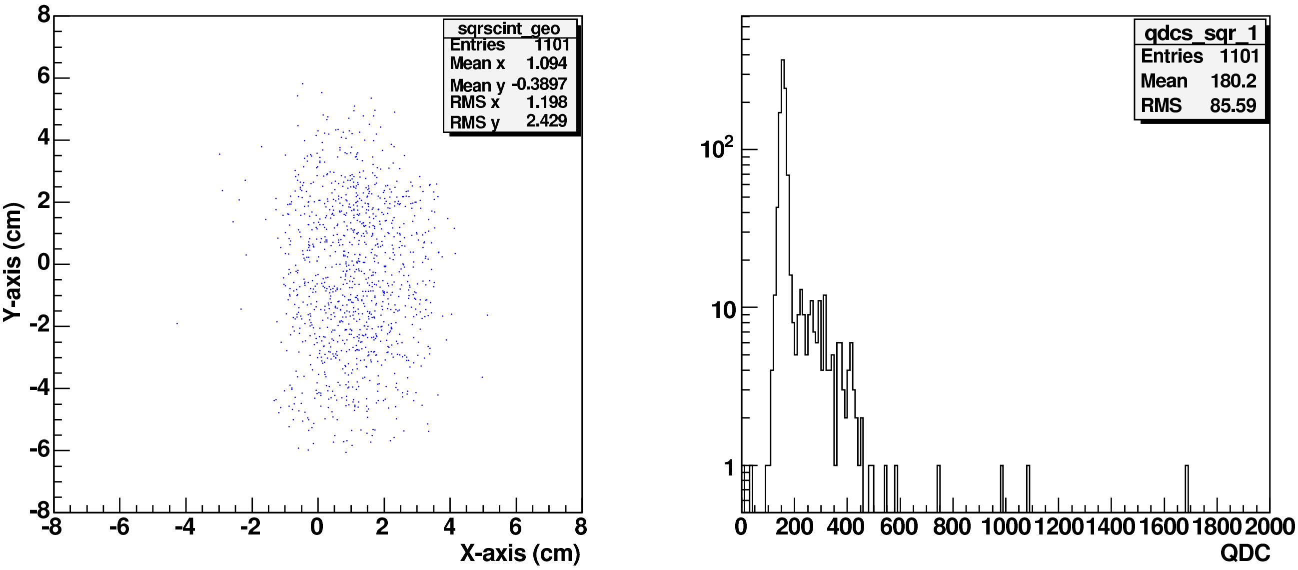

Figure 7.24: Left geometry of the plastic light guide, right QDC values from the light guide.

In Fig.7.25 the superposition of the QDC spectra from square scintillator (Fig.7.18) and light guide is shown. The scintillator response is at about 930, thus the scintillator amplitude is $930 - 130 = 800$. We find that the scintillator creates $800/30 \approx 27$ dynode electrons on the PM.

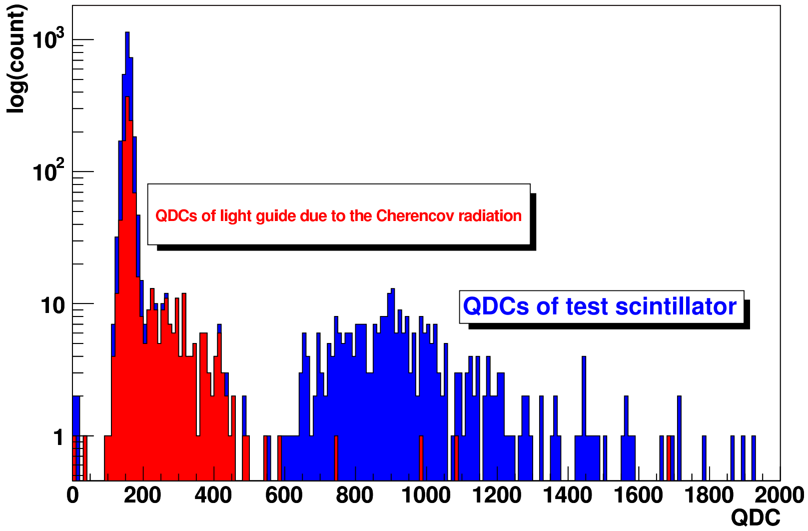

Figure 7.25: Superposition of the QDC spectra from scintillator and light guide.

7.8 Straw Tube

By using the test facility we measured also the response of a straw tube with the same procedures described in section 7.5.

Fig.7.26 shows cosmic hit distribution (illuminating field) on the test wire plane (left) and the same distribution without straw responses (right).

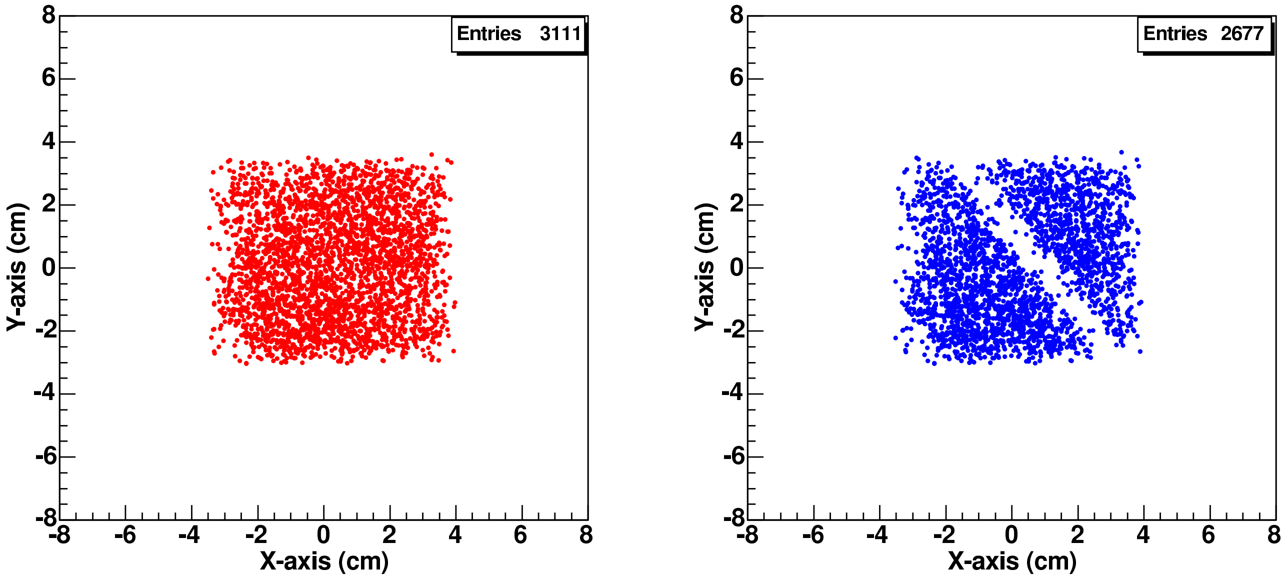

Figure 7.26: Left: hit distribution of the cosmic ray on the wire plane. Right: same distribution with test straw as veto.

Fig.7.27 shows the hit positions in coincidence with the straw. The pattern is clean.

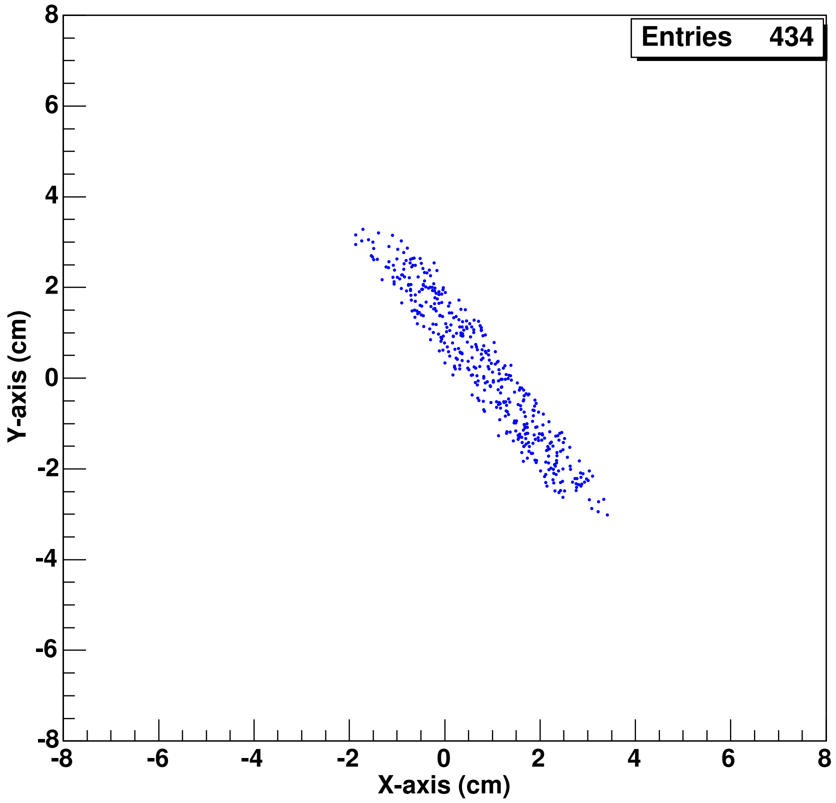

Figure 7.27: Reconstructed geometry of the straw tube.

Before we can determine the resolution of the test straw, we need to know the precise wire position (in space). There is a very simple method to find the position: for each hit point in coincidence with the test straw, we calculate the track distance to the anode wire. If we make circles with this distances as radius around the hit points, then we expect to see the wire as tangent to all these circles (if the reference plane is correct by known). Fig.7.28 shows an example with 8 hits and fitted tangent to the circles. In Fig.7.29 all circles together with the fitted wire are shown.

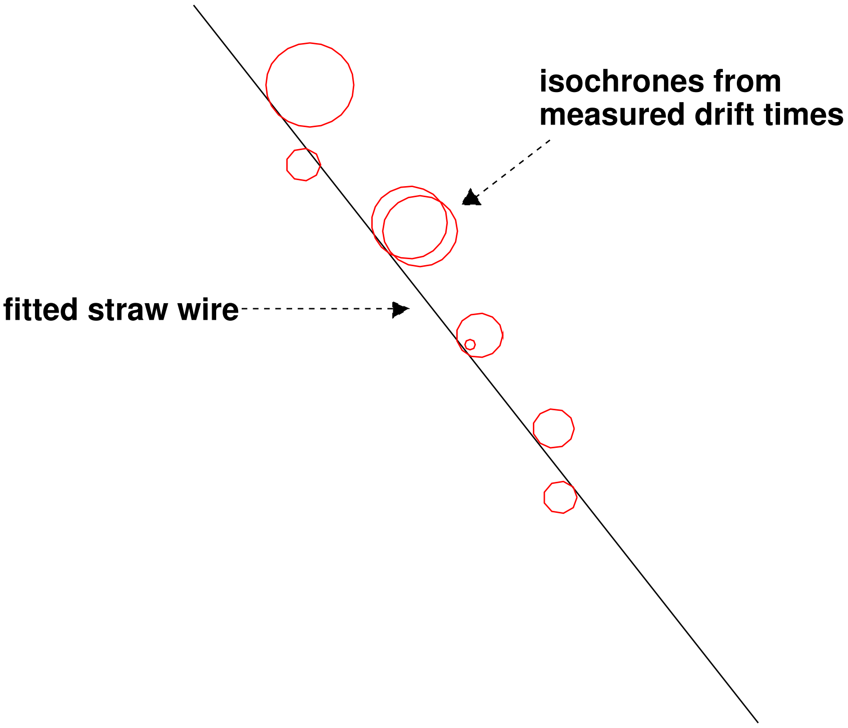

Figure 7.28: A few radial distance circles calculated from the R(t) calibration curve are drawn around the track positions. The wire position appears as tangent to the distance circles.

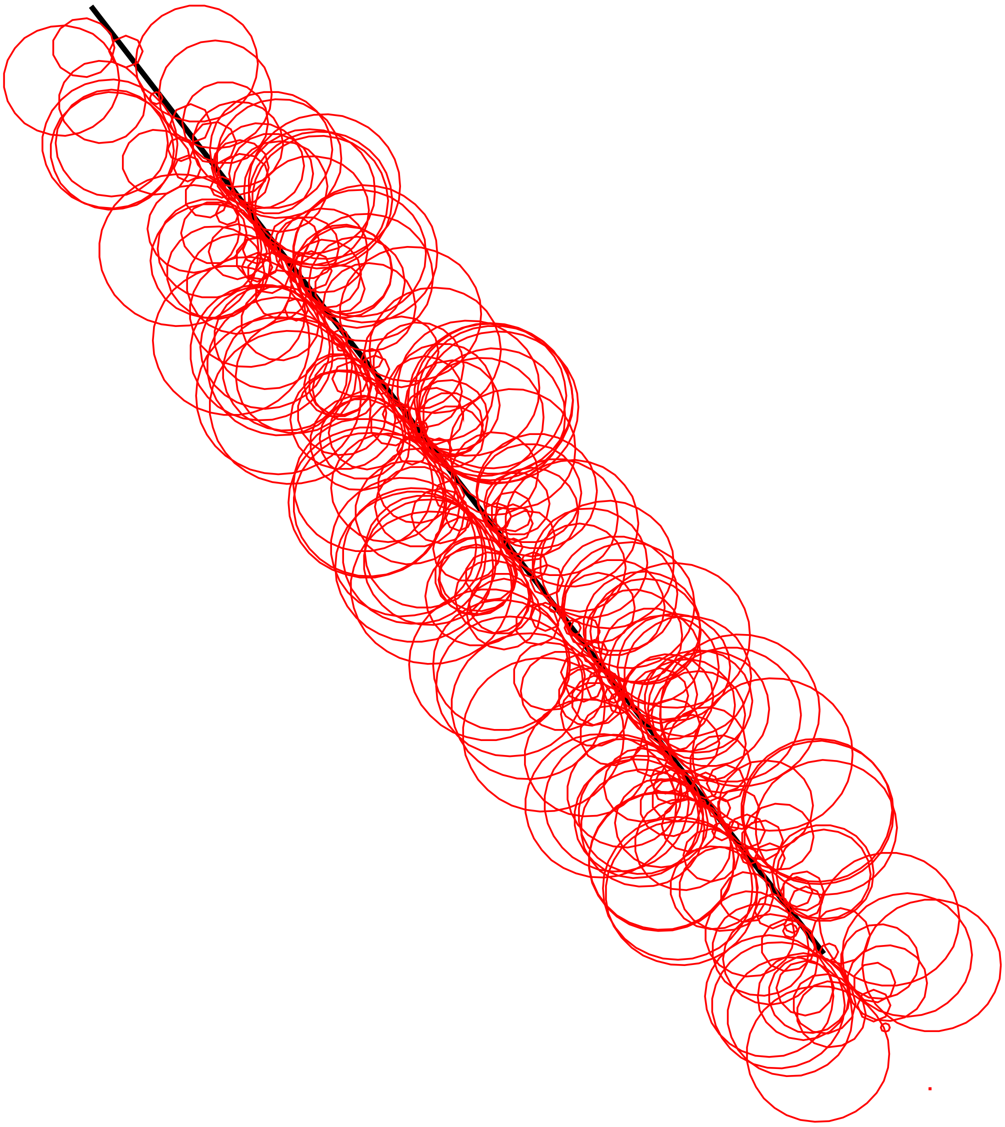

Figure 7.29: The full set of distance circles together with the resulting tangent which approximates the wire position.

After the determination of the wire position one can calculate the distance between this approximated *"best"* wire position and the hit position determined by the cosmic ray tracker, giving an expected radius. Fig.7.30 shows the expected radius determined from wire position and hit points on horizontal axis and radius determined from straw timing and $R(t)$ calibration on vertical axis.

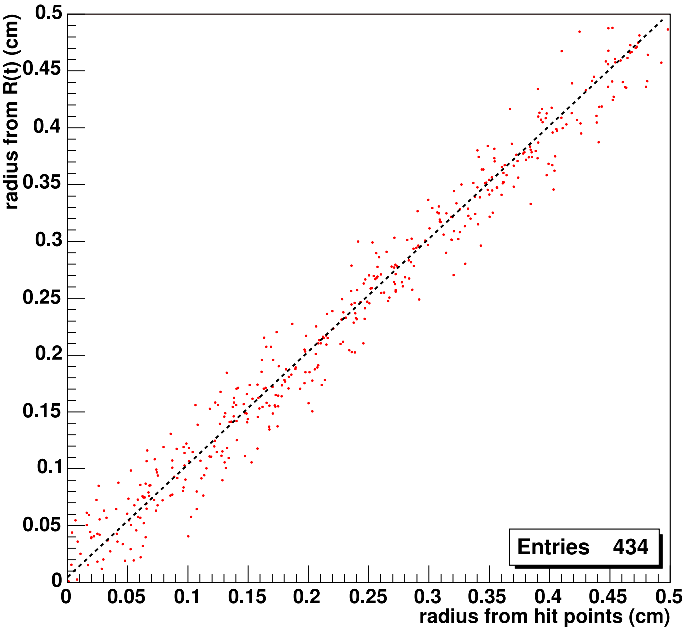

Figure 7.30: The expected radius determined from wire position and hit points on horizontal axis and radius determined from straw timing and $R(t)$ calibration on vertical axis.

Fig.7.31 shows the difference between the radii determined from R(t) calibration and from wire position and the hit position, giving the a folding of the tracker resolution and resolution of the test straw. The folded resolution of $\sigma = 228\mu m$ is obtained. For the single straw we now expect $\sigma_{straw} \approx 228\mu m/\sqrt{3} \approx 132\mu m$. It is comparable to the estimate in section 7.3.3 but higher than $85\mu m$ measurement described in section 5.8. The difference may be due to the systematic errors in the test facility. The straws in the test facility may have lost part of their positioning precision in the 3 years of test operation. One can see that they are not exactly coplanar any more. The time resolution in the TDC channels does not seem to have significant impact on the overall space resolution. The time resolution of the electronic system (including electronic delays) was determined by using a pulser. Digital signal from pulser was duplicated: one for the trigger signal and the other delayed signal for the TDC module (a constant time interval is expected at TDC spectrum). Fig.7.32 shows the TDC spectrum at two different delay times. At both time positions we have a FWHM of $\approx 8nsec$. With an average drift velocity of $5cm/\mu sec$ for the electrons in the gas we get a contribution of $\Delta r \approx 20\mu m$ to the space resolution (only due to the time resolution of the system).

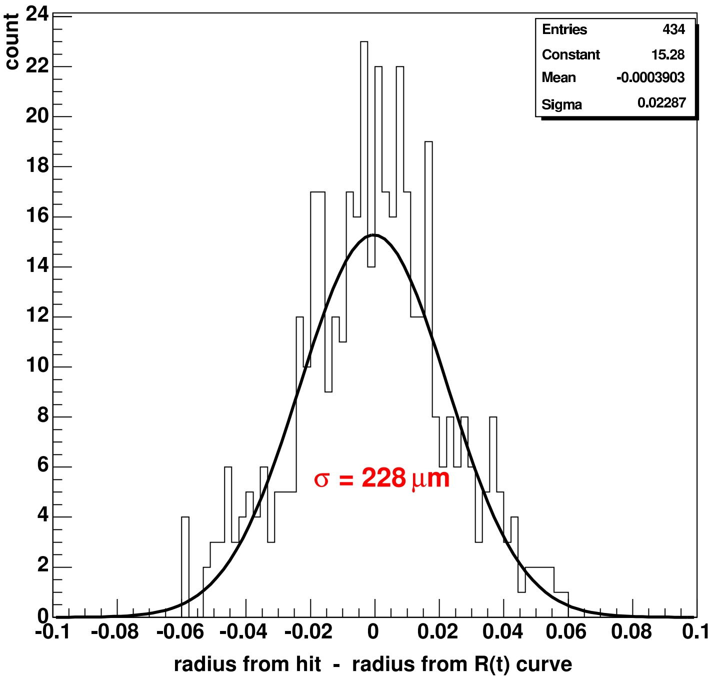

Figure 7.31: $r_{R(t)\,calib}$ - $r_{hit\,points}$.

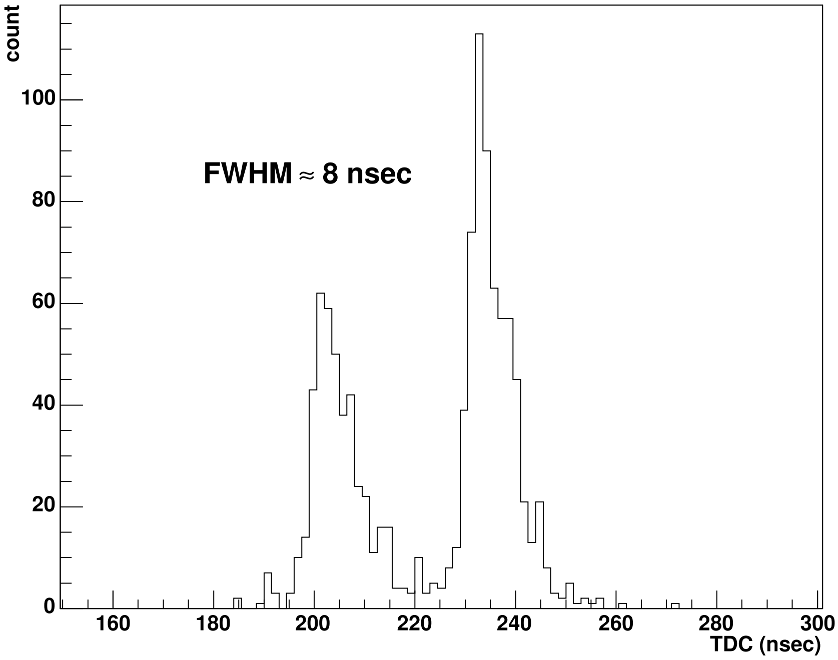

Figure 7.32: TDC resolution histogram. Obtained with pulser signals at two different time.

Summary

A new tracking detector *"Straw Tracker"* is under construction for COSY-TOF. Its purpose is to improve the tracking resolution and efficiency and to reduce inactive material, straggling and secondary reactions. Very important improvements in event reconstruction expected with the new tracker as shown by a Monte Carlo simulation.

A cosmic ray test facility from 128 straw tubes in 4 double planes was constructed in order to investigate practical applications and straw tracker properties in advance. Achieved were results on high rate capacity and aging effects. Aging with $ArCO_2$ counting gas was found with 10^{11} particles per cm counting wire. Clearly visible effects on wire and cathode appear.

The electronics of the test facility is optimized; the oscillation problem of the ASD-8 chip was solved. A stable state of the electronics was obtained. A stand alone data acquisition system (DAQ) was built. At present 64 channels are fully equipped which gives two working hodoscopes of $8 \times 8 cm^2$. 8 QDC channels for inspection of test detector response are available.

After completing the test facility, cosmic ray tracks were reconstructed in three dimension and test objects (2 test scintillators and a test straw tube) were investigated. The test facility works properly and is a very useful tool.

Some improvements should be made: some straw tubes which were degraded by tests with very high irradiation density should be exchanged. The number of active straw channels should be brought from 64 to 128 by adding the still missing 64 delay channels. This increases the useful tracker area by a factor four. Finally the mechanical precision of the straws should be recovered.

Appendix A

TofRoot Data Analysis Framework

A.1 Introduction

TofRoot is a ROOT based data analysis framework for the TOF [95]. It is developed in the University of Dresden by M. Schulte-Wissermann, C. Plettner, L. Karsch, S. Dshemuchadse, R. Jaekel, G.Y. Sun and W. Ullrich. The development goal of the TofRoot is to provide an efficient software environment for the analysis of the experimental data. Main requirements are transparency, stability, portability and extendibility .

TofRoot framework consists of mainly data containers, loop class over the event files, collection of help functions and the calibration database (see Table A.1).

Name	Description
Container Classes	Data storage and management
TofTrackParticle	Track information and kinematic calculations
TofAna	Loop class-loops over single or multiple files
TMatte	Function collection
TofCal	Database containing geometry and calibration data

Table A.1: The most important TofRoot classes

A.1.1 TofRoot Data Containers

To store large quantities of same class objects, ROOT provides the TTree and TNuple classes. The TTree class is optimized to reduce disk space and enhance access speed. A TNuple is a TTree which holds only floating point numbers; a TTree on the other hand can hold all kind of data, such as objects or arrays in addition to all the simple types [101].

TofRoot data containers uses the TTree structure to store data from the detectors. Each branch corresponds to a sub-detector of the TOF-spectrometer. Objects stored in the branches are detector data of each event [95]. A sketch of a container class is shown in Fig.A.1, where its placement within a data tree is indicated as well.

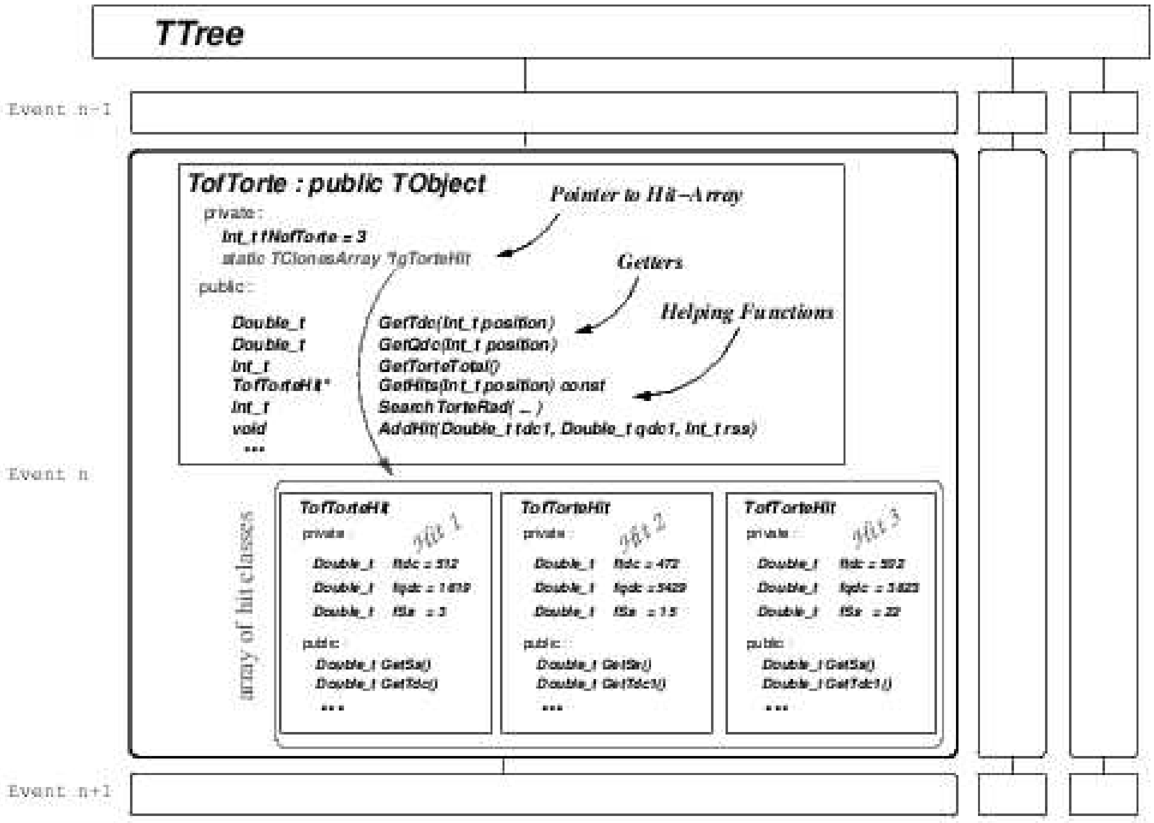

Figure A.1: Each container class represent a sub-detector of COSY-TOF. Information of each triggered channel is stored as a hit-class

A.1.2 TofAna - The Loop Class

The Loop class which is called TofAna makes the life easier for the data analyzer at communication with the experimental data stored in trees. To analyze data, the following routine works has to be carried out; opening the file, obtaining the tree/branch, creation of the data container instances, and the connection of these instances to the branches of the tree. All these steps can be annoying and boring for more than one file or run. To aid the user and minimize the time needed for such standard procedures, the loop class TofAna is developed [95]. Some important features of the TofAna are as follows:

- Dataloop, either one or multiple files.
- Creation of data containers, connection to the data tree(s).
- Opening and closing of the calibration file.
- Correct calibration data for each run.
- Reading/writing of all or user selected branches.

- Reading/writing of all or user selected events
- Reading/writing of all TofRoot data formats(RAW, LST, CALtemp, CAL).
- Run statistics.

A.1.3 TofCal - The Calibration Database

The calibration database TofCal contains offsets, factors and functions derived from the calibration of the data. Beside the calibration data, all geometric information of the subdetector positions and physical constants (e.g. speed of light, mass of the proton) are also contained in it.

A main feature of the TofRoot calibration chain and the TofCal calibration database is the automatic calibration of *each* run. This is a substantial difference to other analysis packages where only one calibration data-set is used for the total amount of data. During the calibration/conversion, the involved programs communicate with the database. They eventually read necessary data, perform calibration routines, and finally, the data for each individual run is stored in a directory like structure within the database (one directory per run). The TofCal is generated and filled during the calibration chain shown in Fig-A.2.

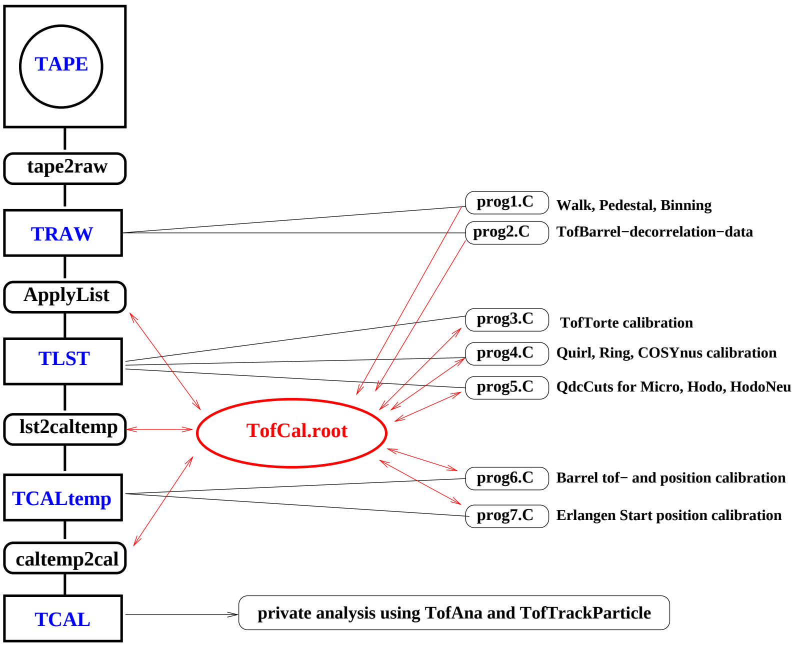

Figure A.2: Conversion of detector data from tape using four intermediate data formats (RAW, LST, CALtemp, CAL). The CAL-format is fully calibrated and the basis of all data analysis.

A.1.4 TofTrackParticle - The Track Class

The track class ”TofTrackParticle” contains all physical informations $(\beta, p, v, \phi, ...)$ about track and is designed to allow quick and easy access to these informations [95].

The TofTrackParticle is filled during the conversion from the CALtemp to the CAL format. By applying a linear fit algorithm to the hitted pixels of the start and stop detectors, one can discriminate the ”real tracks” from the background. If a track passes a χ^2-test, its direction, time of flight, the χ^2 value, the triggered QDC conversions and where to find the participating pixels in the data tree are stored in the class. All other physical observables are calculated *dynamically* by member functions of the TofTrackParticle. The design of the TofTrackParticle classes is totally independent of the track search algorithms. Therefore it will be no problem to implement a new track-search routine.

Appendix B

Calibration of the Raw Data

B.1 Introduction

During the experiment the raw data are stored in TDAS-Format (binary format) on magnetic tapes. This raw data contains the digitized information on the events, the response of each detector element recorded by ADCs, TDCs and scalers. Since this format is rather cumbersome and redundant for use in offline analysis, it is therefore converted by means of the program tdas2ascii to a ascii format convenient for the offline analysis. The offline evaluation program reads this format and performs necessary tasks to get desired physical observables. In order to obtain a physical observable two main steps have to be undertaken:

- The calibration parameters have to be determined.
- The algorithm for this observable has to be implemented.

A calibration parameter can be a cut-off value, an offset, or a factor. Only after the calibration process, the physical analysis can be started. The calibration process consists of following steps:

- Pedestal Subtraction
- TDC Module Calibration
- Walk Correction
- TDC Alignment of the Start Torte Quirl and Ring Detectors
- Absolute flight time calibration
- ADC Calibration

B.1.1 Pedestal Subtraction

Due to the charge integration of the base line, QDCs always show a positive nonzero conversion even in the absence of a hit. All these QDCs contribute to the data stream as a narrow and non physical peak at small QDC values; the so called pedestal or correct zero point of the QDC [95]. In the pedestal subtraction, individual QDC-cut values (pedestals) for each channel are determined and subtracted from the measured QDC value.

B.1.2 TDC Module Calibration

The TDC module used in the TOF has channel width of 100 ps in ideal case. In the TDC module calibration, the actual channel width of the module is determined. For this, a measurement using a time calibrator (ORTEC/EG&G 462) giving signals with $\Delta t = 10ns$ (corresponding to 100 TDC module channels) is done after each beam time [52].

B.1.3 Walk Correction

The output pulse from a discriminator appears at or just after the time instant when the input pulse crosses the threshold. Thus the time of appearance varies, or 'walks', with respect to the beginning of the pulse when either the pulse height or the threshold level changes [91]. In other words, the bigger the photomultiplier signal is, the earlier the discriminator reacts and with it the TDC. In the TOF, this effect leads to a deviation of $\Delta t = 3ns$ in the time which must be corrected [52].

The walk correction measurements are done with the laser calibration system developed for TOF. The light pulses from the laser are sent to the each elements of the start and stop detectors via quartz fiber. The amplitude of the pulses is damped with up to eight filters, in order to cover all QDC spectrum.

The walk correction proceeds in three steps: Firstly, pedestal subtraction must be done. In the second step, the ADC values from the walk measurements and the corresponding TDC values are filled in a histogram. At the final step, from the all entries a walk curve, is fitted:

$$TDC = (a) + \frac{b}{ADC + c}$$

where a, b, c are fit parameters.

B.1.4 TDC Alignment Of The Torte Detector

The torte detector consists of two consecutive scintillating rings, each divided into 12 in ϕ. Due to different cable lengths and different transit time in photomultipliers, TDC values from these two layers are distinct from each other by a constant offset for a hit. In the torte TDC calibration, these offsets are determined and TDCs from two layers are aligned.

To evaluate these offsets the TDC differences of all overlapping segments are filled into histograms. This yields 24 time differences between the segments, from which the 24 TDC offsets can be determined [95]. As a result, the time of flight is calculated using:

$$tof = TDC_{stop} - ((TDC_i + off_i) + (TDC_j + off_j))/2$$

To improve the time resolution arithmetic mean of TDCs from the two layers are taken.

B.1.5 Intern Quirl Ring TDC Calibration

The stop detector quirl and ring consists of 3 layers: a straight-layer and two (left/right) wound layers. The time of flight of the particle is calculated from TDCs of these layers and start detector. What we measure is not only the flight time of the particle but also light propagation time in the scintillator and signal run time in cable and electronic devices. Due to the difference in the geometry of layers (straight and wound) and different run time of signals resulted from distinction in cable lengths, 3 layers give 3 different TDC values for a particle hit. In the intern quirl ring TDC calibration time deviation of layers from each other are corrected and set to zero.

$$TDC_{straight} = TDC_{left} = TDC_{right}$$

The measured time of flight can be written as:

$$t_{meas}(l = 0..2) = t_{flight}(\beta, L) + t_{scint}(l, r) + t_{offset}(l, n)$$

where l is layer number, 0 is for straight, 1 for left wound and 2 is for right wound layer.
$t_{flight}(\beta, L)$: true flight time of particle depending on velocity β and distance L
$t_{scint}(l, r)$: run time of light in the scintillator depending on hit position r in the scintillator.
$t_{offset}(l, n)$: run time of signal in the cable and electronic devices
Using the fact that the signal run time in the two wound layers is same

$$t_{scint}(1, r) = t_{scint}(2, r)$$

one can obtain the offsets between left and right wound layers:

$$\begin{aligned} \Delta t_{meas}(i, j) &= t_{meas}(m = 1, i) - t_{meas}(m = 2, j) \\ &= t_{offset}(m = 1, i) - t_{offset}(m = 2, j) \end{aligned}$$

where i and j are the element numbers. After the calibration of the two wound layers with each other, calibration between straight and wound layers is done using:

$$\begin{aligned} \Delta t_{meas}(k, r) &= t_{meas}(m = 0, k) - \left(\frac{t_{meas}(m = 1, i) + t_{meas}(m = 2, j)}{2} \right) \\ &= t_{offset}(k) - \left(\frac{t_{offset}(m = 1, i) + t_{offset}(m = 2, j)}{2} \right) + \Delta t_{radial}(r) \end{aligned}$$

where

$$\Delta t_{radial}(r) = t_{scint}(m = 0, r) - t_{scint}(m = 1, r)$$

and k is element number of straight layer i, j are element numbers of left and right wound layers [96]. Fig.B.1 shows the TDC spectrum of the wound layers of the Quirl detector before (left) and after (right) calibration.

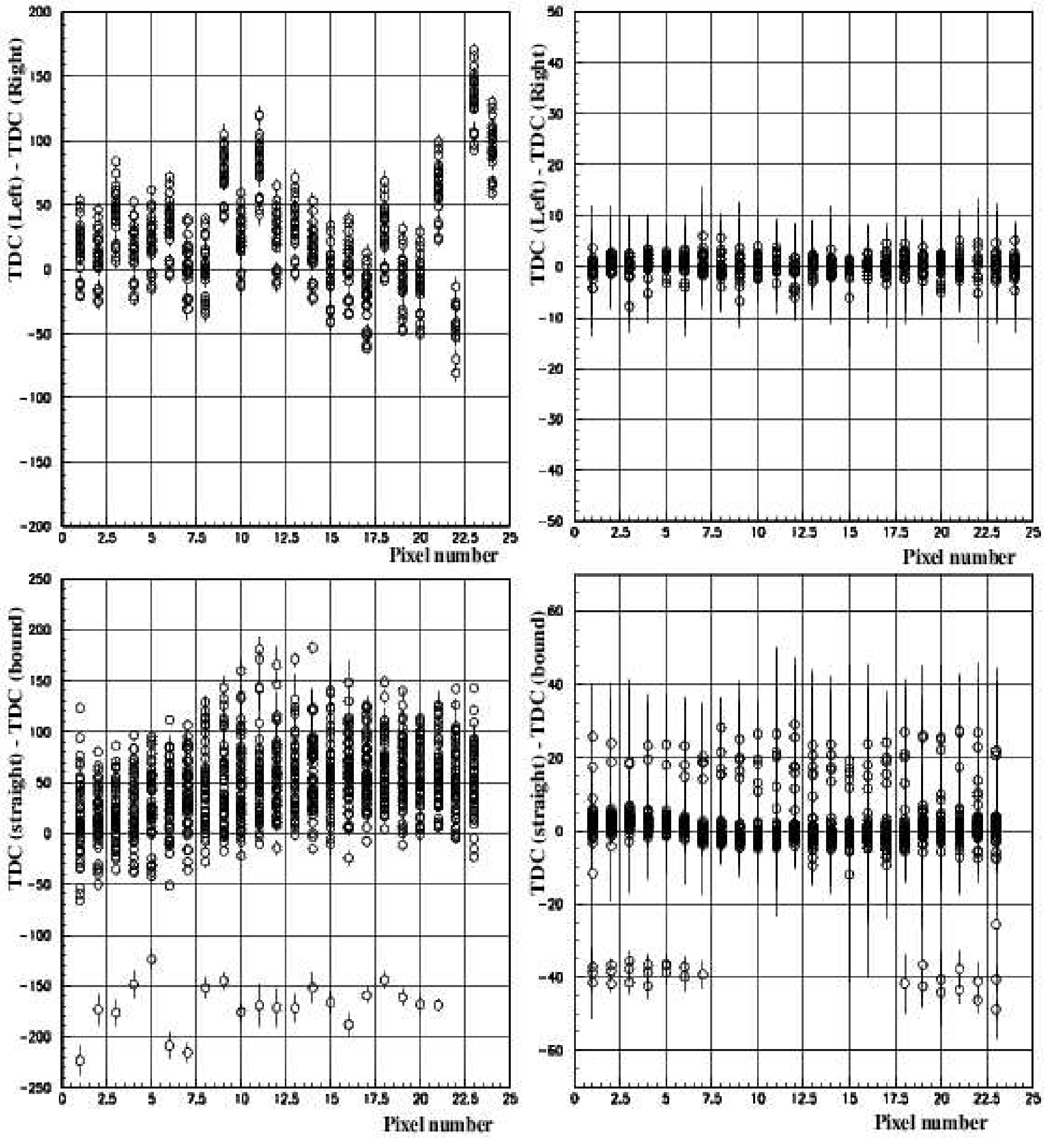

Figure B.1: The TDC spectrum of the wound layers of the Quirl detector before (left) and after (right) calibration. TDC values in units of 100 psec. Figure is taken from [55].

B.1.6 Absolute flight time calibration

After intern calibration of the detectors, the offset between start- and stop detector is determined. For this, either elastic proton scattering ($pp \rightarrow pp_{el}$) or deuteron pion ($pp \rightarrow d\pi^+$) production reactions is used. In two particle reactions, one can calculate the momentums of the particles from the scattering angles θ (with a mass hypothesis). From the momentum, the velocity of the particles can be obtained. Using the velocity and flight distance of the particle, one gets the expected flight time $TOF_{expected}$. The difference between measured and expected flight time which is the offset, is added to the TDC value of the start detector.

B.1.7 dE/dx Calibration of the ADS's

In addition to the TDC information there are three ADC values per pixel of the Quirl/Ring detector. The idea of the ADC calibration is the conversion of the digital information recorded by the ADCs during the experiment to corresponding energy deposited in the detector elements, which is calculated with the Bethe Bloch formula

$$\begin{aligned} -\frac{dE}{dx} &= \kappa z^2 \frac{Z}{A} \frac{1}{\beta^2} (\frac{1}{2} \ln \frac{2m_e c^2 \gamma^2 T_{max}}{I^2} - \beta^2 - \frac{\delta}{2}) \\ \kappa &= 4\pi N_A r_e^2 m_e c^2 = 0.307075 MeV g^{-1} cm^2 \end{aligned}$$

the relativistic velocity β is determined from the absolutely calibrated time of flight. The energy loss, varies with $1/\beta^2$ and decreases with increasing β until $\beta \approx 0.9$, where a minimum is reached which defines the minimum ionizing energy. The minimum value of energy of dE/dx is almost the same for all particles with the same charge.

A pixel consists of one straight segment, two spiral segments wound in opposite directions. An advantage of the used geometry is that each pixel provides the same accuracy in determination of polar and azimuthal angle (θ and ϕ) of the track independently of the scattering angle. There are 24x24x2 = 1152 pixels, with neglecting the central beam hole, and so 3x1152 histograms are defined, which describe the hit pixel of all detector segments. The light collection efficiency depend on the impact position of the detector elements, and varies particularly, for the curved segments along the radius [55].

In general the light output decreases from larger radii down to a minimum at radius of $\approx 30\,cm$ for the bent scintillator segments, and increases at the top of the elements. The variation of the light collection over a straight segment is smaller, as expected.

A calibration with raw data, where the energy and angle of a particle are correlated, are used to refine the calibration constants. A veto cut is applied on the used raw data for calibration to exclude the halo events and events not created in the target (non target associated particles). When the different detector hits have been combined into tracks, the impact position of the particle in each detector element is calculated. The ADC calibration subprogram is executed after absolute TDC calibration. For each pixel, the ADC and the calculated energy loss in the three layers are stored in three Histograms. Thus 3×1152 (total number of pixels) ADC calibration parameters are extracted.

For each detector segment the correction factors could be formulated as:

$$FADC = \frac{ADC_{measured}}{Radcor(\theta, \phi)}$$

where θ and ϕ determine the position of the hit pixel. Further corrections (offset and factor) similar to the TDC calibration also involved in the calibration subprogram. The ADC spectrum for the three layers of the Quirl detector versus the pixel number before and after calibration is shown in FigB.2.

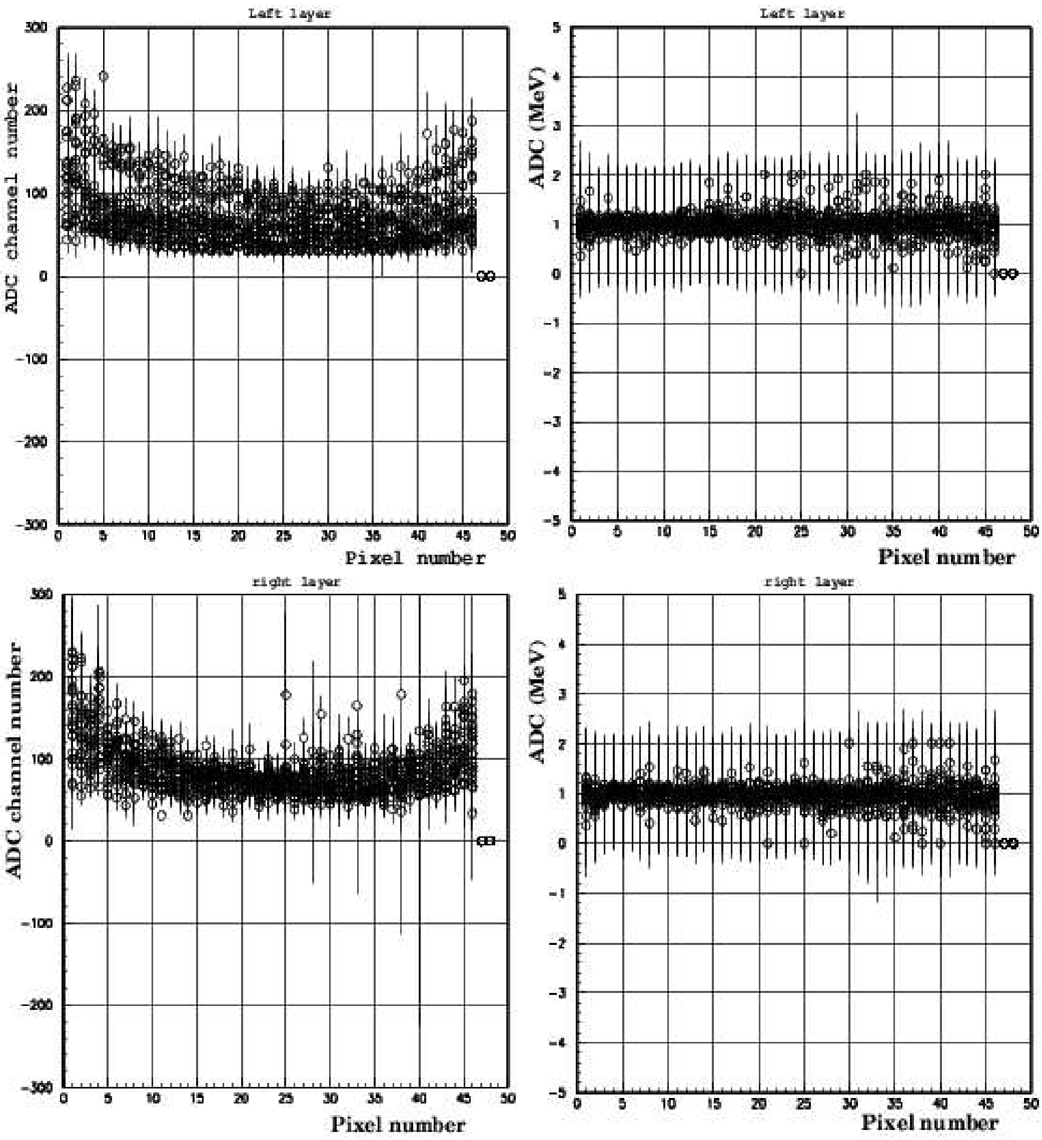

Figure B.2: The ADC spectrum of the wound layers of the Quirl detector before (left) and after (right) calibration. Figure is taken from [55].

Appendix C

Response Pattern and Single Straw Efficiency

For a given experiment and an event A with a probability of $P(A) = p$ and $P(\bar{A}) = q$ where $p + q = 1$, the probability that the event A occurs exactly k times in any order at n trail is given [103]:

$$P_n(k) = \frac{n!}{(n-k)! \cdot k!} \cdot p^k \cdot q^{n-k}$$

If we consider that the straw responds with a probability ϵ on a hit (the efficiency of the single straw), and assume instead of 8 straws (from 4 double planes) 8 trials on a single straw tube, we can write the probability that the straw is responding k times from 8 trials as:

$$P_8(k) = \frac{8!}{(8-k)! \cdot k!} \cdot \epsilon^k \cdot (1-\epsilon)^{8-k}$$

$$\begin{aligned} P_8(8) &= \epsilon^8 \\ P_8(7) &= 8 \cdot \epsilon^7 \cdot (1-\epsilon)^1 \\ P_8(6) &= 28 \cdot \epsilon^6 \cdot (1-\epsilon)^2 \\ &\vdots \end{aligned}$$

Fig.C.1 shows the plots of $P_8(0), \ldots, P_8(8)$.

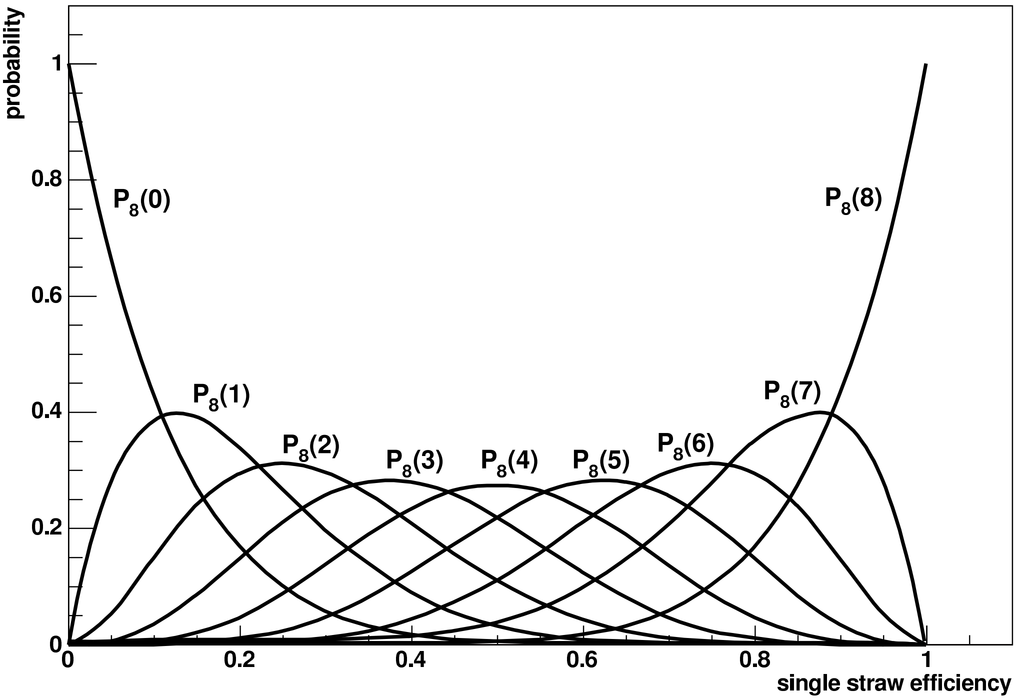

Figure C.1: $P_8(k)$ versus ϵ.

Bibliography

[1] H. Perkins Donald. *Introduction to High Energy Physics.* Addison-Wesley, Oxford, 1982.

[2] M. Gell-Mann. *Phys. Lett.*, 8:214, 1964.

[3] W. N. Cottingham and D. A. Greenwood. *An Introduction to the Standard Model of Particle Physics.* Cambridge University Press, Cambridge, 1998.

[4] Particel Data Group. Review of Particle Physics/Particle Physics Booklet. *C. Caso et al., Phys. J.*, C3, 1998.

[5] D. Flamm and F. Schorebel. *Introduction to the Quark Model of Elementary Particles.* Gordon and Breach Science Publishers, New York, 1982.

[6] G. Dissertori, G. Knowles Ian, and M. Schmelling. *Quantum Chromodynamics.* Clarendon Press, Oxford, 2003.

[7] B. L. Ioffe. QCD at Low Energies. 2005.

[8] M. Judah Eisenberg and S. Koltun Daniel. *Theory of Meson Interactions with Nuclei.* A Wiley-Interscience Publication, New York, 1980.

[9] C. Hanhart. Meson production in nucleon nucleon collisions close to the threshold. *Phys. Rept.*, 397:155–256, 2004.

[10] E. Merzbacher. *Quantum Mechanics.* JOHN WILEY & SONS, New York, 1961.

[11] M. Schmidt. Rutherford Scattering Experiment. http://www.pha.jhu.edu/∼ mschmid7/rutherford.pdf.

[12] H. Machner. *Einfuehrung in die Kern- und Elementarteilchenphysik.* WILEY-VCH, Weinheim, 2005.

[13] R. Mankel. Patern recognition and event reconstruction in particle physics experiments. *Rep. Prog. Phys.*, 67:553–622, 2004.

[14] Private communication Prof. Dr. Kilian K. Research Center Jülich.

[15] R. Bilger et al. Proton proton bremsstrahlung at 797-MeV/c. *Phys. Lett.*, 429:195, 1998.

[16] U. Bechstedt et al. Status of the Cooler Synchrotron COSY Jülich. Presented at IEEE Particle Accelerator Conference (PAC2001), Chicago, Illinois, 18-22 Jun 2001.

[17] H. Stockhorst et al. The Cooler Synchrotron COSY Facility. Prepared for 17th IEEE Particle Accelerator Conference (PAC 97): Accelerator Science, Technology and Applications, Vancouver, British Columbia, Canada, 12-16 May 1997.

[18] R.A Maier. Cooler Synchrotron COSY - performance and perspectives. *Nucl. Inst. Meth.*, A390, 1997.

[19] D. Prasuhn et al. Electron and stochastic cooling at COSY. *Nucl. Instrum. Meth.*, A441:167–174, 2000.

[20] D. Prasuhn et al. Stabilization of an Electron Cooled Proton Beam at Injection with Sextupoles. IKP Annual Report 2002, Jülich/Germany, 2002.

[21] D. Prasuhn et al. Stochastic Cooling System in COSY. Proc. EPAC94, 1994.

[22] R. Toelle et al. The cooler synchrotron cosy in jülich. *NIM B*, 113, no.1-4:26–29, 1996.

[23] H. Stockhorst et al. The Medium Energy Proton Synchrotron COSY. Prepared for 7th European Particle Accelerator Conference (EPAC 2000), Vienna, Austria, 26-30 Jun 2000.

[24] H. Machner. Recent physics at COSY: A review. 2005.

[25] D. Grzonka and K. Kilian. Associated hyperon production at COSY. *Acta Phys. Polon.*, B29:3463–3472, 1998.

[26] H. Machner and J. Haidenbauer. Meson production close to threshold. *PiN Newslett.*, 15:311–314, 1999.

[27] J. M. Laget. Strangeness production in nucleon-nucleon collisions. *Phys. Lett.*, B259:24–28, 1991.

[28] The COSY-TOF Collaboration. Hyperon production in the channel $pp- > K^+p\Lambda$ near the reaction threshold. *Physics Letters*, B632:27, 2006.

[29] O. Schult et al. *Nucl. Phys*, A583:629, 1995.

[30] E. Roderburg et al. Studies of p p and p d interactions with the time-of-flight spectrometer at cosy. *Acta Phys. Polon.*, B27:2953–2957, 1996.

[31] The COSY-TOF Collaboration. Evidence for a narrow resonance at 1530-MeV/c^2 in the K^0p system of the reaction $pp \rightarrow \Sigma^+K^0p$ from the COSY-TOF experiment". *Phys. Lett.*, B595:127–134, 2004.

[32] D. Grzonka and K. Kilian. Overview of the experimental program of strangeness production at COSY. *Nucl. Phys.*, A691:473–482, 2001.

[33] W. Eyrich et al. Strangeness production in proton proton reactions at cosy- tof. *PiN Newslett.*, 13:373–376, 1997.

[34] E. Kuhlmann et al. Light meson production and p p bremsstrahlung at the cosy time-of-flight spectrometer. *Phys. Scripta*, 48:226–228, 1993.

[35] The COSY-TOF Collaboration. Study of the reaction $pp \rightarrow pp\pi^0$ within 10-MeV above the threshold. *Eur. Phys. J.*, A17:595–606, 2003.

[36] The COSY-TOF Collaboration. Measurement of the eta production in proton proton collisions with the COSY time of flight spectrometer. *Eur. Phys. J.*, A16:127–137, 2003.

[37] K. T. Brinkmann et al. Three-particle final states measured at the pion threshold with the cosy-tof spectrometer. *Acta Phys. Polon.*, B29:2993–2997, 1998.

[38] E. Roderburg et al. Studies of eta and eta-prime measurements with the time-of- flight spectrometer at cosy. *Acta Phys. Polon.*, B24:1629–1640, 1994.

[39] K. Brinkmann et al. Vector meson production in collisions of nucleons. *Int. J. Mod. Phys.*, A20:427–435, 2005.

[40] S. Abd El-Samad et al. Production of omega mesons in proton proton collisions. *Phys. Lett.*, B522:16–21, 2001.

[41] R. Bilger et al. Measurement of the $pd \rightarrow^3 He\eta$ cross section between 930 and 1100 MeV. *Phys. Rev.*, C65:044608, 2002.

[42] TOF-Collaboration. Juelich, Germany.
http://www.fz-juelich.de/ikp/COSY-TOF/detektor/DetektorPrinzip_e.html.

[43] The COSY-TOF Collaboration. The COSY-TOF barrel detector. *Nuclear Instruments and Methods in Physics Research Section A: Accelerators, Spectrometers, Detectors and Associated Equipment*, 443:238–253, 2000.

[44] V. Jaeckle et al. A liquid hydrogen / deuterium target with very thin windows. *Nucl. Instrum. Meth.*, A349:15–17, 1994.

[45] K. Kilian et al. A liquid hydrogen/deuterium target with very thin windows. *Nuclear Instruments and Methods in Physics Research Section A: Accelerators, Spectrometers, Detectors and Associated Equipment*, 349:15–17, 1994.

[46] S. Abdel-Samad, M. Abdel-Bary, and K. Kilian. New developments in cryo-targts for the external cosy experiments. *Nuclear Instruments and Methods in Physics Research*, A 495:1–7, 2002.

[47] S. Abdel-Samad et al. Cryogenic target with very thin gold finger heat pipe. *Nuclear Instruments and Methods in Physics Research*, A556:20, 2006.

[48] Mamdouh Mohamed Abd El-Bary Dewidar. *Development of a Cryogenic Target System with Optimal Access to Reaction Detectors.* Ph. D Thesis, der Rheinisch-Westfaellischen Technischen Hochschule Aachen, 2004.

[49] S. Abdel-Samad. *Improving the Properties of Cryogenic Targets for the external Cooler Synchroton (COSY) Experiments.* Ph. D Thesis, der Rheinisch-Westfaellischen Technischen Hochschule Aachen, 2001.

[50] P. Michel et al. Mars: A start detector system for the cosy time-of-flight spectrometer tof. *Nuclear Instruments and Methods in Physics Research*, A408:453, 1998.

[51] W. Eyrich et al. A detector system for hyperon production at the cosy time- of-flight spectrometer. *Phys. Scripta*, 48:115–116, 1993.

[52] D. Hesselbarth. *Experimentelle Untersuchungen zur Hyperon-Produktion im Proton-Protan-Stoss.* Ph. D Thesis, der Rheinischen Friedrich-Wilhelms-Universitaet Bonn, 2001.

[53] M. Dahmen et al. The quirl scintillator. *Nuclear Instruments and Methods in Physics Research*, A348:97, 1994.

[54] A. Böhm et al. The cosy-tof barrel detector. *Nuclear Instruments and Methods in Physics Research*, A443:238, 2000.

[55] Amein Mohamed Abdel-Ghaffar Hassan. *Two Step Processes for Meson Production at the Time Of Flight Spectrometer at COSY.* Ph. D Thesis, Institut fuer Kernphysik Forschungszentrum Jülich, Germany, 1998.

[56] K. Kilian. Straw tracker with very low total mass. FP6/I3NS application July 2002.

[57] K. Nunighoff et al. A light straw tracker detector working in vacuum. *Nucl. Instrum. Meth.*, A477:410–413, 2002.

[58] K. Kilian et al. Development of a Very Light Track Detector for TOF. IKP Annual Report 1997, Jülich/Germany.

[59] http://en.wikipedia.org/wiki/Solid_angle.

[60] P. Wintz et al. The New Straw Tracker For COSY-TOF. IKP Annual Report 2003, Jülich/Germany.

[61] http://en.wikipedia.org/wiki/Young's_modulus.

[62] A. H. Walenta, J. Heintze, and B. Schuerlein. The multiwire drift chamber, a new type of proportional wire chamber. *Nucl. Instrum. Meth.*, 92:373–380, 1971.

[63] F. Sauli. Principles of Operation of Multiwire Proportional and Drift Chambers. Experimental Techniques in Nuclear and Particle Physics, T. Ferbel ed., World Scientific, 1991.

[64] H. Bethe and M. Livingston. *Rev. Mod. Phys.*, 9:285, 1937.

[65] E.N. Lassestre et al. *J. Chem. Phys.*, 49:2382, 1968.

[66] S.F. Biagi. *Nucl. Instr. and Meth.*, A283:716, 1989.

[67] B. Schmidt and K. Martens. *HD-PY*, 92/02:1992, 1992.

[68] R. Bouclier et al. Recent developments of the multi drift tube. *Nucl. Instr. and Meth.*, A283:509, 1989.

[69] F.F. Reike and W. Prepejchal. *Phys. Rev. D*, A6:1507, 1972.

[70] D. Denisov. *Nucl. Instr. and Meth.*, A306:200, 1991.

[71] A. Sharma. Properties of some gas mixtures used in tracking detectors. SLAC-J-ICFA-16-3.

[72] http://rkb.home.cern.ch/rkb/PH14pp/node62.html.

[73] http://www.upscale.utoronto.ca/PVB/DBailey/SubAtomic/Lectures/LectF04/Lect04.htm.

[74] http://besch2.physik.uni-siegen.de/∼depac/DePAC/DePAC_tutorial_database.

[75] D. H. Wilkinson. Ionization energy loss by charged particles. I: The Landau distribution. *Nucl. Instrum. Meth.*, A383:513–515, 1996.

[76] A. Sokolow. *Development of proportional chamber detector and simulations to measure charm hadrons in antiproton-proton annihilation.* Ph. D Thesis, Justus Liebig Uni. Giessen, 2005.

[77] V. Palladino and B. Sadoulet. *Nuclear Instruments and Methods*, 128:323, 1975.

[78] V. Palladino and B. Sadoulet. Application of the classical theory of electrons in gases to multiwire proportional and drift chamber. Lawrence Berkeley Lab. Report LBL-3013, 1974.

[79] T. Holstein. *Phys. Rev.*, 70:367, 1946.

[80] K. B. Ines and B. Grosswendt. *Nuclear Instruments and Methods in Physics Research Section B: Beam Interactions with Materials and Atoms*, 142:219–244, 1998.

[81] T. Aoyama. *Nuclear Instruments and Methods in Physics Research Section A: Accelerators, Spectrometers, Detectors and Associated Equipment*, 234:125–131, 1985.

[82] A. H. Walenta et al. Laboratory Course on Silicon Sensors.

[83] Private communication Mr. Mohos I. Research Center Jülich.

[84] H. Albrecht et al. The Outer Tracker detector of the HERA-B experiment. Part II: Front-end electronics. *Nucl. Instrum. Meth.*, A541:610–629, 2005.

[85] K. Berkhan et al. Large-System Experience with the ASD-8 Chip in the HERA-B Experiment.
http://ph-collectif-lecc-workshops.web.cern.ch/ph-collectif-lecc-workshops/LEB99_Book/Posters/kolanoski.pdf.

[86] Private communication Mr. Nellen R. Research Center Jülich.

[87] S. Hendel. Untersuchungen zu Entwicklung eines neuartigen Detector zur spurrekonstruktion von Elementarteilchen. Diplomarbeit, Technische Fachhochshule Wildau, 2003. IKP-Jül-2825.

[88] M.R. Convery. A Device for Quick and Reliable Measurement of Wire Tension. Princeton/BABAR TNDC-96-39, 1993.

[89] P. Wintz. Large tracking detector in vacuum consisting of self-supporting straw tubes. HPC2003, BHonnef/July-2003, Germany.

[90] N. Dennis and T. Heppell. *Vacuum system Design.* Chapman and Hall LTD, UK, 1968.

[91] C. F. G. Delaney and E. C. Finch. *Radiation Detectors.* Clarendon Press, Oxford, 1992.

[92] M. Danilov et al. Aging tests of the proportional wire chambers. 2002.

[93] P. Wintz et al. Resolution and Efficiency of the Straw Tracker for COSY-TOF. IKP Annual Report 2004, Jülich/Germany.

[94] R. Veenhof. GARFIELD, Computer program for the detailed simulation of two- and three-dimensional drift chambers. CERN Program Library, CERN, Geneva, Switzerland.

[95] M. S. Wissermann. *Investigation of Meson Production at COSY-TOF Using the Analysis Framework TofRoot.* Ph. D Thesis, Technische Universitaet Dresden, 2004.

[96] M. Dahmen. *Das Flugzeitspektrometer an COSY: Ein Detektor zur excklusiven Messung von Mehrteilchenreaktionen.* Ph. D Thesis, der Rheinischen Friedrich-Wilhelms-Universitaet Bonn, 1995.

[97] GEANT-Detector Description and Simulation Tool, CERN Program Library Long Writeup W5013. CERN, 1211 Geneva 23, Switzerland, 1993.

[98] R. A. Mewaldt. California Institute of Technology
http://www.srl.caltech.edu/personnel/dick/cos_encyc.html.

[99] K. Zwoll. *Nuclear Science, IEEE Transactions on*, 43:44, 1996.

[100] K. Zwoll et al. *Nuclear Science, IEEE Transactions on*, 41:37, 1994.

[101] ROOT, Users Guide 3.02c. CERN, 1211 Geneva 23, Switzerland, 2002.

[102] http://rd11.web.cern.ch/RD11/rkb/PH14pp/node26.html.

[103] Athanasios Papoulis. *Probability, Random Variables, and Stochastic Processes.* McGRAW-Hill, New York, 1991.